MARS ATMOSPHERE

Mars methane detection and variability at Gale crater

Christopher R. Webster,[1]* Paul R. Mahaffy,[2] Sushil K. Atreya,[3] Gregory J. Flesch,[1] Michael A. Mischna,[1] Pierre-Yves Meslin,[4] Kenneth A. Farley,[5] Pamela G. Conrad,[2] Lance E. Christensen,[1] Alexander A. Pavlov,[2] Javier Martín-Torres,[6,7] María-Paz Zorzano,[8] Timothy H. McConnochie,[9] Tobias Owen,[10] Jennifer L. Eigenbrode,[2] Daniel P. Glavin,[2] Andrew Steele,[11] Charles A. Malespin,[2] P. Douglas Archer Jr.,[12] Brad Sutter,[12] Patrice Coll,[13] Caroline Freissinet,[2] Christopher P. McKay,[14] John E. Moores,[15] Susanne P. Schwenzer,[16] John C. Bridges,[17] Rafael Navarro-Gonzalez,[18] Ralf Gellert,[19] Mark T. Lemmon,[20] the MSL Science Team†

Reports of plumes or patches of methane in the martian atmosphere that vary over monthly time scales have defied explanation to date. From in situ measurements made over a 20-month period by the tunable laser spectrometer of the Sample Analysis at Mars instrument suite on Curiosity at Gale crater, we report detection of background levels of atmospheric methane of mean value 0.69 ± 0.25 parts per billion by volume (ppbv) at the 95% confidence interval (CI). This abundance is lower than model estimates of ultraviolet degradation of accreted interplanetary dust particles or carbonaceous chondrite material. Additionally, in four sequential measurements spanning a 60-sol period (where 1 sol is a martian day), we observed elevated levels of methane of 7.2 ± 2.1 ppbv (95% CI), implying that Mars is episodically producing methane from an additional unknown source.

Because Earth's atmospheric methane is predominantly biologically produced (*1*), determining the abundance and variability of methane in the current martian atmosphere is critical to assessing the contribution from a variety of potential sources or reservoirs that may be biological [such as methanogens (*1*, *2*)] or abiotic (*1*). These latter processes include geological production such as serpentinization of olivine (*3*), ultraviolet (UV) degradation of meteoritically delivered organics (*4*–*6*), production by impacts of comets (*7*), release from subsurface clathrates (*8*) or regolith-adsorbed gas (*9*, *10*), erosion of basalt with methane inclusions (*11*), or geothermal production (*12*). Several detections of Mars methane have been published. Ground-based observations from the Canada-France-Hawaii Telescope in 1999 found a global average value of 10 ± 3 parts per billion by volume (ppbv) (*2*), and those using the NASA Infrared Telescope Facility (IRTF) telescope in 2003 reported (*13*) methane release in plumes from discrete sources in Terra Sabae, Nili Fossae, and Syrtis Major that showed seasonal changes with a summertime maximum of ~45 ppbv near the equator. The planetary Fourier spectrometer (PFS) on the Mars Express (MEX) spacecraft reported detection in 2004 (*14*) with an updated global average abundance of 15 ± 5 ppbv (*15*), with indications of discrete localized sources and a summertime maximum of 45 ppbv in the north polar region. From the thermal emission spectrometer (TES) of Mars Global Surveyor, methane abundances from 5 to 60 ppbv were deduced (*16*) as intermittently present over locations where favorable geological conditions such as residual geothermal activity (Tharsis and Elysium) and strong hydration (Arabia Terrae) might be expected. Using data from NASA IRTF acquired in February 2006, Krasnopolsky (*17*) reported a detection of 10 ppbv at mid-latitudes (42° to 7°N) over Valles Marineris but an upper limit of 3 ppbv outside that region. In December 2009, Krasnopolsky obtained an upper limit of 8 ppbv and noted that data from both observations agreed with those of Mumma *et al.* (*13*). More recent ground-based observations report methane mixing ratios that have diminished considerably since 2004–2006 to a 2σ upper limit of 5 ppbv (*17*–*19*), suggesting a very short lifetime for atmospheric CH_4 and contradicting the MEX claim that methane persisted from 2004–2010. At Curiosity's Gale crater landing site (4.5°S, 137°E), published maps of PFS data (*15*) show an increase from ~15 ppbv in fall to ~30 ppbv in winter, whereas the TES trend (*16*) is opposite: ~30 ppbv in fall and ~5 ppbv in winter.

Observational evidence for methane on Mars has been questioned in the published literature (*20*–*22*) because photochemical models are unable to reconcile the observed amounts with their reported spatial gradients and temporal changes over months compared with the expected ~300-year methane lifetime. Contradictions were noted between the locations of maxima reported from ground-based observations and maps inferred by PFS and TES from Mars orbit. The plume results (*13*) were questioned (*22*) on the basis of a possible misinterpretation from methane lines whose positions coincided with those of terrestrial isotopic $^{13}CH_4$ lines. Krasnopolsky (*7*) argued that cometary and volcanic contributions were not sufficient to explain high methane abundances—noting for the latter possibility the lack of current volcanism or hot spots in thermal imaging (*23*)—and the extremely low upper limit for Mars SO_2 that in Earth's volcanic emissions is orders of magnitude more abundant than CH_4, as predicted for Mars (*24*). Model calculations including expected atmospheric transport and circulation (*20*, *25*) are, to date, all unable to reproduce the spatial and temporal characteristics of the observed high-concentration methane plumes, whether resulting from possible clathrate release (*8*) or surface adsorption by or desorption from the regolith (*9*) or for UV degradation of surface organics (*4*–*6*), despite the introduction of a variety of putative loss mechanisms (*26*–*28*).

The tunable laser spectrometer (TLS) of the Sample Analysis at Mars (SAM) (*29*) instrument suite on the Curiosity rover has a spectral resolution (0.0002 cm^{-1}) that offers unambiguous identification of methane in a distinct fingerprint spectral pattern of three well-resolved adjacent $^{12}CH_4$ lines in the 3.3-μm band (*30*). The in situ technique of tunable laser absorption in a closed sample cell is simple, noninvasive, and sensitive. TLS is a two-channel tunable laser spectrometer that uses both direct and second harmonic detection of infrared (IR) laser light. One channel uses a near-IR tunable diode laser at 2.78 μm that has yielded robust data on carbon, oxygen, and hydrogen isotopic ratios on Mars (*31*). The second channel uses an interband cascade tunable laser at 3.27 μm for methane detection alone, scanning across seven rotational lines that include the R(3) triplet used in this study. This laser makes 81 passes of a 20-cm-long sample cell of the Herriott design fitted with high-vacuum microvalves that allow evacuation with a turbomolecular pump for empty cell scans or filled to Mars ambient pressure (~7 mbar) for full cell runs. Our methane determination is made by differencing the measured methane abundances in our sample cell when filled with Mars atmosphere from measurements

[1]Jet Propulsion Laboratory, California Institute of Technology, Pasadena, CA 91109, USA. [2]NASA Goddard Space Flight Center, Greenbelt, MD 20771, USA. [3]University of Michigan, Ann Arbor, MI 48109, USA. [4]Institut de Recherche en Astrophysique et Planétologie, UPS-OMP, CNRS, 31028 Toulouse, France. [5]California Institute of Technology, Pasadena, CA 91125, USA. [6]Instituto Andaluz de Ciencias de la Tierra [Consejo Superior de Investigaciones Científicas (CSIC)–Universidad de Granada], Granada, Spain. [7]Division of Space Technology, Luleå University of Technology, Kiruna, Sweden. [8]Centro de Astrobiologia, Instituto Nacional de Técnica Aeroespacial–CSIC, Madrid, Spain. [9]Department of Astronomy, University of Maryland, College Park, MD 20742, USA. [10]University of Hawaii, Honolulu, HI 96822, USA. [11]Carnegie Institution of Washington, Washington, DC 20015, USA. [12]Jacobs Technology, NASA Johnson Space Center, Houston, TX 77058, USA. [13]Laboratoire Inter-Universitaires Des Systèmes Atmosphériques (LISA), UMR CNRS 7583, Paris, France. [14]NASA Ames Research Center, Mountain View, CA 94035, USA. [15]York University, Toronto, Ontario M3J 1P3, Canada. [16]The Open University, Milton Keynes MK7 6AA, UK. [17]Space Research Centre, University of Leicester, Leicester LE1 7RH, UK. [18]Instituto de Ciencias Nucleares, Universidad Nacional Autonoma de Mexico, Mexico City 04510, Mexico. [19]University of Guelph, Guelph, Ontario N1G 2W1, Canada. [20]Texas A&M University, College Station, TX 77843, USA.
*Corresponding author. E-mail: chris.r.webster@jpl.nasa.gov
†The MSL Science Team authors and affiliations are listed in the supplementary materials.

of the same cell evacuated, as detailed in the supplementary materials (*32*).

From our first six observations spanning a 234-sol period (1 sol = 1 Mars day = 24 hours 37.3 min), we previously reported (*33*) a mean value of 0.18 ± 0.67 ppbv that was not precise enough to claim detection of Mars methane but instead set an upper limit of 1.3 ppbv [95% confidence interval (CI)] that was significantly lower than those reported (5 ppbv, 95% CI) from recent ground-based observations (*17*–*19*).

We have now reprocessed our entire data set [with a small modification explained in (*32*)]. Our data set now extends the measurement period over 605 sols, including 11 direct-ingest measurements and two recent measurements using a methane enrichment experiment run on sols 573 and 684. In this latter procedure, the atmospheric methane is effectively enriched 23 ± 1 times by flowing the ingested gas slowly over a carbon dioxide scrubber material. Before running on Mars, the instrument script was optimized using the test-bed SAM suite (*32*). Results from the complete data set are given in Table 1 and plotted in Fig. 1. We partition our data points of Fig. 1 into three groups for independent analysis: (i) the low-methane direct-ingest results of sols 79, 81, 106, 292, 313, and 684; (ii) the low-methane enrichment results for sols of 573 and 684; and (iii) the four sequential high-methane runs of sols 466, 474, 504, and 526, as there is no statistically significant variation within each grouping. Mean values for these grouped data sets (final three rows, Table 1) form the basis for our analysis and conclusions. We note the good agreement between the direct and enriched experiments that were run back-to-back on sol 684. The daytime run of sol 306 is not included in group (iii) because it was not part of the high methane sequence, nor is it included in the low-methane group (i) because it is clearly higher than the background average.

Our low-methane enrichment experiments produce a mean value for atmospheric methane of 0.69 ± 0.25 ppbv (95% CI), as described in (*32*). The direct-ingest (nonenrichment) group yields a mean methane value of 0.89 ± 1.96 ppbv (95% CI), agreeing with the higher-precision enrichment value within error. For the high-methane abundance seen in direct-ingest group, we measure a mean value of 7.19 ± 2.06 ppbv (95% CI) for the four sols 466, 474, 504, and 526. In the supplementary materials (*32*), we provide arguments to rule out the possibility of terrestrial contamination and therefore conclude that the enrichment result and the high-methane result independently produce detection of methane at two levels of abundance. Although TLS samples only the very lowest part (~1 m) of the Mars atmosphere in the Gale crater region, the atmospheric mixing time of a few months suggests that our measured value of 0.69 ± 0.25 ppbv (95% CI) is probably representative of the mean background level for Mars atmospheric methane abundance, which is only expected to vary substantially and seasonally over the winter poles (*20*).

Table 1. Curiosity TLS-SAM methane measurements at Gale crater (4.5°S, 137.4°E) over a 20-month period. L_s, solar longitude. CI values are ±2 SEM for individual results and are explained in the supplementary materials (*32*) for the grouped results in the last three rows.

Martian sol after landing 6 Aug 2012	Earth date	L_s (degrees)	Gas ingest time/cell pressure (mbar)/foreoptics pressure (mbar)	Mean value ± 1 SEM (ppbv)	Mean value ± 95% CI (ppbv)
79	25 Oct 2012	195.0	Night/8.0/11.5	−0.51 ± 2.83	−0.51 ± 5.66
81	27 Oct 2012	196.2	Night/8.0/11.5	1.43 ± 2.47	1.43 ± 4.94
106	27 Nov 2012	214.9	Night/8.5/10.9	0.68 ± 2.15	0.68 ± 4.30
292	1 Jun 2013	328.6	Night/8.7/9.2	0.56 ± 2.13	0.56 ± 4.26
306	16 Jun 2013	336.5	Day/8.1/0.0	5.78 ± 2.27	5.78 ± 4.54
313	23 Jun 2013	340.5	Night/8.7/0.0	2.13 ± 2.02	2.13 ± 4.04
466	29 Nov 2013	55.7	Night/8.0/2.3	5.48 ± 2.19	5.48 ± 4.38
474	6 Dec 2013	60.6	Night/7.9/2.3	6.88 ± 2.11	6.88 ± 4.22
504	6 Jan 2014	72.7	Night/8.1/2.3	6.91 ± 1.84	6.91 ± 3.68
526	28 Jan 2014	81.7	Day/7.5/2.3	9.34 ± 2.16	9.34 ± 4.32
573	17 Mar 2014	103.4	Night/5.3/2.3	0.47 ± 0.11	0.47 ± 0.22
684	9 Jul 2014	158.8	Night/4.5/2.7	0.90 ± 0.16	0.90 ± 0.32
684	9 Jul 2014	158.8	Night/6.8/2.7	0.99 ± 2.08	0.99 ± 4.16
Mean value of low-methane sols 79, 81, 106, 292, 313, 684				0.89 ± 0.70	0.89 ± 1.96
Mean value of low-methane enrichment results for sols 573 and 684				0.69 ± 0.09	0.69 ± 0.25
Mean value of high-methane sols 466, 474, 504, 526				7.19 ± 0.74	7.19 ± 2.06

The principal sources of organics delivered exogenously to Mars are isotropically accreted interplanetary dust particles (IDPs) and low-mass carbonaceous chondrites containing up to 10% organics by weight (*1*, *4*–*6*). Recent observations by SAM on Curiosity have detected the presence of chlorobenzene and simple chlorinated alkanes (*34*) in a drilled martian mudstone in Gale crater. Laboratory studies of meteoritic materials have shown that UV irradiation of organic molecules can produce methane either directly (*5*) or through secondary photochemical reaction (*35*) and that certain molecules can form a photoresistant layer leading to methane over extended time periods (*6*). Constrained by laboratory production rates, models have assessed the rate and size of infall of meteoritic material such as IDPs, carbonaceous chondrites, and other sources of organic carbon to the martian surface that might reproduce methane observations under Mars-like UV conditions. The UV/CH_4 model of isotropically accreted IDP organics of Schuerger *et al.* (*5*) predicts that the UV-induced production of methane is carbon-limited and over geological time can produce a globally averaged methane abundance of 2.2 ppbv methane for a 20% conversion rate of organic carbon to methane. No significant diurnal or seasonal changes are predicted by this model, which cannot explain the variability of methane over relatively short time scales observed in earlier studies (*13*, *15*). Even with consideration of single large bolide impacts or multiple airburst events, the models struggle to emplace sufficient carbon over the large surface areas of the plume observations and, more importantly, cannot supply methane fast enough to create plumes over the observed time frame (*5*).

Our background methane abundance reported here of ~0.7 ppbv from the low-methane enrichment is significantly lower than the 2.2 ppbv obtained from the Schuerger UV/CH_4 model estimate (*5*) described above, despite the fact that measured surface UV levels from Curiosity's Rover Environmental Monitoring Station (REMS) instrument (*32*, *36*) agree with the model values (*5*). This implies that either the quantity of delivered carbon or its conversion efficiency to methane is one-third of the model's estimates or that an indigenous source may be having an effect. It is also likely that the fresh analog material used by Schuerger *et al.* (*5*) is not completely representative of the bulk of material (UV-processed IDPs) being delivered to Mars.

As detailed in (*32*), our high-methane result of 7.19 ± 2.06 ppbv (95% CI) shows no significant quantitative correlation with relative humidity, atmospheric pressure (carbon dioxide abundance), ground or air temperature, inlet pointing, or radiation levels measured by other Curiosity instruments: the REMS (*36*), the Chemistry and Camera complex [ChemCam (*37*)], and the Radiation Assessment Detector (*38*). The REMS observations suggest a plausible anticorrelation with water abundance as well as air and ground temperatures, and both REMS and the Curiosity mast camera (*39*) show a possible anticorrelation with atmospheric opacity (*32*), but our first enrichment measurement on sol 573 spoils this. However, all methane measurements (including sol 573) support an anticorrelation of methane abundance with column measurements of oxygen abundance and water vapor as measured by the ChemCam instrument (see fig. S9), the latter contrasting with the weak positive correlation observed by the Mars Express PFS (*8*, *40*).

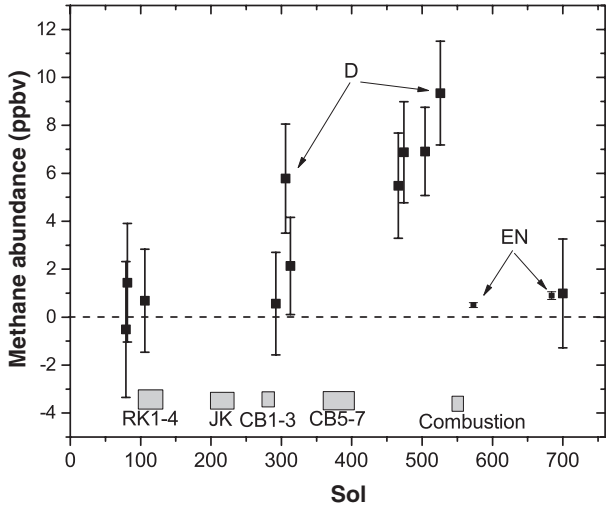

Fig. 1. The TLS-SAM methane measurements versus martian sol. Plotted values are from Table 1, with error bars representing ±1 SEM. Those with larger error bars are the direct-ingest results, and the two with smaller error bars labeled "EN" are the values retrieved from the methane enrichment runs. All measurements were made from nighttime ingest, except the two marked "D" that were ingested during the day and analyzed at night. The last direct-ingest value (plotted near sol 700) occurred during the same sol 684 as the last enrichment run but is offset to a higher sol value to separate the points for visual clarity. The shaded boxes show the occurrence and duration of the SAM evolved gas analysis runs for Rocknest (RK), John Klein (JK), Cumberland (CB), and combustion during which gases evolved from rock samples were introduced into SAM and a portion was fed into the TLS sample cell for analysis.

However, the lack of O_2 and H_2O data for the solar longitude range L_s = 160 to 220 spoils this comparison, and we must await future measurements to assess this fully.

Concerning the possibility of spatially variable methane abundance, although the high-methane measurements were observed within 200 to 300 m of each other (fig. S10), the rover had not traveled far (~1 km) since the lower value of sol 466, and the high methane disappeared after traveling only a further ~1 km away. Typical ground winds of ~7 m/s (*25*) would cover that distance in only 2 min, and given the rotation of diurnal wind, it is impossible to isolate one location from another. This suggests a short-duration event that is either local and weak or more distant and stronger. The persistence of the high-methane values over 60 sols and their sudden drop 47 sols later is not consistent with a well-mixed event but rather with a local production or venting that, once terminated, disperses quickly. Most of our data are taken at night, when prevailing winds are likely from the south. The marginally higher daytime values suggested in sols 306 and 526 indicate a source to the rover's north, because prevailing daytime winds would advect toward the rover location. The change in rover location is therefore unimportant as this is a temporal, not locational, variation. With a concern that Curiosity transit over varying surface materials [identified by the alpha particle x-ray spectrometer (*41*) measurements] could be associated with the high-methane observations, we studied rover stand time and local terrain composition (*32*) and ruled out such potential contributions. Although we cannot rule out possible clathrate release (*8*) or surface adsorption into the regolith with subsequent release (*9*), both these mechanisms do not support the local, short–time scale variation that we observe.

Our measurements of a background methane abundance of ~0.7 ppbv can be reconciled with photochemical models that include an exogenous source such as UV degradation of organics (*5*) because model results likely represent upper limits with extensive UV processing in space before delivery to Mars. Like the earlier plume measurements, our higher transient methane amounts of ~7 ppbv require an additional source of methane, in our case suggesting advection to the rover location from a local unidentified source. If that source were a recent bolide striking Gale crater and producing 1% methane, we estimate that it would have to be several meters in size and leave a crater of tens of meters in diameter, but no new impact craters have been observed within Gale crater from Mars orbit time-series imaging (*42*) since landing. Our measurements spanning a full Mars year indicate that trace quantities of methane are being generated on Mars by more than one mechanism or a combination of proposed mechanisms—including methanogenesis either today or released from past reservoirs, or both.

REFERENCES AND NOTES

1. S. K. Atreya, P. R. Mahaffy, A. S. Wong, *Planet. Space Sci.* **55**, 358–369 (2007).
2. V. A. Krasnopolsky, J. P. Maillard, T. C. Owen, *Icarus* **172**, 537–547 (2004).
3. C. Oze, M. Sharma, *Geophys. Res. Lett.* **32**, L10203 (2005).
4. F. Keppler *et al*., *Nature* **486**, 93–96 (2012).
5. A. Schuerger, J. E. Moores, C. A. Clausen, N. G. Barlow, D. T. Britt, *J. Geophys. Res.* **117**, E08007 (2012).
6. O. Poch, S. Kaci, F. Stalport, C. Szopa, P. Coll, *Icarus* **242**, 50–63 (2014).
7. V. A. Krasnopolsky, *Icarus* **180**, 359–367 (2006).
8. E. Chassefière, *Icarus* **204**, 137–144 (2009).
9. P.-Y. Meslin, R. Gough, L. Lefevre, F. Forget, *Planet. Space Sci.* **59**, 247–258 (2011).
10. R. V. Gough, M. A. Tolbert, C. P. McKay, O. B. Toon, *Icarus* **207**, 165–174 (2010).
11. S. McMahon, J. Parnell, N. J. F. Blamey, *Int. J. Astrobiol.* **12**, 113–122 (2013).
12. G. Etiope, D. Z. Oehler, C. C. Allen, *Planet. Space Sci.* **59**, 182–195 (2011).
13. M. J. Mumma *et al*., *Science* **323**, 1041–1045 (2009).
14. V. Formisano, S. Atreya, T. Encrenaz, N. Ignatiev, M. Giuranna, *Science* **306**, 1758–1761 (2004).
15. A. Geminale, V. Formisano, G. Sindoni, *Planet. Space Sci.* **59**, 137–148 (2011).
16. S. Fonti, G. A. Marzo, *Astron. Astrophys.* **512**, A51 (2010).
17. V. A. Krasnopolsky, *EPSC Abstracts* **6**, 49 (2011).
18. V. A. Krasnopolsky, *Icarus* **217**, 144–152 (2012).
19. G. L. Villanueva *et al*., *Icarus* **223**, 11–27 (2013).
20. F. Lefèvre, F. Forget, *Nature* **460**, 720–723 (2009).
21. S. K. Atreya *et al*., *Planet. Space Sci.* **59**, 133–136 (2011).
22. K. J. Zahnle, R. S. Freedman, D. C. Catling, *Icarus* **212**, 493–503 (2011).
23. P. R. Christensen, *Eos Trans. AGU Fall Meet. Suppl.* **84** (46), Abstract P21A-02 (2003).
24. F. Gaillard, J. Michalski, G. Berger, S. M. McLennan, B. Scaillet, *Space Sci. Rev.* **174**, 251–300 (2013).
25. M. A. Mischna, M. Allen, M. I. Richardson, C. E. Newman, A. D. Toigo, *Planet. Space Sci.* **59**, 227–237 (2011).
26. S. K. Atreya *et al*., *Astrobiology* **6**, 439–450 (2006).
27. G. T. Delory *et al*., *Astrobiology* **6**, 451–462 (2006).
28. W. M. Farrell, G. T. Delory, S. K. Atreya, *J. Geophys. Res.* **33**, L21203 (2006).
29. P. R. Mahaffy *et al*., *Space Sci. Rev.* **170**, 401–478 (2012).
30. C. R. Webster, P. R. Mahaffy, *Planet. Space Sci.* **59**, 271–283 (2011).
31. C. R. Webster *et al*., *Science* **341**, 260–263 (2013).
32. See supplementary materials on *Science* Online.
33. C. R. Webster, P. R. Mahaffy, S. K. Atreya, G. J. Flesch, K. A. Farley, *Science* **342**, 355–357 (2013).
34. C. Freissinet *et al*., "Organic molecules in the Sheepbed mudstone of Gale crater, Mars," *8th International Conference on Mars*, Abstract 1349, Pasadena, CA, 14 to 18 July 2014; www.hou.usra.edu/meetings/8thmars2014/pdf/1349.pdf.
35. J. R. C. Garry, I. L. ten Kate, Z. Martins, P. Nørnberg, P. Ehrenfreund, *Meteorit. Planet. Sci.* **41**, 391–405 (2006).
36. J. Gómez-Elvira *et al*., *J. Geophys. Res.* **119**, 1680–1688 (2014).
37. T. H. McConnochie *et al*., "ChemCam passive spectroscopy of atmospheric O_2 and H_2O," *8th International Conference on Mars*, Abstract 1328, Pasadena, CA, 14 to 18 July 2014; www.hou.usra.edu/meetings/8thmars2014/pdf/1328.pdf.
38. D. M. Hassler *et al*., *Space Sci. Rev.* **170**, 503–558 (2012).
39. M. T. Lemmon, "The Mars Science Laboratory optical depth record," *8th International Conference on Mars*, Abstract 1338, Pasadena, CA, 14 to 18 July 2014; www.hou.usra.edu/meetings/8thmars2014/pdf/1338.pdf.
40. A. Geminal *et al*., *Planet. Space Sci.* **56**, 1194–1203 (2008).
41. M. E. Schmidt *et al*., "Geochemical classification of rocks in Gale crater with APXS to sol 360: Sediment provenance, mixing, and diagenetic processes," *45th Lunar and Planetary Science Conference*, Abstract 1504, The Woodlands, TX, 17 to 21 March 2014; www.hou.usra.edu/meetings/lpsc2014/pdf/1504.pdf.
42. H. K. Newsom *et al*., "Gale crater and impact processes from Curiosity," *45th Lunar and Planetary Science Conference*, Abstract 2103, The Woodlands, TX, 17 to 21 March 2014; www.hou.usra.edu/meetings/lpsc2014/pdf/2103.pdf.

ACKNOWLEDGMENTS

The research described here was carried out in part at the Jet Propulsion Laboratory, California Institute of Technology, under a contract with NASA. Data described in the paper are further described in the supplementary materials and have been submitted to NASA's Planetary Data System (PDS) under an arrangement with the Mars Science Laboratory (MSL) project. Funding is acknowledged for J.M.-T. and M.-P.Z. from the Spanish Ministry of Economy and Competiveness, J.C.B. from the UK Space Agency, and R.G. from the Canadian Space Agency.

SUPPLEMENTARY MATERIALS

www.sciencemag.org/content/347/6220/415/suppl/DC1
Materials and Methods
Supplementary Text
Figs. S1 to S13
Tables S1 and S2
References (*43*–*45*)
The MSL Science Team Author List

24 September 2014; accepted 5 December 2014
Published online 16 December 2014;
10.1126/science.1261713

Mars methane detection and variability at Gale crater

Christopher R. Webster *et al.*

Science **347**, 415 (2015);
DOI: 10.1126/science.1261713

Science (print ISSN 0036-8075; online ISSN 1095-9203) is published weekly, except the last week in December, by the American Association for the Advancement of Science, 1200 New York Avenue NW, Washington, DC 20005.

Supplementary Materials for

Mars methane detection and variability at Gale crater

Christopher R. Webster,* Paul R. Mahaffy, Sushil K. Atreya, Gregory J. Flesch, Michael A. Mischna, Pierre-Yves Meslin, Kenneth A. Farley, Pamela G. Conrad, Lance E. Christensen, Alexander A. Pavlov, Javier Martín-Torres, María-Paz Zorzano, Timothy H. McConnochie, Tobias Owen, Jennifer L. Eigenbrode, Daniel P. Glavin, Andrew Steele, Charles A. Malespin, P. Douglas Archer Jr., Brad Sutter, Patrice Coll, Caroline Freissinet, Christopher P. McKay, John E. Moores, Susanne P. Schwenzer, John C. Bridges, Rafael Navarro-Gonzalez, Ralf Gellert, Mark T. Lemmon, the MSL Science Team

*Corresponding author. E-mail: chris.r.webster@jpl.nasa.gov

Published 16 December 2014 on *Science* Express
DOI: 10.1126/science.1261713

This PDF file includes:

Materials and Methods

This supplementary material repeats some of that published earlier *(33)* that is here updated and extended to include discussion of the enrichment experiments, spectral difference plots, correlation results of the TLS methane measurements with a variety of observed quantities like relative humidity, water abundance, ground and surface air temperatures, etc., and finally to present arguments for ruling out terrestrial contamination.

The Tunable Laser Spectrometer (TLS) in the Sample Analysis at Mars (SAM) instrument suite on the Curiosity Rover:

This instrument has been previously described in detail *(29,33 and references therein)*. Fig. S1 below shows the optical layout for the methane measurement.

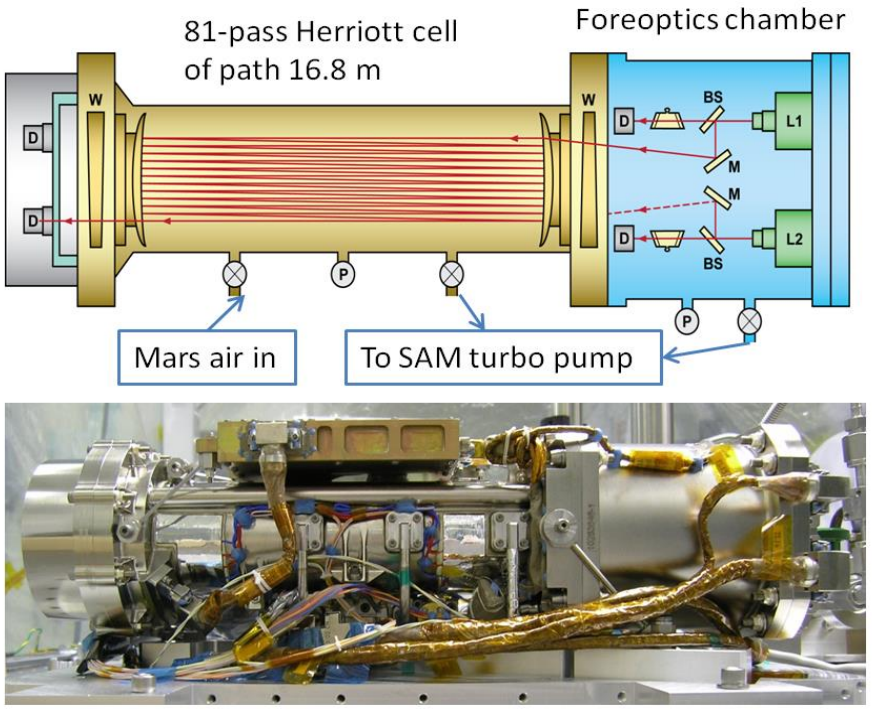

Fig. S1. Top: Schematic of the TLS optical path. Prior to entering the 81-pass (16.8 m pathlength) sample cell through a wedged Ge window (W), the IC laser beam makes a single pass through ~9 cm of a foreoptics chamber containing lasers (L), beam-splitters (BS), reference gas cells (not used for methane measurement), and steering mirrors (M). Bottom: Photo of TLS flight spectrometer before integration into SAM with gold preamplifier on top of Herriott cell.

Methane spectroscopy and laser parameters:

The TLS interband cascade (IC) laser scans through a unique fingerprint of seven spectral lines in the υ_3 band: three $^{12}CH_4$ lines associated with R(3) and four subsequent $^{13}CH_4$ lines associated with R(3) transitions. Table S1 below lists the three $^{12}CH_4$ lines

used for this study, as identified by both the HITRAN data base *(43)* and laboratory measurements. We create the labels e, f, g for these three lines, where the g line is strongest, and both e and f are about half the intensity of the g line.

Table S1. Spectral lines used to identify methane from HITRAN data base *(43)*

Spectral line center (cm^{-1})	Line-strength at 296 K (cm^{-1}/ molecule·cm^{-2})	Ground-state energy (cm^{-1})	Assignment	Label
3057.687285	2.085E-19	62.8781	R(3)	g
3057.726529	1.245E-19	62.8768	R(3)	f
3057.760524	1.245E-19	62.8757	R(3)	e

The IC laser was developed at JPL, and operated near 245 K stabilized by a two-stage thermoelectric cooler (TEC) producing single-mode (>99%) continuous-wave output power with a linewidth retrieved from low-pressure (Doppler limited) spectra of ~10 MHz. This light was collimated using an efficient triple-lens collimator to produce ~1 mW laser power that passes through the foreoptics chamber then into the sample (Herriott) cell. Prior to entering the Herriott cell, the beam was attenuated by a factor of ~20 by a thin mylar sheet (not shown in Fig. S1) to reduce optical fringing and detector non-linearity. We note that the pre-launch settings for the TEC and laser current scans (used for calibration also) have not been changed and the target spectral line positions remain in our scan window. Very small (~linewidth) variations in the spectral line position are seen depending on the Curiosity heat ramp behavior, but we observe and track the methane lines continually for each spectrum through the simultaneously-recorded reference cell detector; the tracked methane spectrum arises from residual methane gas in the foreoptics chamber.

Description of the Difference Method:

We determine Mars methane abundances by differencing full cell and empty cell results (not spectra), as described below. In a typical run on one sol, we collect (downlink) 13 empty cell spectra (2 minutes on board averaged each) followed by 26 full cell, then followed by another 13 empty cell spectra for return-to-zero check. Cell temperatures and pressures are extremely stable during the complete sol run and contribute negligibly to our results (see later). We chose to record relatively long periods of continuous empty or full spectra to make sure that no drift (growth or loss) in retrieved methane abundance was observed during the run. We record sequential 2-minute empty cell spectra for ~1 hour followed by ~1 hour of sequential full cell spectra. We do not difference full-empty spectra before processing. Rather, with powerful computing resources now available, we process each of our 3 methane lines separately in each and all of our 2-minute spectra (by comparison with HITRAN calculations described below), then produce a combined efg-line average abundance for each spectrum that becomes a single raw 2-minute data point. Then, after applying common calibration factors and error contributions, we compare statistically the empty and full cell results for each measurement after normalizing to the empty cell mean values.

Direct and Second-harmonic (2f) Spectra

TLS is designed to simultaneously produce both direct absorption and second harmonic (2f) spectra, as is standard for commercial and laboratory tunable laser spectrometers *(44)*. Tunable laser spectrometers "scan" through spectral lines by applying a current ramp (usually saw-tooth) to the laser that through junction heating changes the wavelength by a small amount, the ramp repeated typically every one second (as done in TLS).

In direct absorption, absorption line depths that indicate gas abundance are measured as dips in the large light level on the detector as the laser is scanned. For very weak absorptions of ~1% or less (due to low gas amounts, too small path lengths or gas pressures, etc., and as expected for low methane (<20 ppbv) amounts) it is challenging for electronics and dynamic range to measure small changes in a large signal, and a "harmonic" detection is preferred. In harmonic detection, the very narrow laser linewidth (much narrower than the gas absorption line) is modulated ("dithered") at high frequency (say 10 kHz) by applying a sinusoidal component to the laser current ramp (increasing laser current is the normal method of tuning the laser across the spectral scan) with an amplitude that is small compared to the gas linewidth. So, if we modulate at 10 kHz and look at only the component of the detector signal at 10 kHz (using phase-sensitive detection), we would record a first-harmonic or first-derivative (1f) spectrum as shown in Fig. S2. Outside the spectral line and at the line center, the laser is jiggling left and right where no difference exists, so it records zero in these places, but has its maximum signals (negative and positive) at the side of the line where the slope is maximum.

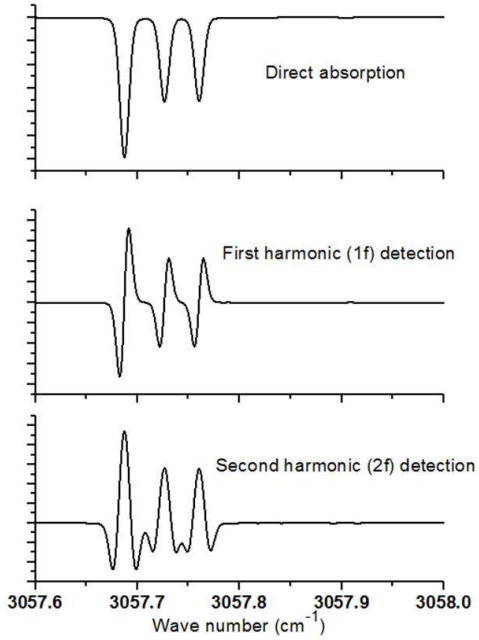

Fig. S2. Comparison of theoretical line shapes of direct absorption, first harmonic (1f) detection and second harmonic (2f) detection.

If we now modulate at 10 kHz, but look at the component of the laser light on the detector that is at 20 kHz, we would record (as we do on TLS) the second-harmonic or second-derivative (2f) spectrum seen in Fig. S2. Both 1f and 2f spectral signals are zero-based in amplitude and move the detection frequency to higher frequency (kHz) compared to the direct (DC) spectrum, where 1/f noise is lower. Thus the harmonic method produces higher signal-to-noise spectra. The 1f spectrum is not usually used since it can have small vertical offsets and the line center position is a zero-crossing rather than a peak. The 2f spectrum is preferred since it has its peak in the same place as the direct absorption spectrum, and moves the detection regime to the higher (20 kHz) frequency.

Spectral Data Processing:

The Beer-Lambert law models the optical transmission of light through an absorbing medium *(44)*:

$$I_\nu = I_0 e^{-k(\nu)\rho l}$$

where I_ν is the transmitted light intensity at frequency ν, I_0 is the incident light intensity, $k(\nu)$ is a line shaping function that may be Doppler, Lorenzian, or Voigt, although the Doppler lineshape is a close approximation at Mars atmospheric pressures. ρ is the molecular number density and l is the path length in cm. We use this model to determine the abundances of individual absorption lines present in our sampled measurements. The model needs many input spectral parameters for temperature dependence, air broadening, ground state energy, etc., and we use the HITRAN database for this information *(43)*. Direct absorption spectra produce good results for gases that have line center absorption depths of ~1% or greater. For higher sensitivity, we add a modulation to the laser current and then demodulate the returning detector signal at twice that frequency. This effectively gives us a second harmonic or 2f spectrum in which sensitivities of up to 2 parts in 10^5 are possible. See the section above and also Webster et al. *(44)* for a complete discussion.

Laser Power Normalization and Wave Number Scale

For a given channel (either CH_4 or CO_2/H_2O), TLS returns 3 spectra from the Herriott cell "science" detector, and 3 spectra from the reference channel detector. For both the Herriott cell and reference channel spectra, these 3 spectra are the direct absorption spectrum, the 2f spectrum, and a high-gain 2f spectrum. Our methane analysis is done using the 2f spectrum that is normalized to laser power from the direct absorption spectrum and mapped to a wave number scale using the reference detector signals. The high-gain 2f spectrum is not used since with only moderate gain increase (x16) it duplicates the 2f spectrum in signal-to-noise ratio but suffers from dynamic range restriction.

The TLS instrument also returns reference detector spectra recorded simultaneously with those from the science detector, and these are used to track the methane lines to provide the wave number scale for later processing. The methane signal (spectra)

detected by the reference detector (located inside the foreoptics, as shown in Fig. S1) is due to residual methane in the foreoptics. The foreoptics contribution to the science spectrum is equivalent to about 90 ppbv for sols 79-292 and much lower for subsequent runs. The 2-stage thermoelectric cooler on the IC laser keeps the lines in the same position during the scans, with drifts in line positions over all sols of only about 1-2 linewidths that are tracked successfully.

For an amount of gas at a given pressure and temperature, calculations using the HITRAN data base parameters *(43)* will predict the depth and width (distribution in wave number) of the absorption by the gas sample for all sampled frequencies, allowing us to then compare our recorded spectra to the spectra produced by the model. But, in order to make this comparison, we must first normalize the recorded data. This process that takes level 0 data (spectra) and produces level 1 data (spectra) entails:

Removing a "null pulse" which is a measurement of the background light taken with the laser off, and recorded during every one second spectrum that is averaged on board for our 2-minute downlinked spectrum. This allows us to determine the direct absorption with respect to a percentage of transmitted light (i.e. 1% absorption: 99% transmission).

Removing any DC offsets in the harmonic spectra (described below).

Fit the baseline of the spectra. This sloping baseline results from the fact that the laser output power increases as it tunes through different wave numbers.

Divide 2f spectra by DC baseline.

Assign a wave number (cm^{-1}) scale to the real spectra. We do this by using easily identifiable peaks of known wave number.

Once the raw spectra (level 0 data) are normalized (Fig. S3) as level 1 data, we can then use the HITRAN model to scale our real world data.

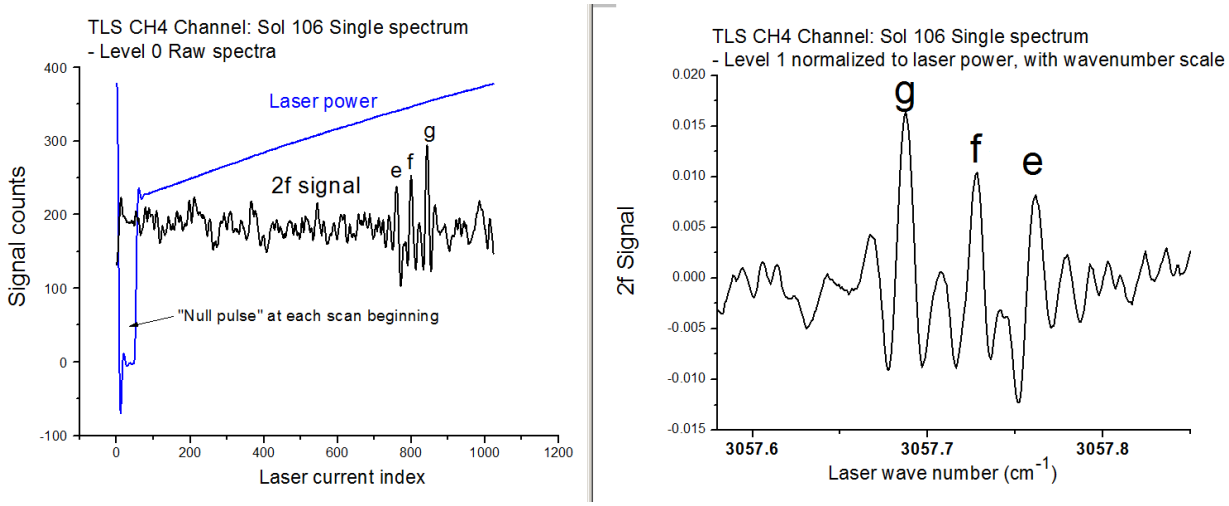

Fig. S3. Example of normalization of a real single spectrum (2 min.) downloaded for sol 106. The methane triplet lines e, f, g can be identified from Table S1 above. The left panel is the complete level 0 spectra, whereas the right panel that shows level 1 data (same 2-min. spectrum normalized to power and given wave number scale) has been expanded in wave number to show the methane lines used and the occurrence of optical interference fringes that limit the detection method for a single 2-min. spectrum.

Producing Abundances

Using temperatures and pressures from our instrument for input, we iteratively run the model, varying the abundance in a converging algorithm until the synthetic spectra for the single line is the same size as our real spectrum (within some determined threshold). The convergence criteria are set to optimize for the 2f spectra.

For the methane analysis, we generate two results, one named "peak-to-peak" that returns the peak-to-peak signal amplitude (actually central peak to lobe-average) values, and a second named "integral" that returns the area of the 2f line between and above the bottom lobe minima positions (wave number). The peak-to-peak method finds the signal amplitude of the 2f maximum and lobe minima average, and is our preferred method since it produces somewhat lower scatter in our data, although results for either method are very close. The integral method, which is used for retrieving H, C, O isotope ratios *(31)* uses the following algorithm:

Find the global max of the 2f absorption spectra (peak)

Find the two local minima (2f lobes)

Fit a line between the two lobes

Using the lobes as integration boundaries, find the area between the fitted line and the spectra for both the direct and 2f spectra. Ratio this area between real and synthetic spectra and if ratio is outside the convergence threshold, iterate with new abundance.

Once the measurements converge, we ratio the resulting areas of the real spectra to the synthetic spectra which has a known abundance. For both methods, using the same laser modulation and gain throughout (pre-launch calibration and all Mars measurements), we relate the 2f signal size to the direct absorption size through calibration as described below, and like any flight project, we rigorously run our experiment as tested and calibrated pre-launch.

<u>Calibration:</u>

When analyzing direct absorption spectra with known pressure, temperature and path length, a Beer's law calculation using spectral line parameters from HITRAN *(43)* can in theory provide the gas abundance without the need for calibration gases (i.e. someone else did the work when they created the data-base). However, calibration gases serve the dual purpose of verifying the spectrometer response (a check of pathlength or number of passes in a cell, laser linewidth, pressure, mode purity, temperature, saturation, etc.) and also giving a direct calibration (relationship) between the direct absorption and the 2f channel with its various different gain stages.

The relative methane abundances reported here are calibrated using NIST-traceable methane in air provided by the NOAA-CMDL laboratory (provided by Jim Elkins group) specified to contain 88 ±0.5 ppbv. By injecting this gas into the TLS Herriott cell during pre-launch calibration runs of TLS and SAM in the NASA GSFC environmental chamber, we record both direct absorption and 2f signal sizes using the same conditions (e.g. laser scan, modulation, flight electronics and software, Herriott cell temperature and pressure, ramp heater) used on Mars. During the calibration run, the foreoptics is pumped

out so that there is no contribution from foreoptics gas. The path length of the Herriott cell was verified to be 81 passes based on direct absorption measurements of these same methane lines using a second calibration cylinder (same provider) at 1800 ppbv. In addition, by adding pure methane gas at low pressures so that the lines are bleached to zero light transmission at line centers, the mode purity during the scan is verified. No change in alignment or detector signal sizes has been detected since pre-launch. Normalizing the mean value retrieved to 88 ppbv gives us a calibration result and uncertainty of 88.0 ±1.13 ppbv. We note that this absolute uncertainty of ±1.13 ppbv does not carry forward in our difference method described below, since it would only serve to change the mean value and upper limit slightly (by ~1 part in 88).

The foreoptics contribution to the difference method:

The difference method is described in the body of the main paper, and the sequence shown in Fig. S4 below. During the empty or full cell periods, the foreoptics and Herriott cell pressures are very stable; during a typical run (Sol 106) the temperatures and foreoptics pressure are stable to 0.02%, and the Herriott cell pressure during the full cell section is stable to 0.1%.

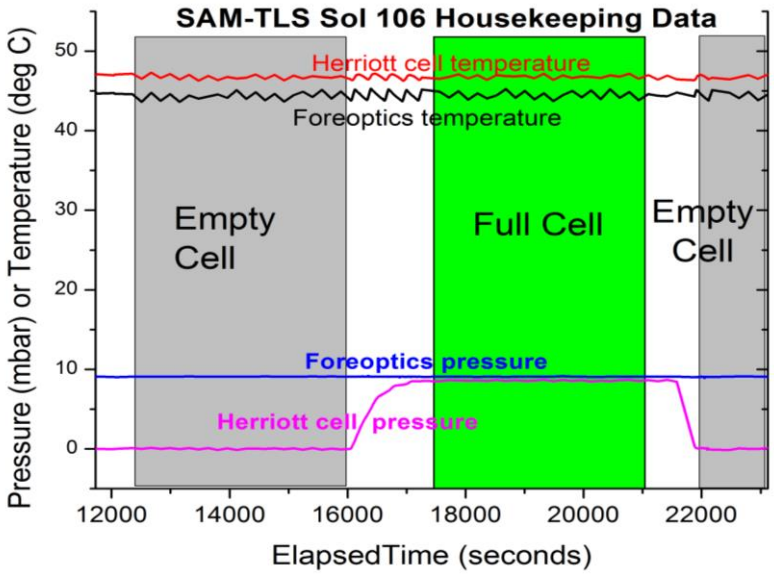

Fig. S4. Housekeeping data from a single methane run (Sol 106) showing experiment sequence of 26 empty cell scans, 26 full cell scans, and 6 empty cell scans. Although the foreoptics pressure is different for some runs (see Table 1), note that the foreoptics chamber pressure is constant during the empty and full Herriott cell runs on any given sol. For sols 306 and 313, the foreoptics pressure was first reduced to zero. The Herriott cell and foreoptics temperatures show the saw-tooth like effect of the small ramp applied to the heater to wash optical interference

During the long pre-launch activities in Florida, the foreoptics chamber leaked up to a significant pressure (~76 mbar) by the time we arrived at Mars. This pressure included terrestrial "Florida air" from the launch site that contained significant terrestrial methane gas (~10 ppmv) that showed up as a large methane signal (spectrum) on the Herriott cell science detector for both "empty" and "full" Herriott cell data, since the beam made one

pass through the 9-cm length of the foreoptics. Results from these runs made before sol 79 were discarded and not included in the analysis. To reduce the foreoptics contribution, we pumped down the foreoptics chamber in a series of steps for subsequent sol runs (80, 33, 11.5 mbar) until at 11.5 mbar we observed no detectable increase (or reduction) in the empty or full cell spectra with time over the run, so that we were confident that the leakage was negligible during the runs to follow. To eliminate any residual concerns regarding possible leaks between the foreoptics and Herriott cell during the run, for sols 306 and 313 we further reduced the foreoptics pressure to close to zero by pumping on the chamber.

Because of the foreoptics contribution, all of our spectra (empty and full Herriott cell) look somewhat like those in Fig. S3 since (in the absence of significant Martian methane) they are dominated by the foreoptics contribution. We then process them as described above, and then look for differences in the empty and full cell results. Specifically, the "full" cell methane spectra are first processed as if the observed methane spectrum came only from the Herriott cell, that is, we use the measured Herriott cell pressure and temperature to retrieve a "full cell" methane mixing ratio by comparison with HITRAN. Then for the "empty" cell spectra, we use the same mean temperatures and pressures of the full cell and process the empty cell spectra to reveal the "empty cell" methane mixing ratio. This method makes the difference method most sensitive to Herriott cell methane from Mars, should it be there. If there were no methane on Mars, the empty and full cell results would be identical. If there were 20 ppbv methane on Mars, the full cell result would be 20 ppbv larger than the empty cell result. For sols 79-292, for example, both the empty and full cell results are close to 90 ppbv, and for sols 306 and 313 it is <20 ppbv. For the difference data given in Table 1, the mean empty cell values for that specific run have been subtracted from the mean full cell values to provide the resulting Martian methane mixing ratio.

The "methane enrichment" and "hybrid" experiments:

For direct ingest runs (lower precision), inlet 2 (see top right corner of Fig. S5) is used. It is a 3/16" internal diameter stainless steel tube heated to 50^{o}C containing a dust filter of sintered Inconel 0.5 micron particles that is located on the rover side ~1 m above the Martian surface, and was pointed at a variety of directions relative to the nominal wind direction.

On two occasions we conducted "methane enrichment" experiments that effectively increase the methane abundance in the Herriott cell by removing ("scrubbing out") a large part of the main atmospheric component, carbon dioxide. In these runs, the Mars atmosphere is ingested through a second inlet (Inlet 1 in Figure S5 below) and led to the TLS Herriott cell by passing over a CO_2 scrubber cell filled with Linde 13X molecular sieve material. Once the Herriott cell is pumped out, the Mars atmosphere is ingested along the path shown in Fig. S5 until the TLS cell is either at 90% of the Mars ambient pressure of ~7 mbar, or two hours have gone by. For the two enrichment runs, we typically produced 4-5 mbar of enriched atmosphere in the Herriott cell after the two-hour limit. The script for the enrichment runs was thoroughly tested in the SAM test-bed at NASA GSFC in a series of 3 runs aimed at determining "the enrichment factor (EF)", during which a "Mars mix" of known abundances (50 ppbv methane in this case) was used, where TLS measured the methane abundance before and after the enrichment, and

for the "empty cell". Using an N_2/Ar ratio approximating that expected on Mars, a value for EF of 24 ±2 (95% CI) was first obtained, modified to 22 ±2 (95% CI) with a more accurate N_2/Ar ratio from a separate gas mixture in a subsequent run.

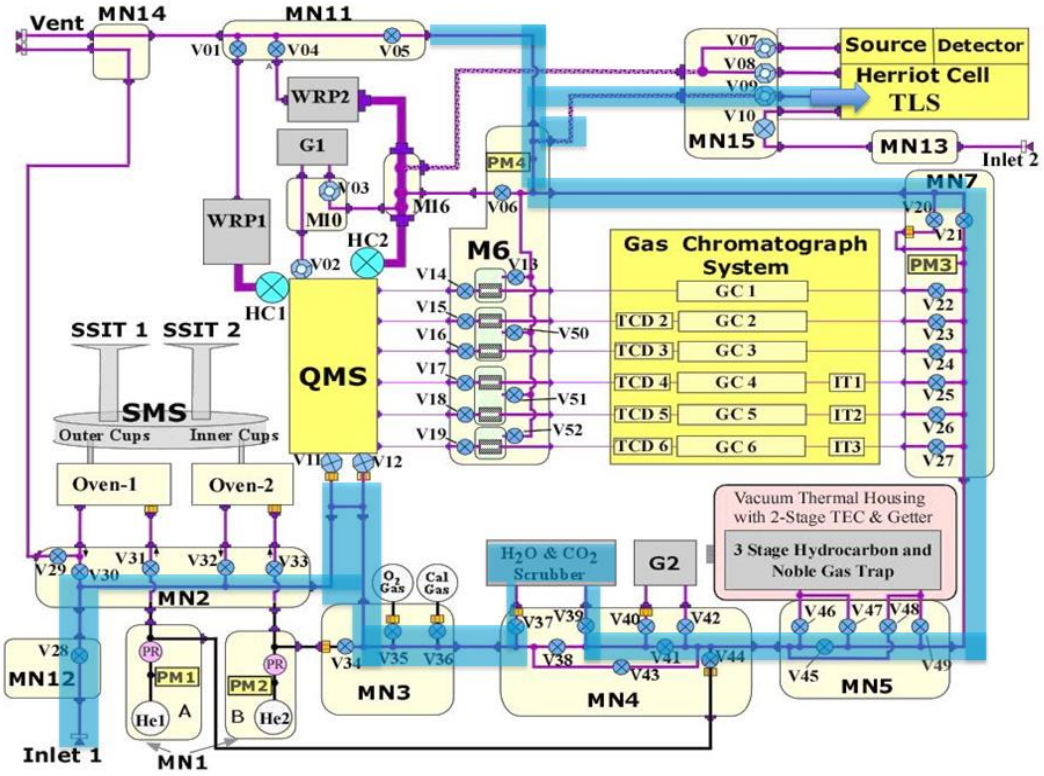

Fig. S5. The SAM gas handling and routing schematic. V=valve, MN=manifold, SMS=sample manipulation system, WRP=wide range turbomolecular pump. The broad blue highlight shows the path taken by the ingested Mars atmosphere during the enrichment experiments. The lower precision "direct ingest" runs ingest Mars atmosphere through the shorter path from Inlet 2 and manifold MN13 into the Herriott cell.

Because our first enrichment run on Sol 573 produces a very low value for methane in contrast to the earlier "high methane" runs, we modified the methane enrichment script to append a direct ingest run immediately after it, and called this our "hybrid methane" script. This was also tested in the SAM test bed at NASA GSFC, and produced consistent enrichment factor of 23 ±1 (95% CI) even though it was conducted months after the first run with many other test-bed studies in EGA mode done in between.

Data Analysis:

Through the SAM central data handler (CDH), the Curiosity rover returns two-minute averaged spectra from TLS (direct absorption and 2f spectrum for both Herriott cell and reference gas cell) that show the three spectral absorption lines given in Table S1. We treat each of these lines as a separate estimate of the absorption attributable to methane somewhere along the optical path. These absorptions were converted into an apparent methane mixing ratio in the Herriott cell by assuming that this is the only region in which methane occurs.

Changes to data processing since the first Science paper (33) results: All our data have now been reprocessed with the same new algorithm that reduces any susceptibility to variations in the laser plate temperature by automatically rejecting the few 2-minute points that resulted from a laser plate temperature changing by more than 0.1 deg/minute. The need for this quality control is because the spectral lines will blur somewhat during the 2-minute average by an amount dependent on the laser plate temperature; the faster the laser plate temperature changes during the 2-minute collection, the smaller the methane spectral lines will be in depth. Although it is true that our integrated area under the spectral line will take care of this, it is not perfect since we integrate not across the full lineshape, but across the area between the second harmonic lobe positions (still most of the line). Not all runs require point removal, and point removal can result in either or both the full or empty cell runs. The most significant change that this reprocessing produces is for the daytime run of Sol 306: removing the few low points that were associated with a fast-moving laser plate temperature results in raising the mean value of the full cell abundance to produce the now-high retrieved value for the daytime abundance (Table 1 and Figure 1).

Comparing the data for the six observations of sols 79-313 in this paper with those in Webster et al. (2013), the results for sols 81 and 292 are rather similar, while those for sols 79, 106, 306, and 313 are different. Using the current data, the published value of 0.18 ± 0.67 ppbv and the upper limit of 1.3 ppbv in Webster et al. *(33)* should be revised to 0.88 ± 0.81 ppbv and 2.2 ppbv, respectively. Although the revised mean for this 6-sol group is 0.88 ppbv, at 95% confidence level the upper limit is 0.88 +1.645*SEM = 2.2 ppbv, because in this case a one-sided Student distribution needs to be considered for upper limits.

Averaged Spectra:

We choose to partition our data points of Fig. 1 into 3 groups for independent analysis: (i) the "low methane" direct ingest results of sols 79, 81, 106, 292, 313 and 684; (ii) the "low methane" enrichment results for sols of 573 and 684; and (iii) the "high methane" four sequential runs of sols 466, 474, 504, and 526, since each of these groups shows no significant variations within. The daytime result of sol 306 is not included. The averaged spectra for these three groups are plotted in Fig. S6 below where a definitive increase in signal size (integrated area) is evident for each line in the methane signature.

Figure S6 follows on next page.

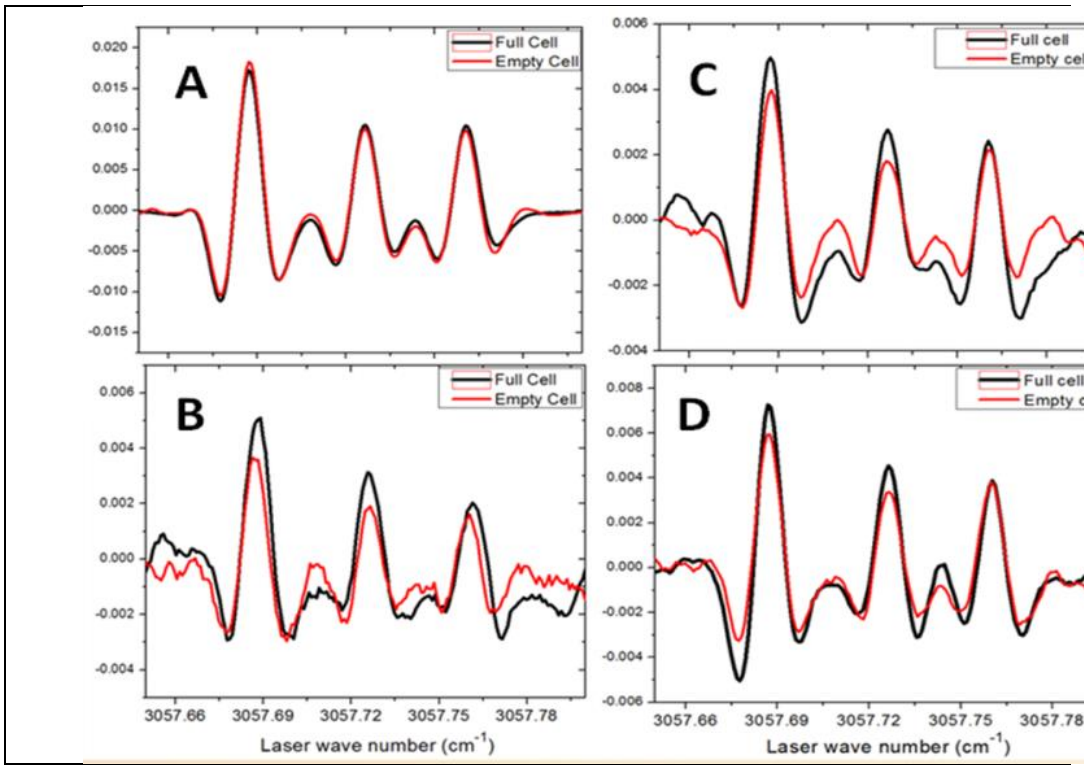

Fig. S6. Visual comparison between full and empty cell average spectra: A. "Low methane" from Sols 79, 81, 106, 292, 313 and 684; B. "High methane" from Sol 474 only; C. "High methane" from Sols 466, 474, 504, and 526; and D. "Low methane" from the enrichment experiment sols of 573 and 684 before dividing the difference by the enrichment factor of 23.

Computation of mean values, standard error of the means and confidence intervals:

For each sol, the average net signal $\overline{Net}$ (in ppbv) is obtained from the Full and Empty cell analyses from the following equation:

$$\overline{Net} = \overline{Full} - \overline{Empty} \quad \text{(S1)}$$

where $\overline{Full}$ and $\overline{Empty}$ are the mean values of the Full and Empy cell analyses for a given sol.

The variance is thus:

$$\sigma^2_{\overline{Net}} = \sigma^2_{\overline{Full}} + \sigma^2_{\overline{Empty}} \quad \text{(S2)}$$

which is estimated by means of replication:

$$\frac{s^2_{Net}}{n_F} = \frac{s^2_{Full}}{n_F} + \frac{s^2_{Empty}}{n_E} \quad \text{(S3)}$$

where n_F and n_E are the number of Full and Empty cell analyses acquired on a given sol. The value $\frac{s_{Net}}{\sqrt{n_F}}$ calculated from Eq. S3 is given in Table 1 as the Standard Error of the Mean.

The 95% Confidence Interval is given by:

$$\Delta\overline{Net} = \pm\frac{s_{Net}\, t(P,df)}{\sqrt{n_F}} \tag{S4}$$

where the critical values of the t-distribution are taken for a significance level P of 95% and the degrees of freedom $df = n_F - 1$. Note that usually $n_F \approx$ 25-30, and thus the critical value is close to2, which is the value we considered in Table 1.

The mean net values provided for each series ("low methane", "low methane with enrichment", "high methane") are calculated as the average of all individual 2-min full cell analyses of that series, from which the average empty cell of the corresponding sol is subtracted, i.e., net values are calculated for each sol with the appropriate background, and then are averaged over all the sols of that series. The mean value can thus be written as:

$$\begin{aligned}\overline{Net} &= \frac{1}{n_{F,tot}}\left[\sum_{i=1}^{n_F(1)}\left(Full_1(i) - \overline{Empty\,(1)}\right) + \sum_{i=1}^{n_F(2)}\left(Full_2(i) - \overline{Empty\,(2)}\right) + \ldots\right] \\ &= \frac{1}{n_{F,tot}}\left[\sum_{k=1}^{n_{F,tot}} Full(k) - \sum_{j=1}^{N} n_F(j)\,\overline{Empty\,(j)}\right]\end{aligned} \tag{S5}$$

where indices 1, 2,…, N correspond to the sol index within a series, $n_F(j)$ is the number of full cell analyses performed on the j^{th} sol, and $n_{F,tot}$ is the total number of full cell analyses over the given series. $\overline{Net}$ refers here to the mean net values of that series, while $\overline{Empty\,(j)}$ is the mean of the Empty cell analyses measured on sol j.

Although the Full and Empty cell values exhibit some non-random fluctuations over different sols, the set of net values is randomly distributed over each series. A possible real (non-random) variation of the net signal may be observed during the enrichment series (as reflected by the different mean values obtained on sol 573 and 684, although confidence intervals overlap), so that the estimated standard deviation of the net values may be overestimated for that series.

Since only mean daily values of the background were subtracted from individual Full cell analyses, the variance of the net signal as calculated from Eq. S5 only reflects the variance of the Full cell analyses. In reality, the variance of the net signal is the sum of the variances of the Full and Empty cell analyses. Since both are similar to a good approximation, the real variance of the net signal should be $\approx 2\, s_{Net}^2$ (where s_{Net}^2 is the variance calculated from the dataset of net values described above). As a result, the SEM and Confidence Intervals for the mean values of each series are calculated as:

$$SEM_{\overline{Net}} = \frac{\sqrt{2} \times s_{Net}}{\sqrt{n_{F,tot}}} \quad \text{(S6)}$$

and

$$\Delta\overline{Net} = \pm \frac{\sqrt{2}\, s_{Net}\, t(P, df)}{\sqrt{n_{F,tot}}} \quad \text{(S7)}$$

with $df = n_{F,tot} - 1$ degrees of freedom. With this approach, the uncertainty on the Empty cell values is also taken into account.

Supplementary Text

Correlations with other measured parameters:

Correlations with other measurements have been described in the main text, and the data plots are presented below.

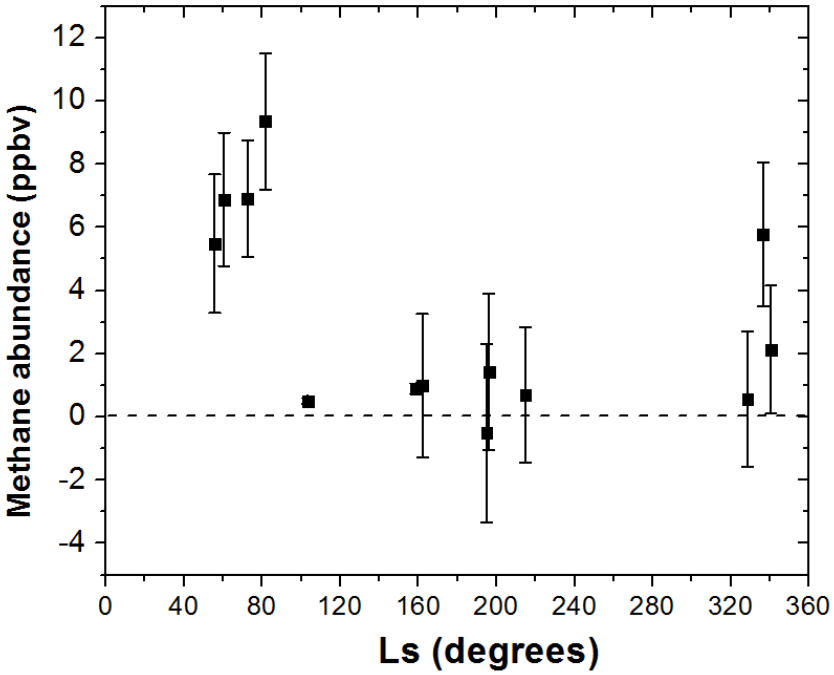

Fig. S7. Plot of TLS methane abundances vs. solar longitude (degrees).

Figure S8 follows on next page.

Panel A:

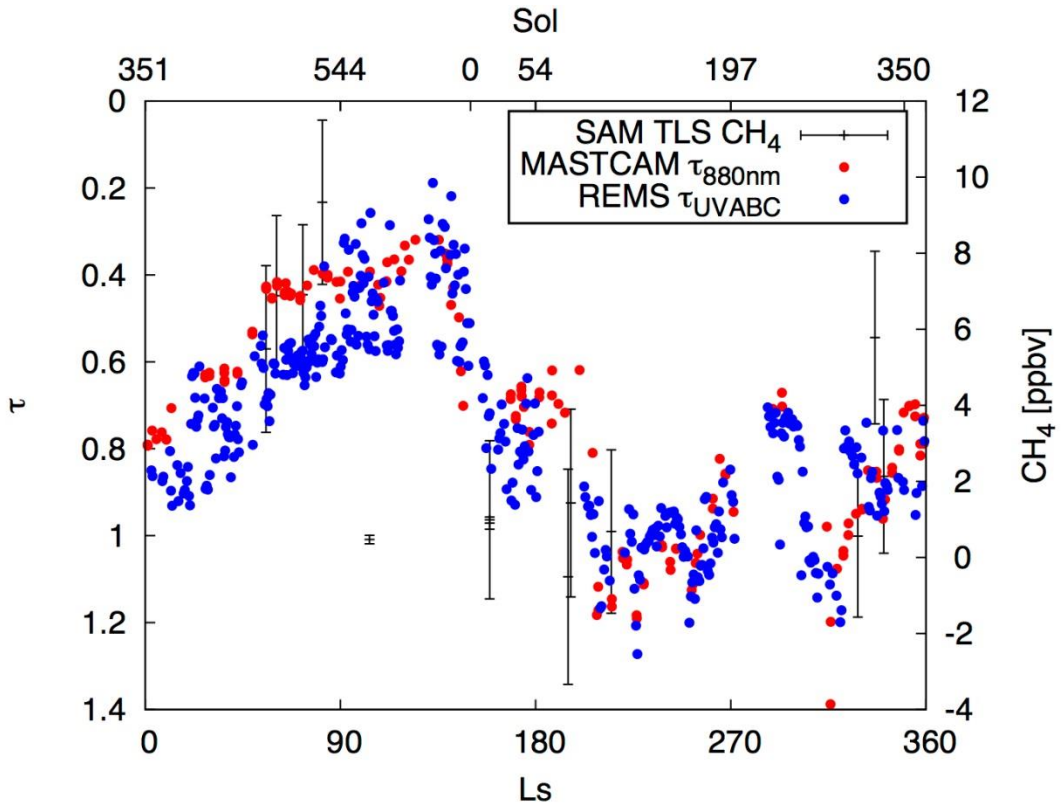

Panel B:

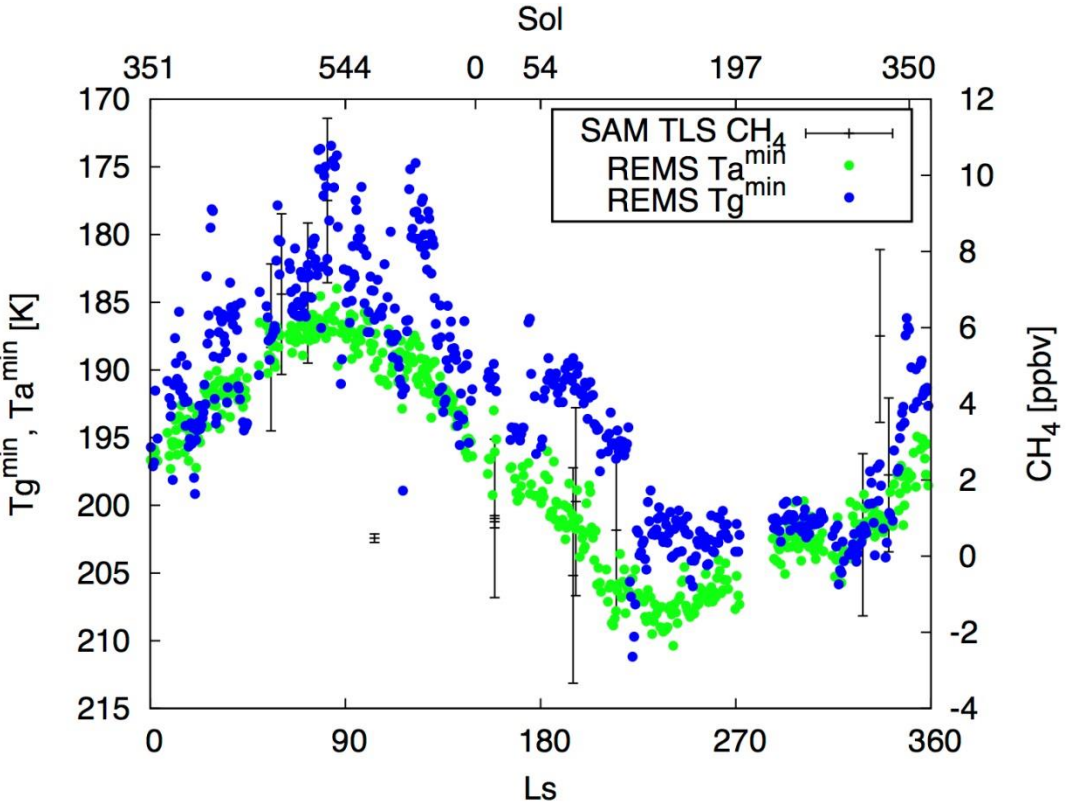

Panel C:

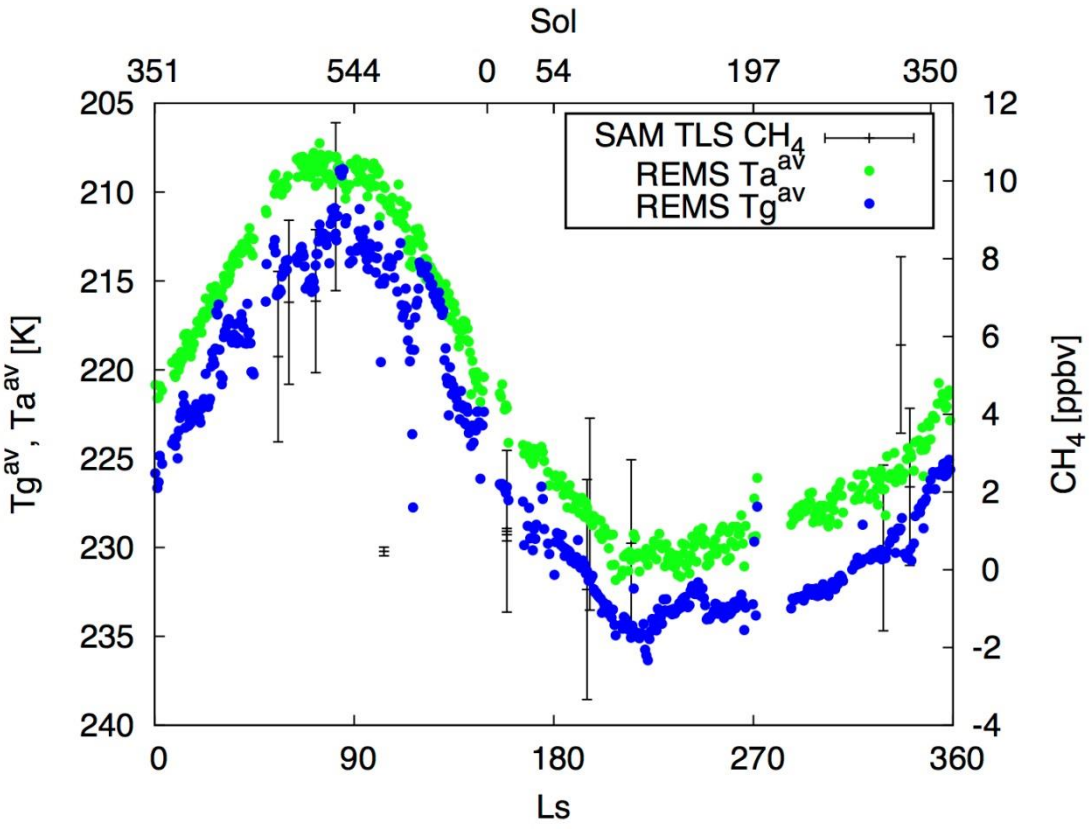

Panel D:

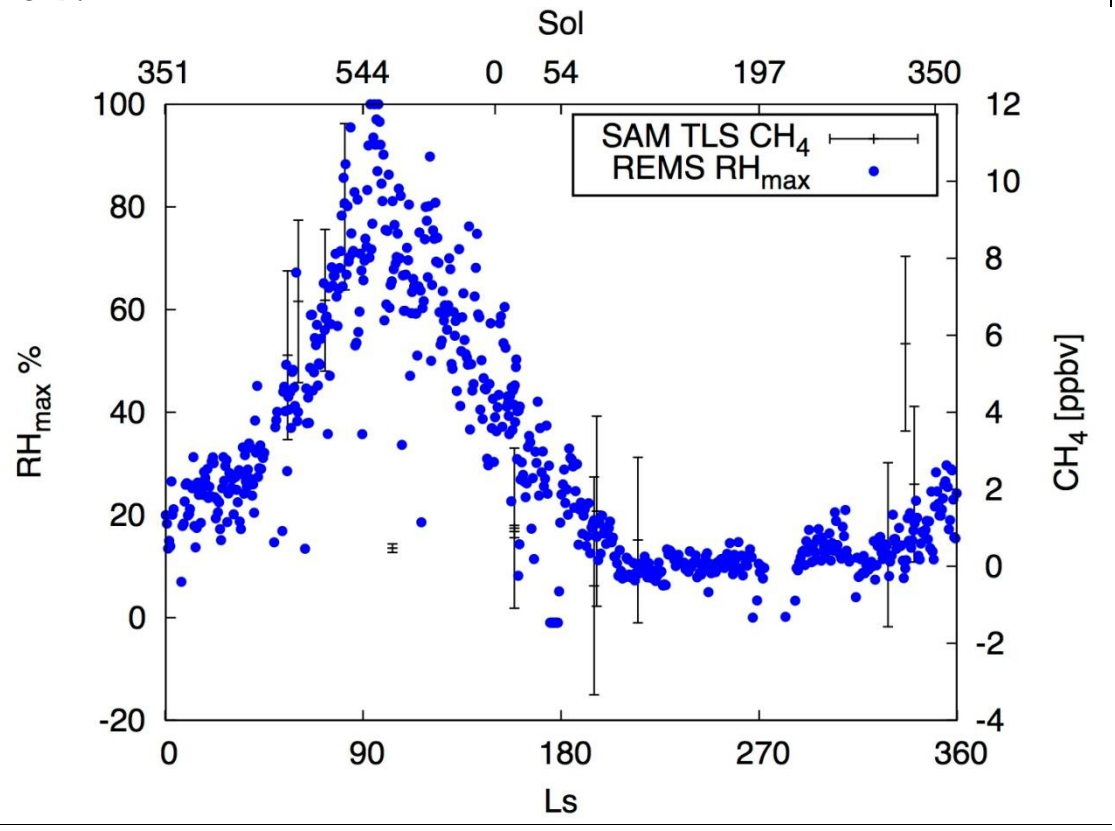

Panel E:

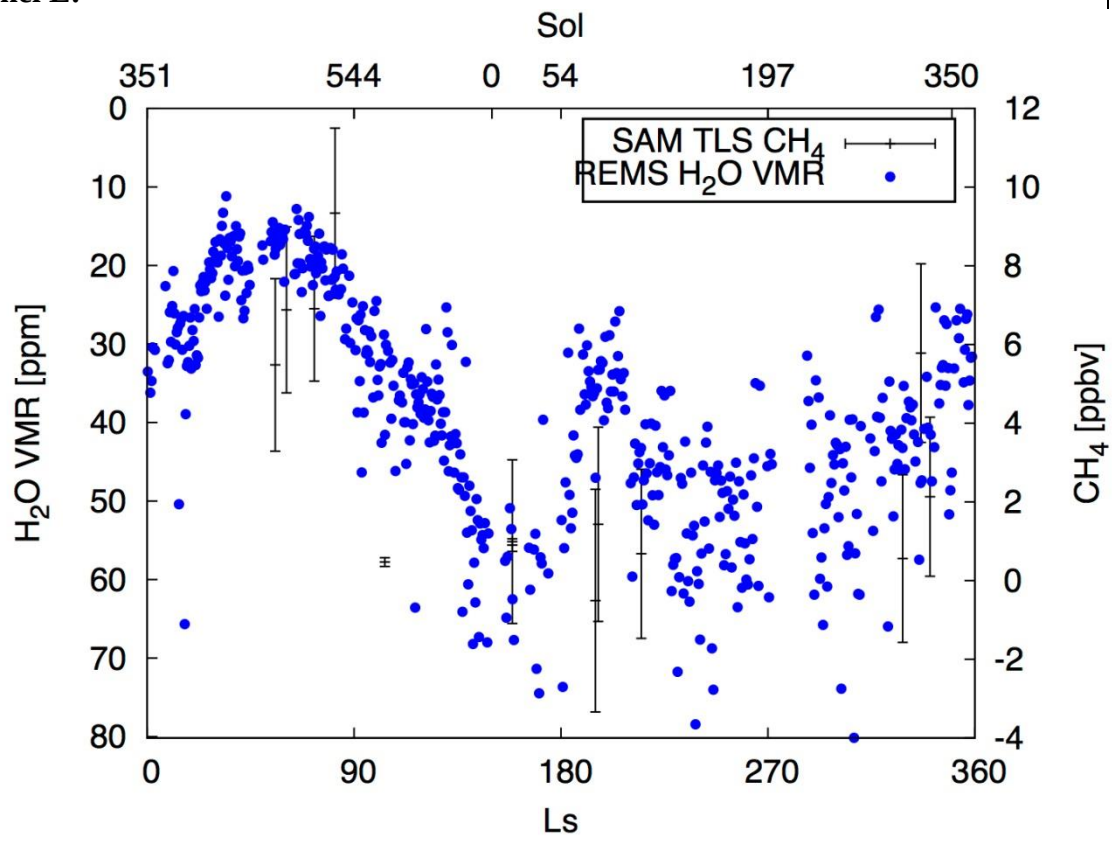

Fig. S8. **Panel A:** Comparison between TLS methane measurements and dust opacity measured by MSL's mast camera (MASTCAM) at 880 nm and by the REMS instrument across UV-abc wavelengths. **Panel B:** Comparison between TLS methane measurements and the minimum ground (Tg) and air (Ta) temperatures as measured by REMS. **Panel C:** Comparison between TLS methane measurements and the average ground (Tg) and air (Ta) temperatures as measured by REMS. **Panel D:** Comparison between TLS methane measurements and the maximum daily relative humidity RH as measured by REMS. **Panel E:** Comparison between TLS methane measurements and the in situ water vapor volume mixing ratio (vmr) as measured by REMS.
For a description of REMS and MASTCAM, see *(36)* and *(39)*.

Figure S9 follows on next page.

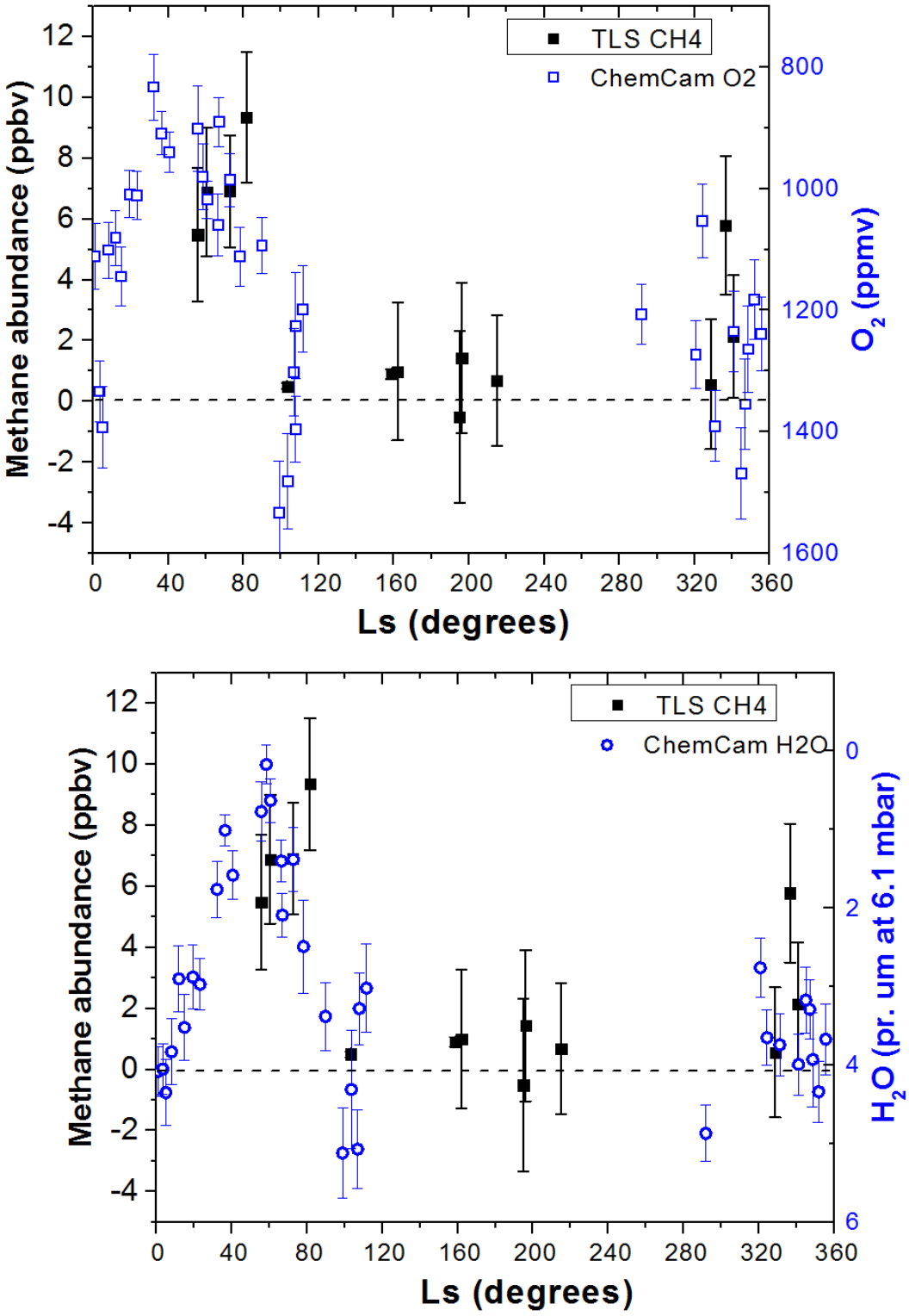

Fig. S9. Comparison between TLS-SAM methane measurements and preliminary ChemCam oxygen (top panel) and water (lower panel) column abundances, the latter

plotted in precipitable microns at 6.1 mbar. The preliminary ChemCam data is from the presentation by McConnochie et al. *(37)* at the 8th Mars International Conference (2014).

Regarding the Curiosity rover location during the TLS methane measurements, the "high" methane results were all obtained in one region near Everett, as shown below in Fig. S10.

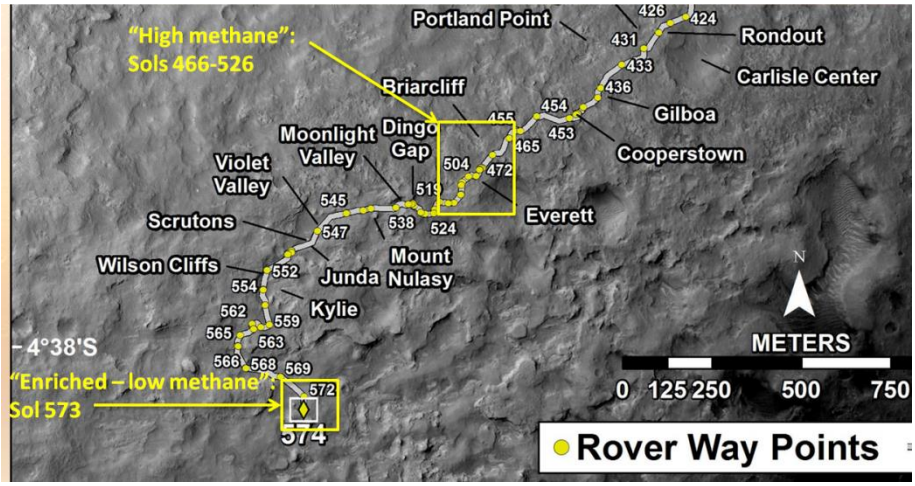

Fig. S10. Schematic showing the Curiosity rover's location during the observations of "high" methane, near Everett. The subsequent low value observed for sol 573 was only ~800 m away.

Arguments against terrestrial contamination:

During evolved gas analysis (EGA) runs conducted by SAM, a portion of gas from a specific temperature cut containing helium carrier gas and gases evolved from the sample during pyrolysis is delivered to TLS primarily for isotopic analysis (H, C, O isotopes). During these runs, we also measure high levels (typically ~10 ppmv) of methane produced from the decomposition and reaction products of N-Methyl-N-tert-butyldimethylsilyltrifluoroacetamide (MTBSTFA) present in the sample system as a terrestrial contaminant *(45)*. Measured values of $d^{13}C$ in the evolved methane are in the range of -40 to -100 per mil. The occurrence of these EGA runs is plotted along the bottom of Figure 1 in the main body of the paper. In light of this known contamination, we here consider scenarios by which this source of terrestrial contamination could be responsible for our methane detection at both high and low values, and present arguments below to rule these scenarios out.

Hypothesis: The observed methane is the result of incomplete pumping out (evacuation) of the Herriott cell:

From observed signals comparing the Mars atmospheric carbon dioxide (~96% pure) to those of an evacuated cell, we measure that the cell is pumped to <0.007 mbar, so that 10 ppmv CH_4 in 10 mbar He could leave a few ppbv methane after the end-of-EGA evacuation. However, before and after each atmospheric ingest reported here (performed days to weeks after EGA runs), the cell is again pumped out to <0.007 mbar, so that the contribution would be negligible. Moreover, the 4 "high methane" results

were recorded over a continuous period spanning 60 sols during which time no EGA runs of any kind were made, yet the 4 methane values remained consistently high. Note also that several earlier measurements made after RN, JK and CB sample analysis (see Fig. 1 caption) are low, not high.

Hypothesis: There is a coating (MTBSTFA or reaction products) inside the Herriott cell that emits methane after reacting with ingested Mars atmosphere. This coating has built up over time, and may have been cleaned/removed by the combustion run leading to the lower methane values in the subsequent (enriched plus hybrid) runs. The empty cell would not show methane that would appear only once Mars atmospheric gas is ingested.

We first note that both the Herriott cell interior and its primary mirror pair are both gold-coated, and can be considered the same surface for film coating or reaction. Because the interband cascade (IC) laser used for methane detection bounces 81 times between mirror surfaces, changes in the transmitted laser power provide a very sensitive detection of any film build up inside the cell. Figure S11 below shows that the methane laser power has not significantly diminished since landing, and if anything shows a minor trend toward higher power (cleaner mirrors). The measured 1SEM scatter in the data is only ~0.1% over the whole time period, and this change in laser power would require a change in mirror reflectivity of only ~10 parts per million! Should a putative polymeric type film cause such a change in reflectivity as a loss (absorption), we calculate that this tiny absorption could result from a film of 5×10^{-3} monolayers thick. Although very small, if every molecule of such a fractional layer was converted somehow to one molecule of methane, a few ppmv of methane could result in the 7 mbar Herriott cell when full. Therefore, any methane production from such a contamination must be limited not by the tiny film thickness, but by the available putative reactants ingested from the Martian atmosphere. We also know from full cell and before-and-after-empty-cell measurements that no trend is observed on any run over time (30 mins for each component, typically), so that any such chemistry must be very fast (less than a minute or so) and then immediately terminate.

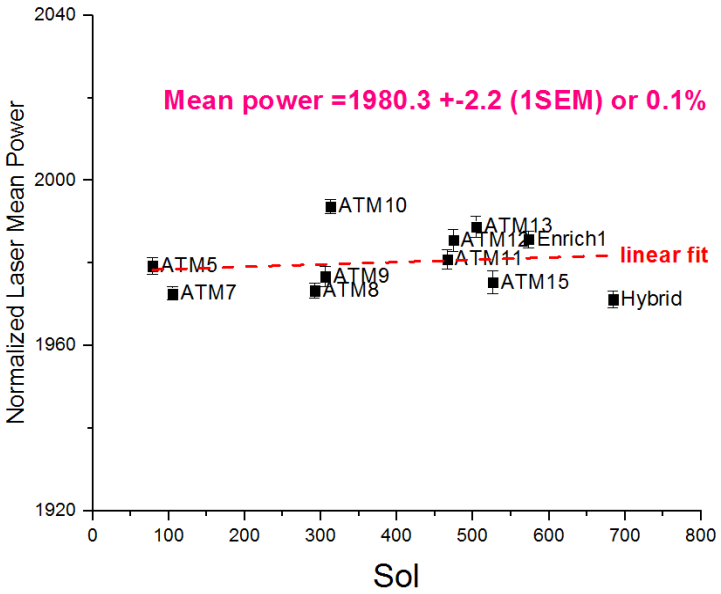

Fig. S11. Normalized mean laser power of the Interband Cascade (IC) laser as a function of Martian sol, showing no significant change over time. If anything, a linear fit shows a slight trend toward increasing power (cleaner mirrors). Because the IC laser beam bounces 81 times between Herriott cell mirrors, this implies no change to mirror reflectivity within a few parts per thousand. Enrich 1=first enrichment run; Hybrid=direct ingest + second enrichment run.

Should this mechanism be occurring, we need to question exactly what Martian gases would be involved in this fast chemistry to produce methane? And what would the proposed surface coating be made of? We consider ozone at 10-200 ppbv, or hydrogen peroxide at <40 ppbv that potentially could react with a surface coating. Although methyl propene was first suggested as a potential "coating" material since it is a known byproduct of MTBSTFA degradation, this is ruled out since it is highly unlikely that methyl propene is adsorbed to surfaces, since it is much too volatile at 10 mbar (comparable to chloromethane). Better candidate MTBSTFA products that are more likely to condense on surfaces at 45 ^{o}C, 10 mbar, are the silylated water products, tert-butyldimethylsilanol and 1,3-bis(1,1-dimethylethyl)-1,1,3,3 tetramethyldisiloxane identified by SAM or something like the C4 ketones or aldehydes that have been seen in lab analog studies.

Regarding the possible "cleaning" effect of the combustion run, we rule this out since the EGA runs themselves produce oxygen at measured values (QMS) higher than the oxygen accompanying the combustion experiment temperature cut given to TLS.

Note that the TLS Herriott cell is maintained at 45 ^{o}C and only occasionally sees the EGA experiment. TLS receives a "temperature cut" (ingested gas from a predetermined oven temperature range) only ONCE per EGA run - not continuously - and this is a single 400 cc volume of mainly He at 10 mbar with EGA products fed to TLS.

In summary, we conclude that the possibility of terrestrial contamination producing the "high" methane signals is very unlikely, and with no evidence to back this scenario, we rule it out for the following main reasons:

There is no evidence of a coating/film that formed inside the TLS Herriott cell. Measured laser light level changes during the mission can accommodate no more than 10^{-3} monolayer at most.

The earlier TLS methane data do not show any increase after 15 (!) EGA runs (RN, JK, CB1-3, BK's), with the "high methane" occurring suddenly after an additional 3 EGA runs (CB5-7) and then disappearing after a single combustion run that is not significantly different to TLS than a standard EGA run of an oxygen-containing sample.

It is difficult to identify atmospheric reactants and chemistry that would react with any putative film or coating inside the Herriott cell to produce methane. During SAM EGA the QMS has not detected any atmospheric oxidants that could react with any coating in the TLS at 45 ^{o}C that would release methane.

While there is no evidence to suggest an analytical problem despite an exhaustive search for one, such a short-lived elevated methane signal is surprising. Given its transience, an undetected analytical problem cannot be ruled out. Continued measurements of the atmospheric methane abundance, especially using the enrichment procedure, may further establish the reliability of this detection, and possibly of the recurrence frequency of elevated methane concentrations.

<u>Study of Curiosity Wheel Degradation and Changing Terrain during Transit:</u>

Because the observation of high methane occurred on four sols only, rover motion and geologic features of the terrain had to be excluded as possible methane release mechanisms in the unlikely scenario of methane being trapped in voids in crushed rocks, particularly since the Curiosity wheel degradation occurred during transit over harsh environments. The wheels themselves are made of aluminum, and there is no possibility that the wheel degradation can itself produce methane, but a two-ton rover traversing over differing rock terrain may crush rocks and somehow release methane in some places and not others. Therefore, the following correlations were tested against the high methane results: a) rover stand time, b) general terrain features, c) geochemistry of individual rocks.

a) Rover stand time

Rover stand time is the time elapsed between the last wheel motion and the ingest of atmosphere into the SAM instrument. To calculate this, the difference between the time of last wheel motion (extracted from the rover motion protocols) and the ingest start time (from the SAM protocols) was calculated (Fig. S12). All four observations of high methane (sols 466, 474, 504, 526) were made after relatively short rover stand times (Fig. S12). Within those four sols the longest stand time of ~36 hours occurred on sol 466, sol 526 had ~23 hours stand time and sols 474 and 504 ~11 hours. Similarly short but also long stand times (up to 555 hours) are related to low methane observations. Heating of the ground from the RTG as a cause for high methane measurements can be excluded as it would increase with time, which is not seen.

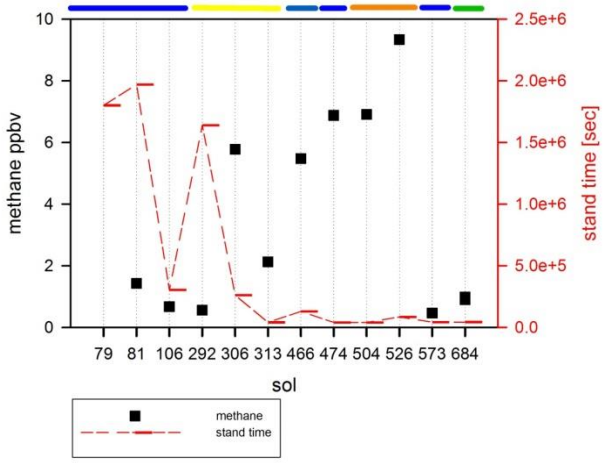

Fig. S12. Diagram relating rover stand time and terrain classification to the methane measurements. Methane measurements are plotted in ppbv, for error bars refer to Fig. 1 and Table 1 one in the main manuscript. Mean values of high methane (left axis and black squares) were taken from sols 466, 474, 504, and 526, all other sols are classified as 'low methane'. Note that sols 306 and 526 are daytime runs. With this in mind, sol 306 is classified as a low-methane result. Unit of rover stand time is seconds, because the basis for the calculation is the spacecraft clock. Bar above the plot represents terrain classification from orbital mapping, whereby grey-blue, yellow and orange colors represent increasingly more rough terrain, while green and blue represent smooth terrain.

b) General terrain features

Considering next the release of methane from crushing of rocks or disturbing soil while driving we take the following factors into account: rover stand time and the classification of the terrain from mapping (Fig. S12) and elevation . Elevation of the ingest location does not correlate with the methane measurements. The overall distance driven is a measure of the rover location and is best represented by the terrain mapping (bar above Fig. S12). Observation of high methane occurred over terrain classified as smooth (blue) and rough (orange), and low methane observations also occurred over both types of terrain, excluding a direct correlation between orbiter data based terrain classification and the methane observations.

c) Geochemistry of individual rocks

To further test a correlation of rock properties with the observation of high methane, we next turn to the chemistry of rocks and soils as measured by APXS *(41)*. Because the rover wheels crush and disturb rock fragments and soil along the traverse randomly, we therefore do not select individual measurements or attempt to single out rock classes but, rather, test chemical data grouped around the sols of the methane experiments. We tested the entire range of elements measured by APXS (Na, Mg, Al, Si, P, S, Cl, K, Ca, Ti, Cr, Mn, Fe, Ni, Zn, and Br) and show selected diagrams in Fig. S13. We investigated elements important for rock forming minerals (Fe, Mg for olivine and pyroxene, Na, K for feldspar plotted vs Si, all as oxides) and elements important for later fluid rock interaction (Ca, S for sulfates, Cl, Br for evaporation processes, Zn for hydrothermal processes; all as oxides). None of the plots shows any correlation between the

observation of high methane and the rocks in the immediate area of the rover position at ingest. Since the diversity of rocks crushed by the rover wheels is likely similar to the diversity measured by APXS (but exceptions may exist), and no correlation is observed between rock geochemistry and the methane observations, rover-generated heating, rock crushing or soil disturbance are an unlikely cause for the high methane observation. However, this assumes that the wheels and APXS sample possible methane-laden rocks equally. The rover wheels may be more likely to crush weakly bound rocks such as carbonaceous ones, but the APXS samples may be less likely to sample them if sparsely distributed.

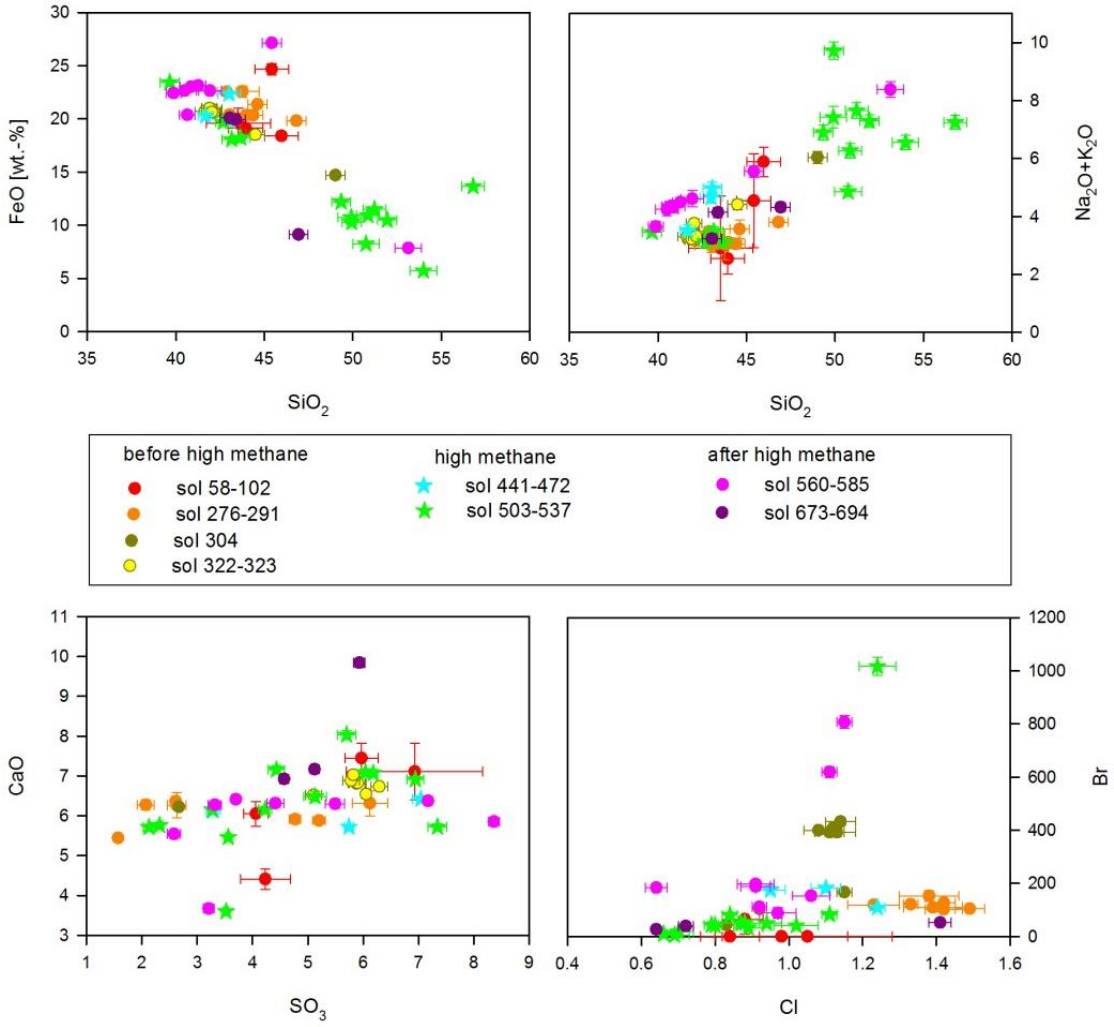

Fig. S13. Plots of APXS *(41)* chemical data. Dots represent APXS measurements taken in the timeframe of low-methane observations, stars represent APXS measurements taken in the same timeframe as the high-methane observations were made. The upper two panels represent oxides important for the host rock classification, e.g., Fe in olivine and alkali oxides in feldspars. The lower two panels represent elements important in secondary alteration e.g., for the formation of Ca-sulfates or evaporitic minerals.

TLS Raw Science and Housekeeping Data for Each Sol

In this section we present two-minute point-by-point raw data that includes relevant science and housekeeping data for both full and empty cells of each sol for which data was recorded. The table S2 below allows the reconstruction / traceability of the final data results and statistics given in the main body of the paper as Table 1.

For all the data given in Table S2 below, the TLS Herriott cell path length is 1680 cm. An average value of the 3 read temperatures (columns E, F, G) is used to process the data. For empty cell runs, the actual pressure in the Herriott cell is $<10^{-4}$ mbar. All quoted mixing ratios in ppbv have been first corrected by a calibration factor resulting from pre-launch calibrations with standard mixtures as described earlier in the SOM.

The columns given in Table S2 below are:

A = Index number for each 2-minute data point

B = Elapsed time (seconds)

C = Fore optics Pressure (mbar) as read. The true fore optics pressure (given in Table 1) is column C values minus 3 mbar.

D = Laser plate temp (deg C)

E = Fore optics temp (deg C)

F = Ref cell temp (deg C)

G = Science detector temp (deg C)

H = Herriott cell pressure (mbar). For full cells this is the actual Herriott cell pressure. For empty cells, this column will read the mean value of the full cell pressure since we convert the fore optics methane abundance signal to what it would be in the Herriott cell prior to subtracting it later in the final column.

I = CH4 mixing ratio (ppbv) from weighting the mixing ratio from 3 lines that takes into account that the g line is about twice as strong (SNR) as the e and f lines that have equal magnitude.

J = Weighted CH4 mixing ratio (ppbv) calculated as the difference of the value in column I minus the mean value for the empty cell for each particular run. Note for the empty cell values, the mean value of column J will therefore be zero, and the data scatter gives us the empty cell SEM value to add (RSS) with the data scatter of the full cell.

Table S2. TLS Raw Data for Full and Empty Cell runs for each sol.

Sol79 Full:									
A	B	C	D	E	F	G	H	I	J
1	16445	14.56	18.54	44.62	42.79	46.98	6.662	71.54362	-8.54402
2	16605	14.52	18.54	44.65	42.48	46.4	6.452	74.55205	-5.53559
3	16766	14.53	18.53	44.48	42.74	46.89	6.632	73.92872	-6.15892
4	16927	14.55	18.53	45.16	42.54	46.58	6.442	83.21665	3.129013
5	17088	14.55	18.54	44.33	42.68	46.78	6.612	74.10462	-5.98302
6	17249	14.53	18.55	45.23	42.66	46.82	6.442	78.1916	-1.89604
7	17409	14.54	18.56	44.2	42.62	46.67	6.572	87.57683	7.489191
8	17570	14.53	18.57	45.06	42.74	46.95	6.502	82.71834	2.630704
9	17731	14.54	18.58	44.07	42.55	46.56	6.522	71.70673	-8.38091
10	17891	14.56	18.58	44.9	42.77	47	6.582	75.84954	-4.2381
11	18052	14.56	18.58	43.95	42.49	46.45	6.482	66.4225	-13.6651
12	18213	14.55	18.58	44.75	42.76	47	6.622	72.4699	-7.61774

13	18374	14.51	18.57	43.87	42.43	46.32	6.452	55.79384	-24.2938
14	18534	14.54	18.52	44.61	42.73	46.94	6.622	80.7523	0.664663
15	18695	14.54	18.55	44.32	42.37	46.28	6.432	79.63755	-0.45009
16	18856	14.55	18.53	44.47	42.69	46.87	6.622	73.84749	-6.24015
17	19017	14.55	18.51	44.85	42.42	46.41	6.412	81.97289	1.885247
18	19178	14.53	18.48	44.34	42.65	46.79	6.592	69.13349	-10.9541
19	19338	14.53	18.45	45.23	42.54	46.66	6.412	78.99308	-1.09456
20	19499	14.53	18.41	44.23	42.59	46.73	6.562	88.48778	8.400142
21	19660	14.52	18.37	45.11	42.65	46.89	6.402	85.08292	4.995284
22	19820	14.53	18.33	44.08	42.52	46.57	6.512	99.85333	19.76569
23	19981	14.53	18.29	44.92	42.7	46.94	6.502	96.92697	16.83933
24	20142	14.53	18.25	43.95	42.45	46.45	6.462	95.41509	15.32745
25	20302	14.53	18.21	44.76	42.69	46.95	6.562	91.17831	11.09067
Sol79 Empty:									
A	B	C	D	E	F	G	H	I	J
1	13327	14.56	18.66	45.05	42.5	46.97	6.523	76.64755	-3.44009
2	13487	14.52	18.73	44.07	42.45	46.73	6.523	60.95483	-19.1328
3	13648	14.54	18.77	44.96	42.67	47.11	6.523	82.62281	2.535167
4	13809	14.56	18.79	44.02	42.49	46.64	6.523	73.51998	-6.56766
5	13969	14.57	18.8	44.88	42.77	47.15	6.523	63.65598	-16.4317
6	14131	14.56	18.81	43.96	42.5	46.55	6.523	96.19029	16.10265
7	14291	14.55	18.8	44.86	42.72	47.01	6.523	76.71578	-3.37186
8	14452	14.55	18.8	43.93	42.46	46.47	6.523	94.80176	14.71412
9	14613	14.55	18.78	44.78	42.77	47.05	6.523	80.5615	0.473861
10	14774	14.56	18.76	43.91	42.45	46.39	6.523	69.33734	-10.7503
11	21340	14.53	17.95	44.16	42.56	46.68	6.523	86.05545	5.967811
12	21646	14.52	17.86	44.08	42.49	46.6	6.523	81.6454	1.557759
13	21806	14.53	17.81	44.9	42.64	46.93	6.523	90.54097	10.45333
14	21967	14.52	17.76	43.92	42.4	46.46	6.523	79.73747	-0.35017
15	22128	14.51	17.71	45.14	42.75	47.16	6.523	85.11004	5.022396
16	22289	14.52	17.67	44.12	42.54	46.69	6.523	80.5477	0.460058
17	22449	14.51	17.64	44.91	42.72	47.08	6.523	82.62589	2.538247
18	22610	14.51	17.6	43.93	42.42	46.5	6.523	66.95215	-13.1355
19	22771	14.52	17.57	44.71	42.67	47.02	6.523	83.40107	3.313429
20	22932	14.52	17.54	43.78	42.3	46.33	6.523	83.22399	3.136354
21	23092	14.6	17.53	44.89	42.79	47.22	6.523	90.81838	10.73074
22	23253	14.51	17.49	43.91	42.42	46.52	6.523	76.26169	-3.82595
Sol81 Full:									
A	B	C	D	E	F	G	H	I	J
1	17544	14.76	21	45.25	43.11	46.88	6.602	67.01518	-16.8779
2	17705	14.75	20.91	44.35	42.95	46.54	6.612	90.95843	7.065365
3	17865	14.75	20.83	45.28	43.07	46.88	6.522	93.36267	9.469611
4	18026	14.76	20.75	44.37	42.95	46.59	6.632	99.33399	15.44093

5	18187	14.75	20.69	45.35	43.02	46.8	6.542	100.7288	16.83578
6	18347	14.74	20.62	44.41	42.95	46.63	6.642	89.5342	5.641139
7	18508	14.73	20.56	45.4	42.95	46.72	6.482	95.66268	11.76962
8	18669	14.73	20.51	44.44	42.94	46.67	6.642	83.8953	0.002236
9	18829	14.72	20.45	45.41	42.87	46.62	6.482	74.77954	-9.11352
10	18990	14.73	20.39	44.45	42.93	46.69	6.652	75.77327	-8.11979
11	19151	14.71	20.34	45.34	42.77	46.48	6.452	79.23326	-4.6598
12	19311	14.72	20.28	44.47	42.91	46.7	6.632	84.77684	0.883782
13	19472	14.7	20.22	45.42	42.98	46.87	6.532	78.09694	-5.79612
14	19633	14.73	20.17	44.44	42.94	46.73	6.642	73.44997	-10.4431
15	19793	14.69	20.12	45.4	42.88	46.72	6.472	90.88347	6.990406
16	19954	14.71	20.06	44.38	42.9	46.71	6.622	90.57041	6.67735
17	20115	14.73	20.02	45.35	42.78	46.55	6.442	95.28182	11.38876
18	20275	14.71	19.97	44.41	42.86	46.69	6.612	93.01972	9.126661
19	20582	14.69	19.89	44.44	42.89	46.74	6.622	102.7503	18.85724
20	20743	14.68	19.83	45.33	42.73	46.54	6.432	84.35604	0.462979
21	20903	14.69	19.77	44.42	42.85	46.71	6.602	87.79615	3.903088
22	21064	14.67	19.72	45.33	42.9	46.87	6.492	74.99412	-8.89894
23	21225	14.68	19.66	44.35	42.83	46.68	6.592	84.00213	0.109071
24	21385	14.66	19.61	45.3	42.78	46.69	6.432	75.1058	-8.78726
25	21546	14.69	19.56	44.31	42.77	46.63	6.572	67.78387	-16.1092
Sol81 Empty:									
A	B	C	D	E	F	G	H	I	J
1	12193	14.85	22.96	44.7	42.75	46.32	6.558	89.72983	5.836767
2	12353	14.87	23.04	44.76	43.17	46.99	6.558	68.68776	-15.2053
3	12514	14.87	23.07	44.05	42.87	46.33	6.558	82.68542	-1.20764
4	12675	14.86	23.07	45.07	43.18	46.93	6.558	84.03241	0.139354
5	12835	14.87	23.05	44.3	43.02	46.51	6.558	89.33652	5.443463
6	12996	14.87	23.03	45.38	43.14	46.78	6.558	82.58879	-1.30427
7	13157	14.86	22.99	44.53	43.14	46.68	6.558	71.29067	-12.6024
8	13318	14.86	22.95	45.14	42.92	46.32	6.558	79.57029	-4.32277
9	13479	14.87	22.9	44.74	43.24	46.83	6.558	69.3854	-14.5077
10	13639	14.85	22.84	44.18	42.89	46.15	6.558	80.11882	-3.77424
11	13800	14.87	22.78	44.94	43.3	46.92	6.558	79.32419	-4.56887
12	13961	14.86	22.71	44.18	43	46.3	6.558	79.64448	-4.24858
13	14121	14.88	22.64	45.15	43.3	46.93	6.558	94.45001	10.55695
14	14282	14.85	22.58	44.35	43.08	46.47	6.558	78.63773	-5.25533
15	14443	14.85	22.51	45.39	43.21	46.8	6.558	93.46878	9.57572
16	14603	14.85	22.45	44.51	43.15	46.61	6.558	83.54709	-0.34597
17	14764	14.83	22.38	45.51	43.24	46.84	6.558	93.15173	9.258674
18	14925	14.84	22.3	44.62	43.21	46.73	6.558	90.04398	6.150921
19	15085	14.83	22.22	45.13	42.95	46.32	6.558	91.82756	7.934504
20	15247	14.86	22.14	44.75	43.24	46.81	6.558	77.36701	-6.52605

21	15407	14.81	22.06	44.99	42.95	46.33	6.558	77.18287	-6.71019
22	15568	14.84	21.99	44.8	43.29	46.91	6.558	90.74457	6.851507
23	15874	14.8	21.83	45.07	43.29	46.96	6.558	82.10128	-1.79178
24	22572	14.65	19.33	44.64	42.55	46.33	6.558	88.63764	4.744581
25	22733	14.67	19.28	44.58	42.86	46.89	6.558	85.44725	1.55419
26	22894	14.65	19.23	45.05	42.61	46.48	6.558	96.94305	13.04999
27	23054	14.67	19.19	44.79	43	47.14	6.558	82.01316	-1.8799
28	23215	14.65	19.16	44.08	42.59	46.35	6.558	87.04733	3.154273
Sol106 Full:									
A	B	C	D	E	F	G	H	I	J
1	17558	14.06	16.58	44.92	42.23	46.52	6.932	89.78309	-2.50446
2	17719	14.07	16.56	44.16	42.34	46.77	7.072	79.02951	-13.258
3	17879	14.07	16.51	44.97	42.55	47.09	7.052	99.72478	7.43723
4	18041	14.06	16.49	43.91	42.3	46.58	7.002	88.95635	-3.3312
5	18201	14.05	16.48	44.72	42.51	47.02	7.052	87.42899	-4.85856
6	18362	14.08	16.46	44.08	42.18	46.4	6.972	101.8558	9.568269
7	18523	14.07	16.45	44.43	42.49	46.99	7.122	86.93041	-5.35714
8	18683	14.05	16.44	45.26	42.41	46.87	6.962	81.70218	-10.5854
9	18844	14.07	16.43	44.15	42.42	46.82	7.072	98.59034	6.302794
10	19005	14.06	16.42	45.01	42.46	46.95	6.962	85.22281	-7.06474
11	19165	14.06	16.42	43.94	42.29	46.6	7.002	90.30474	-1.98281
12	19326	14.08	16.41	44.7	42.56	47.17	7.132	98.63445	6.346905
13	19487	14.08	16.42	43.72	42.15	46.39	6.932	111.1797	18.89219
14	19647	14.13	16.41	44.47	42.49	46.98	7.092	97.42717	5.139618
15	19809	14.06	16.4	45	42.26	46.63	6.962	95.27248	2.984929
16	19969	14.07	16.4	44.2	42.41	46.85	7.082	96.76998	4.48243
17	20130	14.05	16.41	45.08	42.34	46.77	6.912	94.29407	2.006516
18	20291	14.05	16.41	43.97	42.28	46.63	6.992	102.6842	10.39661
19	20451	14.07	16.41	45.23	42.42	46.96	6.942	88.54785	-3.7397
20	20612	14.06	16.41	44.12	42.38	46.79	7.062	95.92603	3.638481
21	20773	14.06	16.41	44.87	42.57	47.16	7.092	86.97158	-5.31597
22	20933	14.06	16.41	43.84	42.26	46.54	6.972	98.79886	6.511306
23	21094	14.06	16.41	44.61	42.49	47.02	7.082	84.27955	-8.008
24	21255	14.06	16.41	44.4	42.16	46.43	6.942	101.9578	9.670247
25	21416	14.07	16.4	44.33	42.45	46.93	7.102	88.03032	-4.25723
26	21577	14.06	16.4	44.82	42.17	46.48	6.882	87.00388	-5.28367
Sol106 Empty:									
A	B	C	D	E	F	G	H	I	J
1	12512	14.07	16.52	43.62	42.01	46.52	7.015	73.72393	-18.5636
2	12673	14.07	16.6	44.77	42.46	47.31	7.015	88.29278	-3.99477
3	12833	14.07	16.65	43.77	42.17	46.64	7.015	90.05381	-2.23374
4	12994	14.08	16.69	44.61	42.45	47.15	7.015	98.52705	6.2395
5	13155	14.07	16.71	43.64	42.11	46.44	7.015	91.3843	-0.90325

6	13315	14.11	16.72	44.45	42.42	47.03	7.015	105.0055	12.71792
7	13476	14.09	16.73	44.03	42.05	46.3	7.015	88.88768	-3.39987
8	13637	14.08	16.73	44.29	42.38	46.91	7.015	85.33829	-6.94926
9	13798	14.07	16.73	44.56	42.07	46.35	7.015	90.9739	-1.31365
10	13959	14.08	16.73	44.15	42.33	46.78	7.015	97.11357	4.826016
11	14119	14.06	16.72	45.11	42.19	46.56	7.015	96.23221	3.94466
12	14280	14.08	16.72	44.01	42.28	46.65	7.015	93.53963	1.252085
13	14441	14.07	16.71	44.84	42.5	47.07	7.015	81.96601	-10.3215
14	14602	14.11	16.71	43.82	42.23	46.5	7.015	83.96638	-8.32117
15	14762	14.09	16.71	44.63	42.49	47.05	7.015	105.3195	13.03194
16	14923	14.08	16.71	43.65	42.13	46.32	7.015	86.05727	-6.23028
17	15084	14.09	16.71	44.46	42.44	46.93	7.015	100.2554	7.96783
18	15245	14.07	16.7	44.9	42.22	46.55	7.015	100.8997	8.612148
19	15405	14.1	16.7	44.24	42.44	46.86	7.015	92.69327	0.405721
20	15566	14.06	16.69	45.14	42.34	46.74	7.015	100.395	8.107438
21	15727	14.1	16.68	44.04	42.34	46.68	7.015	89.48796	-2.79959
22	15887	14.07	16.67	44.94	42.41	46.87	7.015	93.35371	1.066156
23	16048	14.08	16.65	43.87	42.24	46.51	7.015	112.0794	19.79183
24	22476	14.06	16.42	44.79	42.16	46.46	7.015	81.66766	-10.6199
25	22637	14.1	16.4	44.1	42.32	46.73	7.015	89.55833	-2.72922
26	22797	14.1	16.39	44.9	42.48	47.01	7.015	87.02799	-5.25956
27	22958	14.07	16.36	43.83	42.22	46.53	7.015	98.64219	6.35464
28	23119	14.08	16.34	44.56	42.51	47.07	7.015	82.82373	-9.46382
29	23279	14.07	16.31	43.88	42.09	46.3	7.015	91.073	-1.21455
Sol292 Full:									
A	B	C	D	E	F	G	H	I	J
1	17416	12.46	17.15	44.83	42.67	47.11	7.292	96.76794	-13.1652
2	17577	12.44	17.15	44.18	42.35	46.48	7.122	101.7995	-8.13364
3	17738	12.44	17.19	44.53	42.63	47.05	7.342	88.46887	-21.4643
4	17898	12.46	17.18	44.58	42.29	46.42	7.112	111.4216	1.488405
5	18059	12.45	17.17	44.3	42.53	46.84	7.292	107.8867	-2.04645
6	18220	12.44	17.14	45.11	42.59	46.99	7.182	107.393	-2.54019
7	18380	12.45	17.1	44.04	42.44	46.65	7.212	99.99757	-9.93558
8	18541	12.5	17.04	44.84	42.59	46.96	7.202	119.321	9.3878
9	18702	12.43	16.98	43.83	42.29	46.42	7.152	111.2752	1.342021
10	18862	12.44	16.92	44.53	42.58	46.97	7.312	117.5766	7.643471
11	19023	12.44	16.85	45	42.36	46.6	7.142	103.6145	-6.31865
12	19184	12.43	16.8	44.23	42.5	46.81	7.262	118.9729	9.039723
13	19344	12.43	16.76	45	42.63	47.08	7.222	113.713	3.779828
14	19505	12.41	16.72	43.95	42.37	46.58	7.182	117.581	7.647871
15	19666	12.43	16.7	45.11	42.68	47.2	7.272	112.8337	2.900532
16	19826	12.44	16.68	43.98	42.44	46.7	7.232	118.1863	8.253178
17	19987	12.42	16.66	44.82	42.59	47.03	7.222	104.3821	-5.55102

18	20148	12.41	16.64	43.89	42.27	46.53	7.152	112.086	2.152864
19	20308	12.45	16.63	44.85	42.72	47.29	7.392	120.2703	10.33719
20	20469	12.43	16.62	43.85	42.34	46.52	7.152	131.5083	21.57513
21	20630	12.43	16.6	44.51	42.59	47.03	7.302	112.0479	2.114744
22	20790	12.43	16.59	44.03	42.17	46.27	7.092	105.9282	-4.00495
23	20951	12.43	16.59	44.71	42.65	47.19	7.362	105.2734	-4.65976
24	21111	12.43	16.59	43.92	42.25	46.4	7.152	115.7771	5.843952
25	21272	12.43	16.58	44.79	42.7	47.26	7.372	108.3582	-1.57492
Sol292 Empty:									
A	B	C	D	E	F	G	H	I	J
1	12372	12.41	17.13	44.57	42.49	47.25	7.229	110.2908	0.357647
2	12533	12.41	17.2	43.86	42.13	46.47	7.229	107.7875	-2.14566
3	12693	12.45	17.25	44.4	42.47	47.05	7.229	97.62357	-12.3096
4	12854	12.44	17.28	44.36	42.13	46.39	7.229	110.2016	0.268405
5	13014	12.42	17.3	44.57	42.61	47.19	7.229	100.8571	-9.07601
6	13176	12.44	17.32	44.25	42.23	46.44	7.229	113.2934	3.360294
7	13336	12.46	17.34	44.38	42.54	46.98	7.229	97.56478	-12.3684
8	13497	12.47	17.3	44.73	42.25	46.47	7.229	114.7462	4.813009
9	13658	12.46	17.36	44.21	42.46	46.8	7.229	104.6422	-5.29093
10	13818	12.46	17.42	45.04	42.6	47.06	7.229	105.3439	-4.58926
11	13979	12.47	17.35	44	42.42	46.64	7.229	114.5773	4.644116
12	14140	12.47	17.32	45.17	42.7	47.21	7.229	109.9898	0.056694
13	14300	12.47	17.29	44.13	42.52	46.77	7.229	116.1044	6.171202
14	14461	12.45	17.25	44.94	42.66	47.09	7.229	105.533	-4.40012
15	14622	12.5	17.2	43.93	42.39	46.55	7.229	118.465	8.531816
16	14782	12.46	17.14	45.08	42.73	47.24	7.229	110.2832	0.350048
17	14943	12.47	17.09	44.05	42.48	46.69	7.229	111.9352	2.002023
18	15103	12.46	17.04	44.83	42.66	47.07	7.229	112.2417	2.308552
19	15264	12.46	17	44.11	42.34	46.46	7.229	100.3607	-9.57247
20	15425	12.47	16.97	44.55	42.64	47.04	7.229	110.604	0.670833
21	15586	12.46	16.96	44.52	42.28	46.4	7.229	123.3894	13.45628
22	15746	12.48	16.94	44.32	42.53	46.86	7.229	107.5007	-2.43243
23	22175	12.45	16.64	45.01	42.73	47.33	7.229	108.0585	-1.87467
24	22335	12.45	16.63	43.97	42.42	46.67	7.229	114.2711	4.337924
25	22496	12.44	16.64	44.7	42.61	47.08	7.229	111.0682	1.13502
26	22657	12.43	16.66	44.35	42.26	46.46	7.229	112.1906	2.257421
27	22817	12.44	16.68	44.39	42.54	46.94	7.229	119.9849	10.05178
28	22978	12.44	16.7	45.18	42.51	46.95	7.229	109.2195	-0.7137
Sol306 Full:									
A	B	C	D	E	F	G	H	I	J
1	3045	2.83	14.32	44.01	42.11	48.23	6.522	3.815164	0.882994
2	3206	2.84	14.4	44.96	42.36	48.42	6.462	7.34974	4.41757
3	3367	2.87	14.44	43.47	42.06	47.59	6.412	20.85264	17.92047

4	3527	2.87	14.48	44.5	42.47	48.22	6.602	16.35376	13.42159
5	3688	2.89	14.52	44.67	42.15	47.5	6.342	-3.06665	-5.99882
6	3848	2.89	14.55	44.08	42.43	47.84	6.612	-2.54729	-5.47946
7	4009	2.89	14.58	45.21	42.55	48.01	6.482	7.940311	5.008141
8	4170	2.93	14.61	43.72	42.33	47.44	6.512	3.422185	0.490015
9	4330	2.93	14.64	44.69	42.68	48.05	6.682	11.13514	8.202975
10	4491	2.95	14.67	44.64	42.31	47.3	6.452	4.758878	1.826708
11	4652	2.96	14.7	44.28	42.62	47.78	6.692	9.257345	6.325175
12	4812	2.95	14.73	45.37	42.67	47.86	6.542	14.87495	11.94278
13	4973	2.98	14.75	43.91	42.5	47.42	6.592	15.71087	12.7787
14	5134	2.97	14.79	44.88	42.82	48.01	6.732	15.59188	12.65971
15	5294	2.99	14.82	44.62	42.43	47.26	6.552	12.66532	9.733147
16	5455	2.98	14.87	44.47	42.77	47.82	6.772	5.882562	2.950392
17	5615	3	14.99	45.49	42.75	47.8	6.592	5.412557	2.480387
18	5776	3.03	15.02	44.08	42.64	47.48	6.672	13.24316	10.31099
19	5937	3.02	15.09	44.56	42.75	47.7	6.692	8.598874	5.666704
20	6097	3.02	15.13	45.07	42.48	47.27	6.382	12.00407	9.071903
21	6258	3.03	15.16	44.26	42.69	47.55	6.722	1.61431	-1.31786
22	6419	3.02	15.19	45.29	42.87	47.9	6.682	-4.38101	-7.31318
23	6579	3.04	15.2	43.91	42.51	47.26	6.622	12.60968	9.677507
24	6740	3.04	15.24	45.03	42.85	47.83	6.702	15.98493	13.05276
Sol306 Empty:									
A	B	C	D	E	F	G	H	I	J
1	9101	3.04	15.91	44.96	42.69	47.28	6.584	10.29446	7.362286
2	9261	3.06	15.89	43.77	42.45	46.76	6.584	1.363006	-1.56916
3	9422	3.06	15.86	44.46	42.67	47.21	6.584	-2.92177	-5.85394
4	9583	3.06	15.83	44.39	42.29	46.55	6.584	17.63237	14.7002
5	9743	3.06	15.8	44.44	42.73	47.33	6.584	-4.9655	-7.89767
6	9904	3.05	15.76	45.03	42.49	46.9	6.584	5.60066	2.66849
7	10065	3.06	15.72	43.94	42.52	46.93	6.584	8.789412	5.857242
8	10225	3.05	15.68	44.58	42.73	47.35	6.584	0.318399	-2.61377
9	10386	3.04	15.65	45.18	42.56	47.07	6.584	8.240147	5.307977
10	10546	3.05	15.61	44.03	42.58	47.14	6.584	-11.2075	-14.1397
11	10707	3.08	15.59	45.19	42.77	47.5	6.584	9.844905	6.912735
12	10868	3.04	15.58	43.92	42.55	47.01	6.584	1.912447	-1.01972
13	11028	3.04	15.57	45.03	42.86	47.64	6.584	8.372391	5.440221
14	11189	3.05	15.58	43.79	42.5	46.92	6.584	4.560537	1.628367
15	11350	3.04	15.6	44.42	42.69	47.33	6.584	-6.72762	-9.65979
16	11510	3.03	15.62	45.39	42.62	47.24	6.584	4.352027	1.419857
17	11671	3.04	15.64	44.21	42.7	47.31	6.584	-5.61156	-8.54373
Sol313 Full:									
A	B	C	D	E	F	G	H	I	J
1	17557	3.18	16.94	44.58	43.03	46.86	7.352	3.346288	2.001868

2	17718	3.18	16.98	45.38	42.97	46.79	7.212	8.582943	7.238523
3	17879	3.21	17.03	44.32	42.95	46.69	7.382	1.73746	0.39304
4	18039	3.19	17.09	45.12	43.01	46.83	7.212	5.93089	4.58647
5	18200	3.2	17.12	44.1	42.82	46.46	7.222	7.039234	5.694814
6	18361	3.19	17.14	44.81	43.08	46.96	7.352	-6.24634	-7.59076
7	18521	3.19	17.15	43.95	42.7	46.23	7.172	-3.51292	-4.85734
8	18682	3.19	17.16	44.62	43	46.76	7.322	1.170393	-0.17403
9	18843	3.19	17.16	45.27	42.83	46.54	7.172	-12.3959	-13.7403
10	19004	3.2	17.16	44.36	42.96	46.7	7.302	4.001516	2.657096
11	19164	3.19	17.14	45.23	42.92	46.7	7.152	-11.4434	-12.7879
12	19325	3.21	17.11	44.17	42.85	46.52	7.242	0.800171	-0.54425
13	19486	3.19	17.08	44.93	43.09	46.98	7.322	-8.56252	-9.90694
14	19647	3.2	17.04	43.95	42.75	46.32	7.172	17.14424	15.79982
15	19807	3.18	17	44.71	43.02	46.88	7.312	3.947851	2.603431
16	19968	3.19	16.96	44.93	42.76	46.41	7.172	-1.1526	-2.49702
17	20129	3.21	16.92	44.46	42.99	46.78	7.332	8.995767	7.651347
18	20289	3.19	16.89	45.25	43.1	46.99	7.242	13.58355	12.23913
19	20450	3.22	16.84	44.21	42.97	46.6	7.252	20.54244	19.19802
20	20611	3.18	16.83	45.01	43.07	46.95	7.262	8.387115	7.042695
21	20772	3.19	16.79	44.13	42.78	46.41	7.272	3.513235	2.168815
22	20932	3.19	16.76	44.73	43.09	47	7.452	1.953025	0.608605
23	21094	3.19	16.73	44.5	42.7	46.28	7.142	6.360597	5.016177
24	21254	3.19	16.69	44.51	42.99	46.8	7.312	10.01802	8.673602
25	21415	3.19	16.65	44.95	42.7	46.34	7.102	4.986781	3.642361
26	21576	3.19	16.61	44.33	42.87	46.61	7.252	1.734795	0.390375
Sol313 Empty:									
A	B	C	D	E	F	G	H	I	J
1	12832	3.18	16.51	44.87	42.6	46.52	7.257	-0.7421	-2.08652
2	12993	3.19	16.6	44.32	42.82	46.84	7.257	3.720919	2.376499
3	13154	3.18	16.69	45.12	42.97	47.07	7.257	19.48798	18.14356
4	13314	3.2	16.8	44.11	42.78	46.64	7.257	3.442056	2.097636
5	13475	3.19	16.9	44.91	42.98	47.01	7.257	-4.62418	-5.9686
6	13636	3.21	16.98	44.13	42.69	46.42	7.257	21.11955	19.77513
7	13796	3.2	17.05	44.66	43.03	47	7.257	-0.01354	-1.35796
8	13957	3.19	17.09	44.57	42.67	46.34	7.257	-3.32243	-4.66685
9	14118	3.23	17.12	44.47	42.99	46.83	7.257	4.761399	3.416979
10	14279	3.21	17.14	45.05	42.72	46.42	7.257	-0.48184	-1.82626
11	14440	3.21	17.15	44.31	42.88	46.67	7.257	-1.26126	-2.60568
12	14600	3.2	17.17	45.13	43.06	47	7.257	-7.39677	-8.74119
13	14761	3.21	17.17	44.14	42.84	46.45	7.257	0.199528	-1.14489
14	14922	3.2	17.16	44.93	43.07	46.97	7.257	-0.08164	-1.42606
15	15082	3.21	17.15	44.35	42.76	46.38	7.257	0.192271	-1.15215
16	15243	3.21	17.14	44.69	43.1	46.98	7.257	-1.07048	-2.4149

17	15404	3.22	17.11	44.83	42.77	46.39	7.257	-6.85488	-8.1993
18	15565	3.18	17.09	44.51	43.04	46.83	7.257	-15.0198	-16.3642
19	15726	3.2	17.06	45.24	42.84	46.54	7.257	1.0685	-0.27592
20	15886	3.2	17.01	44.35	42.95	46.69	7.257	1.668028	0.323608
21	16047	3.19	17	45.14	43.14	47.06	7.257	-1.05834	-2.40276
22	17557	3.18	16.94	44.58	43.03	46.86	7.257	4.550112	3.205692
23	22469	3.2	16.5	44.03	42.76	46.43	7.257	6.146927	4.802507
24	22630	3.19	16.45	44.82	42.95	46.85	7.257	1.81682	0.4724
25	22791	3.19	16.41	44.17	42.62	46.25	7.257	5.711335	4.366915
26	22952	3.19	16.37	44.55	42.94	46.84	7.257	1.134143	-0.21028
27	23112	3.17	16.34	45.35	42.84	46.7	7.257	5.258879	3.914459
28	23273	3.19	16.31	44.31	42.87	46.62	7.257	-0.70735	-2.05177
Sol466 Full:									
A	B	C	D	E	F	G	H	I	J
1	15709	5.311	16.0123	43.92057	42.61845	46.42974	7.6587	28.30752	7.934239
2	16019	5.3141	16.09998	44.0702	42.50471	46.24944	7.6277	28.44428	8.070997
3	16179	5.3172	16.11435	44.82478	42.96845	47.11537	7.854	17.76879	-2.60449
4	16343	5.3203	16.12872	43.99538	42.56896	46.33775	7.6401	33.35084	12.97756
5	16508	5.3172	16.13447	44.54899	42.85192	46.89182	7.7734	28.26643	7.893146
6	16672	5.3048	16.13447	45.35021	42.75901	46.75991	7.6277	35.82834	15.45506
7	16837	5.3141	16.12297	44.26077	42.77558	46.70653	7.7176	37.62974	17.25646
8	17001	5.2955	16.10142	45.05384	42.84362	46.89003	7.6556	23.93667	3.563393
9	17166	5.3079	16.07555	44.00218	42.62175	46.45275	7.6494	32.98423	12.61095
10	17330	5.3079	16.04105	45.18012	42.94178	47.10104	7.7455	22.56205	2.188769
11	17495	5.3265	15.99792	44.11782	42.70934	46.59104	7.6959	31.59868	11.2254
12	17805	5.3141	15.94616	44.27099	42.81539	46.75279	7.7331	45.04141	24.66813
13	17969	5.2924	15.91164	45.43375	42.98347	47.12613	7.6928	19.93991	-0.43337
14	18129	5.311	15.8915	44.35787	42.87353	46.84722	7.7455	29.32337	8.95009
15	18293	5.2986	15.87567	45.28245	42.67792	46.59281	7.5564	29.57614	9.202861
16	18458	5.3079	15.87711	44.47727	42.88517	46.91502	7.7734	13.43971	-6.93357
17	18622	5.2831	15.88287	45.35717	42.72423	46.67986	7.575	26.5934	6.220125
18	18787	5.2986	15.89725	44.53362	42.93178	46.9847	7.7889	11.44899	-8.92429
19	18951	5.2986	15.91308	45.36761	42.75735	46.71898	7.5936	22.77721	2.403928
20	19116	5.3203	15.95191	44.54387	42.95011	47.00258	7.7982	26.12028	5.747001
21	19280	5.2955	16.07268	45.26856	42.7557	46.70653	7.5843	22.92588	2.552596
22	19584	5.3017	16.15745	45.28939	42.66635	46.59637	7.5378	18.46465	-1.90863
23	19749	5.3048	16.22496	44.47897	42.88517	46.91324	7.7517	33.41192	13.03864
24	19913	5.2955	16.27378	45.38327	42.74576	46.69942	7.575	9.675543	-10.6977
25	20078	5.3141	16.30967	44.53703	42.94344	46.99364	7.8013	16.98204	-3.39124
Sol466 Empty:									
A	B	C	D	E	F	G	H	I	J
1	10603	5.2707	15.51416	44.03619	42.4126	46.72788	7.686	22.94446	2.57118
2	10767	5.2769	15.6093	44.88322	42.60195	47.01331	7.686	26.03333	5.660045

3	10927	5.2707	15.66837	43.85429	42.41096	46.54313	7.686	23.42095	3.047668
4	11091	5.2769	15.70582	44.68585	42.64982	46.97219	7.686	15.64116	-4.73212
5	11250	5.3172	15.71878	44.0617	42.35676	46.35543	7.686	11.09059	-9.28269
6	11410	5.2924	15.72166	44.47556	42.71099	46.96682	7.686	13.48295	-6.89033
7	11574	5.2986	15.71734	44.61396	42.38632	46.3519	7.686	29.55567	9.182386
8	11739	5.2831	15.70726	44.26588	42.65148	46.77594	7.686	24.02075	3.647475
9	11903	5.2862	15.69286	45.14029	42.536	46.59992	7.686	15.10421	-5.26907
10	12068	5.3017	15.67846	44.05319	42.55413	46.5662	7.686	13.42484	-6.94844
11	12232	5.28	15.66261	44.8368	42.80212	47.02762	7.686	23.63699	3.263714
12	12397	5.3048	15.64676	43.82031	42.47673	46.35366	7.686	18.59094	-1.78234
13	12561	5.2986	15.6338	44.58831	42.76067	46.92038	7.686	32.88347	12.51019
14	12725	5.3017	15.61506	44.13313	42.36661	46.17711	7.686	20.20541	-0.16787
15	12890	5.2893	15.59777	44.37151	42.68949	46.77238	7.686	18.86326	-1.51002
16	13054	5.2831	15.58048	45.21998	42.70603	46.83296	7.686	17.0419	-3.33138
17	13219	5.2955	15.57471	44.11102	42.63331	46.61057	7.686	20.94208	0.568802
18	13383	5.2893	15.56318	44.91074	42.76895	46.91145	7.686	24.25814	3.884864
19	13543	5.2986	15.55165	43.90358	42.51459	46.40142	7.686	25.37435	5.001068
20	13707	5.2924	15.53435	44.6208	42.82867	47.06342	7.686	25.03901	4.66573
21	13866	5.2893	15.52569	44.23013	42.4389	46.2565	7.686	14.53637	-5.83691
22	14030	5.3017	15.51704	44.43972	42.75073	46.84009	7.686	33.22836	12.85508
23	21158	5.3017	16.36994	43.87468	42.61515	46.44036	7.686	3.038	-17.3353
24	21322	5.2862	16.32976	45.00896	42.97012	47.17994	7.686	28.96963	8.59635
25	21486	5.2955	16.25368	43.99708	42.72423	46.47046	7.686	8.339099	-12.0342
26	21651	5.2986	16.20342	44.70812	42.94011	46.9847	7.686	20.46948	0.096204
27	21815	5.2955	16.1632	44.23694	42.53435	46.24944	7.686	19.94311	-0.43017
Sol474 Full:									
A	B	C	D	E	F	G	H	I	J
1	15524	5.2831	16.05543	45.20611	42.80709	46.79197	7.5471	19.90683	-0.1882
2	15688	5.2831	16.02668	44.12633	42.70272	46.5591	7.6029	34.93569	14.84066
3	15852	5.2831	16.01086	45.35021	42.90514	47.0151	7.5998	19.53168	-0.56335
4	16012	5.28	15.97204	44.28802	42.80709	46.74211	7.6618	42.00423	21.9092
5	16322	5.2831	15.99074	44.08721	42.69776	46.63188	7.5936	43.31711	23.22208
6	16486	5.2676	15.96773	45.30329	42.91845	47.02941	7.5998	30.05844	9.963411
7	16651	5.2955	15.94328	44.22332	42.77061	46.68697	7.6308	25.3376	5.242573
8	16815	5.2893	15.92171	44.94173	42.88351	46.94002	7.5998	12.11733	-7.9777
9	16979	5.2831	15.89869	43.92737	42.5871	46.38019	7.5347	31.74783	11.6528
10	17144	5.28	15.87423	45.09531	42.95845	47.12254	7.6649	29.14913	9.054103
11	17308	5.2986	15.85409	44.0583	42.67792	46.53427	7.5812	33.21957	13.12454
12	17472	5.2924	15.83395	45.14375	43.02522	47.20866	7.6866	30.9649	10.86987
13	17632	5.2955	15.81812	44.13483	42.74079	46.6301	7.5936	25.74058	5.645545
14	17796	5.2955	15.80804	44.84024	42.92179	47.00795	7.6432	19.2979	-0.79713
15	17955	5.2986	15.79509	43.87638	42.56896	46.34306	7.5037	25.61572	5.520693
16	18119	5.2893	15.78501	44.98309	42.97679	47.15482	7.6959	28.07835	7.983324

17	18284	5.2955	15.78069	43.96988	42.63496	46.46161	7.5409	23.08255	2.987517
18	18448	5.2924	15.78213	44.65332	42.86356	46.92931	7.6525	24.43321	4.338177
19	18612	5.2862	15.78789	44.0753	42.44712	46.17887	7.482	17.52055	-2.57448
20	18771	5.2707	15.78789	44.81276	42.93511	47.09208	7.7114	28.79869	8.703662
21	18936	5.2986	15.74182	44.03109	42.54259	46.32185	7.5316	31.72407	11.62904
22	19100	5.2986	15.8138	44.85055	42.9818	47.14585	7.73	17.11821	-2.97682
23	19264	5.2893	15.85121	44.03789	42.5838	46.36427	7.5347	19.2237	-0.87133
24	19429	5.2986	15.90301	44.88838	43.01686	47.18891	7.73	27.71287	7.617844
25	19593	5.3017	15.95191	44.04129	42.61515	46.40142	7.5409	32.28536	12.19033
26	19758	5.2924	15.95479	44.92624	43.0503	47.22123	7.7331	28.47158	8.376552
Sol474 Empty:									
A	B	C	D	E	F	G	H	I	J
1	10609	5.3017	15.35688	45.04693	42.597	47.09387	7.613	20.31876	0.223733
2	10773	5.3172	15.47666	43.95797	42.46357	46.6923	7.613	18.31722	-1.77781
3	10938	5.3048	15.58624	45.16453	42.72423	47.15661	7.613	14.84457	-5.25046
4	11097	5.3978	15.68278	44.10762	42.6036	46.78841	7.613	9.50554	-10.5895
5	11261	5.2955	15.78357	45.28071	42.80046	47.15482	7.613	21.3261	1.231072
6	11420	5.3079	15.86848	44.21311	42.70603	46.85079	7.613	17.04259	-3.05244
7	11585	5.2769	15.94328	44.95896	42.78387	46.99543	7.613	26.70237	6.607344
8	11744	5.2955	15.99074	43.94437	42.55907	46.5254	7.613	38.97767	18.88264
9	11908	5.2862	16.0468	44.97792	42.96678	47.26616	7.613	14.53356	-5.56147
10	12218	5.2769	16.18044	45.30676	42.82701	46.9847	7.613	14.47054	-5.62449
11	12378	5.2831	16.22783	44.23864	42.75404	46.7617	7.613	37.49272	17.39769
12	12542	5.2645	16.26517	45.41808	42.87353	47.01868	7.613	20.51183	0.416803
13	12707	5.2831	16.27378	44.30846	42.82369	46.82048	7.613	19.26225	-0.83278
14	12871	5.2893	16.2824	45.05211	42.87353	46.94181	7.613	18.25512	-1.83991
15	13035	5.3079	16.28096	44.00898	42.64817	46.48641	7.613	23.35	3.254969
16	13199	5.2893	16.27809	45.20264	42.94844	47.11	7.613	18.29715	-1.79788
17	13364	5.2955	16.27235	44.14504	42.74245	46.6301	7.613	12.41914	-7.67589
18	13528	5.2924	16.26804	45.26508	43.03358	47.19968	7.613	8.79226	-11.3028
19	13693	5.2955	16.25942	44.2097	42.80875	46.7012	7.613	17.26117	-2.83386
20	13852	5.2676	16.23645	45.45292	42.82037	46.83296	7.613	6.404321	-13.6907
21	14016	5.2831	16.21491	44.38344	42.86688	46.83117	7.613	20.44452	0.349489
22	20837	5.3141	16.53773	44.52678	42.95011	46.96325	7.613	26.0597	5.964671
23	21001	5.3699	16.57212	44.52849	42.55578	46.24414	7.613	24.69647	4.601438
24	21166	5.3079	16.57212	44.67557	42.96845	47.02404	7.613	32.26013	12.1651
25	21330	5.2955	16.56926	44.62251	42.6069	46.35897	7.613	20.98654	0.891509
26	21495	5.3141	16.55493	44.75955	43.04027	47.11896	7.613	19.93859	-0.15644
Sol504 Full:									
A	B	C	D	E	F	G	H	I	J
1	14074	5.4133	16.27091	44.50117	42.88018	46.84365	7.6897	25.58666	2.902566
2	14239	5.4102	16.20055	44.92107	42.5937	46.36958	7.4913	11.46481	-11.2193
3	14403	5.3172	16.14309	44.61054	42.93344	46.97934	7.7455	29.26331	6.579217

4	14568	5.3854	16.09998	44.97964	42.66139	46.46515	7.5037	25.15922	2.475131
5	14732	5.3854	16.07268	44.33402	42.82037	46.72788	7.6432	30.76541	8.081324
6	14897	5.3792	16.0813	45.4355	42.75901	46.69764	7.5037	31.47654	8.79245
7	15056	5.3668	16.10573	44.47385	42.90181	46.88825	7.6928	26.68292	3.998829
8	15220	5.3823	16.1474	45.43201	42.7905	46.72432	7.5161	16.97346	-5.71063
9	15380	5.3761	16.17613	44.54558	42.96512	46.96682	7.7052	30.40926	7.725167
10	15544	5.3761	16.18618	45.37631	42.79382	46.6923	7.513	28.18483	5.50074
11	15709	5.3916	16.18618	44.57805	43.0035	47.00437	7.7176	37.89604	15.21195
12	15873	5.3792	16.18331	45.35717	42.81871	46.71898	7.5161	30.62005	7.935963
13	16032	5.3823	16.17469	44.34254	42.86854	46.76704	7.6246	41.00506	18.32097
14	16192	5.2366	16.16176	45.21824	42.82867	46.81335	7.5068	40.50287	17.81878
15	16356	5.3761	16.14452	44.13824	42.73913	46.56087	7.5781	34.50312	11.81903
16	16521	5.3761	16.12441	45.30329	42.95678	47.04194	7.5874	31.17277	8.48868
17	16680	5.3916	16.11004	44.25907	42.81871	46.70297	7.6184	21.3753	-1.30879
18	16844	5.373	16.08417	45.03485	42.92345	46.94538	7.5657	29.5489	6.864814
19	17004	5.3792	16.05687	44.02769	42.67957	46.46869	7.5347	29.85367	7.169578
20	17168	5.3761	16.02668	45.19224	42.99682	47.12075	7.6308	30.01755	7.333462
21	17333	5.3792	15.98498	44.13654	42.75238	46.59814	7.575	42.36706	19.68297
22	17643	5.3792	15.97204	43.99198	42.6102	46.43682	7.5192	34.84183	12.15774
23	17807	5.3761	15.9102	45.10223	43.0035	47.14226	7.6959	24.32199	1.637901
24	17971	5.3761	15.88718	44.0719	42.71761	46.53959	7.5502	25.28739	2.603301
25	18136	5.3885	15.86848	44.81447	42.92845	46.98649	7.637	30.61271	7.928617
Sol504 Empty:									
A	B	C	D	E	F	G	H	I	J
1	10613	5.3482	15.63668	43.65055	42.3026	46.41558	7.594	31.63759	8.953496
2	10777	5.3544	15.71014	44.41925	42.60525	46.93288	7.594	21.31742	-1.36667
3	10942	5.3482	15.7303	44.94173	42.42082	46.55732	7.594	21.14177	-1.54232
4	11101	5.3265	15.7663	44.21311	42.6201	46.81335	7.594	6.24349	-16.4406
5	11265	5.3482	15.77925	45.34152	42.5904	46.76704	7.594	26.91865	4.234558
6	11425	5.3544	15.77925	44.34765	42.75073	46.93109	7.594	23.70877	1.024675
7	11589	5.3451	15.78789	45.20958	42.64157	46.74211	7.594	28.16617	5.482076
8	11748	5.3761	15.80084	44.15355	42.65974	46.6923	7.594	26.14193	3.457836
9	11913	5.3606	15.85265	45.01068	42.7292	46.85614	7.594	21.2061	-1.47799
10	12072	5.3761	15.92027	43.98178	42.56896	46.50058	7.594	7.214975	-15.4691
11	12231	5.3575	15.99649	44.75098	42.85358	47.02404	7.594	26.96003	4.275938
12	12395	5.3978	16.08561	43.86618	42.48825	46.28475	7.594	27.56261	4.878516
13	19039	5.3854	15.85265	45.3085	42.93844	47.05268	7.594	27.20582	4.521725
14	19204	5.3637	15.81812	44.22502	42.78221	46.69942	7.594	20.70492	-1.97917
15	19368	5.3823	15.77637	44.96758	42.90014	47.02226	7.594	28.64022	5.956133
16	19533	5.404	15.74182	43.95797	42.61845	46.4262	7.594	22.29739	-0.3867
17	19698	5.3854	15.71446	45.10569	42.97679	47.14406	7.594	30.07966	7.395573
18	19862	5.3823	15.68566	44.0702	42.69941	46.5662	7.594	17.68464	-4.99945
19	20026	5.3637	15.65397	45.30502	42.86522	46.98291	7.594	28.00447	5.320382

20	20185	5.3978	15.61939	44.24034	42.76398	46.71898	7.594	13.60451	-9.07958
21	20350	5.3761	15.6093	45.40067	42.87187	47.04552	7.594	17.45912	-5.22497
22	20509	5.3916	15.57183	44.32209	42.82203	46.81691	7.594	19.56566	-3.11843
23	20673	5.3792	15.54011	45.15933	42.60525	46.49172	7.594	19.8017	-2.88239
24	20838	5.3947	15.53146	44.47727	42.85691	46.92395	7.594	30.37542	7.691333
25	21002	5.4691	15.50551	45.23212	42.68949	46.62833	7.594	23.90435	1.220265
26	21161	5.3017	15.47954	44.23694	42.69776	46.69586	7.594	21.56018	-1.12391
27	21321	5.3761	15.44925	45.42156	42.70438	46.75635	7.594	21.93089	-0.7532
28	21480	5.3823	15.42039	44.4022	42.82037	46.87754	7.594	24.11609	1.432003
Sol526 Full:									
A	B	C	D	E	F	G	H	I	J
1	2388	4.877	13.60426	43.79652	40.31692	47.95639	6.552	26.70648	4.022131
2	2552	4.8987	13.71572	44.0821	40.71419	47.83603	6.5737	31.73884	9.054487
3	2717	4.9142	13.80363	43.01352	41.11718	47.85607	6.6915	40.73792	18.05357
4	2881	4.9421	13.8622	44.01918	41.65141	48.37854	6.8124	37.63639	14.95204
5	3045	4.97	13.90757	44.85227	41.69388	48.08626	6.676	24.19203	1.507681
6	3209	5.0134	13.94268	43.47609	41.7674	47.82511	6.831	29.92991	7.245559
7	3373	5.0351	13.9734	44.28121	42.20096	48.36195	7.0325	40.66542	17.98107
8	3538	5.0723	14.00411	44.70298	41.9309	47.67427	6.7132	20.38637	-2.29798
9	3702	5.1095	14.03188	43.81181	42.13217	47.83057	6.9178	22.39282	-0.29153
10	4012	5.1281	14.08888	43.5404	42.06342	47.44088	6.8372	31.97966	9.295311
11	4176	5.1591	14.10641	44.52849	42.44219	48.06245	7.0046	33.76789	11.08354
12	4340	5.1591	14.11517	44.75441	42.14527	47.41021	6.8093	31.81215	9.1278
13	4668	5.1963	14.14147	45.10396	42.55083	48.0167	6.9333	38.73551	16.05116
14	4832	5.2335	14.15023	43.75577	42.2239	47.28414	6.9209	45.68799	23.00364
15	4997	5.249	14.15899	44.56779	42.6003	47.96187	7.0883	35.85912	13.17477
16	5161	5.1343	14.15899	45.1005	42.36661	47.47879	6.8744	33.15296	10.46861
17	5325	5.2862	14.16045	44.11102	42.48331	47.62351	7.0356	23.28492	0.600566
18	5489	5.2676	14.16775	45.08321	42.69445	48.00573	7.0201	35.30898	12.62463
19	5653	5.3048	14.18235	44.09401	42.30752	47.23022	6.9612	29.99786	7.313505
20	5817	5.3079	14.21008	44.54387	42.67296	47.87611	7.11	26.57218	3.887829
21	5981	5.3172	14.25386	45.37805	42.51294	47.60902	6.9333	26.11466	3.430306
22	6141	5.3389	14.3122	44.13654	42.54918	47.57642	7.0604	22.00618	-0.67817
23	6304	5.3327	14.38218	45.07457	42.7789	48.00939	7.048	32.16148	9.477135
24	6469	5.3389	14.47103	43.69466	42.34855	47.14585	6.9271	28.5928	5.908451
25	6633	5.3513	14.58018	44.71669	42.67296	47.80145	7.0914	34.97912	12.29477
26	6797	5.3668	14.69503	44.86086	42.3584	47.22662	6.9085	36.53411	13.84976
27	6961	5.3761	14.78218	44.23694	42.6234	47.63257	7.1038	43.85713	21.17278
Sol526 Empty:									
A	B	C	D	E	F	G	H	I	J
1	9330	5.2893	14.91855	43.56072	42.13708	46.51831	6.906	29.15853	6.474172
2	9495	5.2924	14.87069	44.13143	42.44219	47.01868	6.906	27.31063	4.626278
3	9659	5.2831	14.86489	44.88322	42.46028	47.17455	6.906	19.36325	-3.32111

4	9823	5.3017	14.80105	43.60138	42.2026	46.66031	6.906	23.33904	0.654683
5	9982	5.2955	14.85764	44.73554	42.59535	47.43185	6.906	32.40373	9.719376
6	10146	5.3017	14.86489	43.74897	42.19768	46.64431	6.906	19.45841	-3.22594
7	10305	5.3079	14.88955	44.60199	42.64487	47.48963	6.906	17.43427	-5.25009
8	10469	5.2893	14.89535	44.35617	42.23537	46.72966	6.906	24.31777	1.633415
9	10633	5.3017	14.89245	44.42266	42.63661	47.45351	6.906	20.75485	-1.92951
10	10792	5.2831	14.8823	44.94862	42.3584	46.97576	6.906	15.1262	-7.55815
11	10956	5.2986	14.85909	44.25396	42.6003	47.36875	6.906	12.18626	-10.4981
12	11121	5.2924	14.84458	45.32761	42.54424	47.33633	6.906	30.48526	7.800908
13	11285	5.3048	14.82282	44.04469	42.51624	47.21405	6.906	16.3586	-6.32575
14	11449	5.2769	14.81266	45.13683	42.68618	47.59453	6.906	27.10577	4.421416
15	11613	5.2924	14.79234	43.8339	42.43561	47.03836	6.906	25.9052	3.220844
16	11778	5.2738	14.82427	44.90558	42.71761	47.65976	6.906	34.69257	12.00822
17	11942	5.2893	14.85329	43.72012	42.2944	46.83652	6.906	10.23369	-12.4507
Sol684 Full:									
A	B	C	D	E	F	G	H	I	J
1	23775	5.714	16.70962	45.25988	43.32241	47.39759	6.4218	39.20077	-6.48523
2	23939	5.7264	16.68958	44.21821	42.97846	46.69586	6.2699	42.02916	-3.65684
3	24099	5.7171	16.68385	45.32935	43.34771	47.42283	6.4156	55.28287	9.59687
4	24263	5.745	16.67955	44.2761	43.05365	46.75813	6.2668	42.40228	-3.28372
5	24427	5.714	16.69387	45.33457	43.36289	47.43546	6.4094	51.74903	6.063025
6	24592	5.7202	16.70246	44.28121	43.03191	46.76704	6.2761	41.82418	-3.86182
7	24756	5.7109	16.72107	45.51744	43.21802	47.21585	6.2637	38.81238	-6.87362
8	24920	5.7202	16.74111	44.40902	43.06201	46.86327	6.3195	49.60469	3.918688
9	25085	5.714	16.75829	45.56107	43.2584	47.28414	6.304	54.44673	8.760727
10	25249	5.7388	16.77832	44.44996	43.09885	46.91502	6.3443	44.94186	-0.74414
11	25413	5.7326	16.79835	45.15067	43.18609	47.12433	6.2916	52.18519	6.499188
12	25573	5.7233	16.82124	44.14164	42.89682	46.58039	6.2327	52.14915	6.463153
13	25737	5.7264	16.84412	45.16279	43.31904	47.37776	6.428	34.41851	-11.2675
14	25896	5.7295	16.87272	44.16546	42.95344	46.64076	6.2389	40.10463	-5.58137
15	26061	5.7295	16.90274	45.21131	43.34265	47.38857	6.4218	44.91344	-0.77256
16	26225	5.7233	16.93562	44.17907	42.97179	46.6532	6.2358	41.14246	-4.54354
17	26389	5.7295	16.96991	45.25294	43.36796	47.41562	6.4249	32.38898	-13.297
18	26554	5.6241	17.0042	44.22162	43.0035	46.6923	6.2575	52.41802	6.732017
19	26718	5.7388	17.04419	45.27897	43.39328	47.43727	6.4249	41.80993	-3.87607
20	26882	5.7326	17.08702	44.25056	43.03692	46.7172	6.2544	48.26239	2.576391
21	27042	5.7202	17.12983	44.94001	43.24494	47.16199	6.3505	65.8632	20.1772
22	27206	5.6954	17.17549	45.02622	42.95511	46.63188	6.2079	57.7761	12.0901
23	27370	5.7326	17.23539	44.56266	43.12567	46.93288	6.335	51.24721	5.561207
24	27534	5.7326	17.28814	45.6747	43.2786	47.25358	6.2885	52.9319	7.2459
25	27694	5.745	17.34087	44.5866	43.20962	47.02047	6.3722	48.07733	2.391331
26	27858	5.7264	17.40356	45.71671	43.27523	47.20327	6.2668	37.647	-8.039
Sol684 Empty:									

A	B	C	D	E	F	G	H	I	J
1	17586	5.7853	16.35129	44.37833	42.96011	46.70831	6.32	48.15077	2.46417
2	17750	5.7543	16.30967	45.20611	43.03692	46.91681	6.32	37.11463	-8.57196
3	17909	5.7636	16.27091	44.208	42.86189	46.56087	6.32	41.6344	-4.05219
4	18068	5.7667	16.23645	45.03657	43.03191	46.93466	6.32	39.80011	-5.88648
5	18232	5.7605	16.19911	44.16546	42.74741	46.37665	6.32	54.52926	8.84266
6	18397	5.7543	16.16895	44.73554	43.07038	46.99364	6.32	28.68083	-17.0058
7	18561	5.7605	16.1359	44.76298	42.7143	46.37488	6.32	53.41969	7.7331
8	18726	5.7512	16.11004	44.46702	42.95344	46.80979	6.32	48.27744	2.59085
9	18890	5.7357	16.08705	45.23385	43.04528	47.00973	6.32	41.75156	-3.93503
10	19049	5.7481	16.06693	44.19949	42.8486	46.61767	6.32	48.41022	2.72363
11	19208	5.7357	16.0468	45.43898	43.11393	47.17635	6.32	50.43643	4.74984
12	19373	5.7388	16.04249	44.34083	42.95344	46.79375	6.32	49.04306	3.35647
13	19537	5.7264	16.04105	45.47384	43.17098	47.24998	6.32	45.27729	-0.4093
14	19701	5.7357	16.03674	44.37321	42.99849	46.85079	6.32	42.32977	-3.35682
15	19866	5.7233	16.06261	45.49127	43.18945	47.27155	6.32	38.95779	-6.7288
16	20030	5.7419	16.08705	44.38685	43.01686	46.87576	6.32	41.25668	-4.42991
17	20195	5.714	16.12728	45.53314	43.19449	47.28234	6.32	44.30899	-1.3776
18	20359	5.7264	16.19624	44.41925	43.03525	46.91681	6.32	53.4644	7.7778
19	20523	5.714	16.27522	45.54187	43.20962	47.29134	6.32	28.91944	-16.7672
20	20682	5.7233	16.36277	44.45849	43.07038	46.95789	6.32	51.51425	5.82766
21	20846	5.714	16.45744	45.62747	43.19617	47.25717	6.32	46.08513	0.39853
22	21006	5.7388	16.53916	44.52508	43.11393	47.01152	6.32	47.27856	1.59197
23	21170	5.7233	16.60794	45.72021	43.18777	47.21225	6.32	50.61143	4.92484
24	21335	5.7295	16.65664	44.54558	43.14076	47.03836	6.32	47.09248	1.40589
25	21499	5.714	16.69244	45.69745	43.20962	47.16558	6.32	56.84534	11.15875
26	21658	5.7357	16.71248	44.57976	43.16762	47.06163	6.32	52.66145	6.97486
Sol573 Enrich Full:									
A	B	C	D	E	F	G	H	I	J
1	12555	5.4257	15.09671	44.15015	42.48002	47.20866	4.9152	54.82562	4.543876
2	12719	5.4195	15.18784	44.94173	42.28948	46.84187	4.7168	56.81344	6.5317
3	12884	5.4257	15.24132	44.23864	42.65148	47.2374	4.9245	73.37316	23.09142
4	13048	5.4381	15.29045	44.99344	42.36825	46.86149	4.7137	96.32437	46.04263
5	13212	5.4226	15.30778	44.30505	42.64652	47.25178	4.9462	56.05641	5.774669
6	13376	5.4536	15.32367	44.12633	42.18949	46.42089	4.6796	34.79068	-15.4911
7	13541	5.4474	15.33234	44.48409	42.67461	47.28954	4.9586	57.26559	6.983847
8	13705	5.435	15.34389	44.24375	42.28456	46.5254	4.7168	55.66849	5.386753
9	13870	5.4598	15.35544	44.54045	42.74079	47.33813	4.9865	68.70816	18.42642
10	14034	5.4567	15.36121	44.26418	42.33213	46.55732	4.7385	49.2632	-1.01854
11	14198	5.4722	15.36699	44.58489	42.78885	47.36334	4.9927	71.16022	20.87848
12	14357	5.4505	15.36699	44.12803	42.37318	46.5662	4.7602	55.18941	4.907672
13	14521	5.4722	15.36988	44.65845	42.82701	47.40119	5.0082	55.18932	4.907584
14	14681	5.4536	15.37998	43.66921	42.39946	46.56265	4.7602	65.94145	15.65971

15	14845	5.4567	15.38864	44.87634	42.79548	47.37235	4.9369	60.55532	10.27358
16	15009	5.4567	15.38864	43.81351	42.46357	46.68341	4.7912	67.23216	16.95042
17	15174	5.4536	15.40019	44.88494	42.83697	47.41021	4.9617	85.66665	35.38491
18	15338	5.4753	15.42328	43.8288	42.48825	46.69586	4.8191	41.8814	-8.40034
19	15502	5.4536	15.44925	45.12298	42.73251	47.24998	4.8284	59.19456	8.912819
20	15666	5.4722	15.48243	44.00728	42.55907	46.849	4.8687	51.23359	0.951845
21	15831	5.5652	15.50406	45.14894	42.82369	47.34533	4.8656	58.27733	7.995595
22	15995	5.4753	15.52137	44.04299	42.6036	46.89182	4.8873	68.86959	18.58785
23	16154	5.4381	15.52858	45.23732	42.51294	46.83117	4.6951	77.74856	27.46682
24	16318	5.4629	15.53435	44.24034	42.66139	47.0312	4.9245	52.0066	1.724857
25	16483	5.4722	15.54011	45.33457	42.58545	46.94896	4.7664	56.25607	5.97433
26	16647	5.4598	15.55885	44.29483	42.71761	47.09745	4.9524	38.26968	-12.0121
27	16811	5.4691	15.58336	44.54899	42.34034	46.46161	4.6889	54.66129	4.379554
28	16976	5.4815	15.63236	44.47727	42.74907	47.18891	4.9679	56.59688	6.315138
29	17140	5.4784	15.70726	43.76426	42.27964	46.40673	4.7292	88.8915	38.60976
30	17305	5.4784	15.79365	44.6653	42.77392	47.28234	4.9679	60.29715	10.01541
31	17469	5.4784	15.88862	43.64546	42.37646	46.46692	4.7509	57.40298	7.121236
32	17634	5.4691	15.98355	44.8987	42.78387	47.26616	4.9307	54.48134	4.199604
Sol573 Enrich Empty:									
A	B	C	D	E	F	G	H	I	J
1	19022	5.4877	16.45171	44.79559	42.87686	47.30753	4.848	28.49673	-21.785
2	19181	5.4908	16.40438	43.78464	42.51953	46.57862	4.848	48.9216	-1.36015
3	19345	5.4877	16.33694	44.87806	42.91512	47.35974	4.848	40.7296	-9.55215
4	19510	5.4908	16.25512	43.80502	42.54259	46.62122	4.848	37.12602	-13.1557
5	19674	5.4753	16.17182	44.90214	42.92678	47.39398	4.848	52.94976	2.668017
6	19838	5.4815	16.08705	43.80842	42.54589	46.60879	4.848	34.2071	-16.0746
7	19998	5.4939	16.0123	44.96068	42.92012	47.4048	4.848	72.92387	22.64212
8	20162	5.3606	15.94616	43.86449	42.54589	46.70297	4.848	39.53002	-10.7517
9	20466	5.4505	15.88718	44.01408	42.64157	46.85792	4.848	52.67756	2.39582
10	20625	5.4567	15.85265	44.64134	42.83365	47.26616	4.848	49.66292	-0.61883
11	20789	5.466	15.82099	44.61396	42.48002	46.65675	4.848	58.80831	8.526564
12	20954	5.4567	15.79509	44.55583	42.86189	47.33453	4.848	66.42976	16.14801
13	21118	5.5373	15.77349	44.49434	42.46028	46.58926	4.848	58.13909	7.857341
14	21283	5.466	15.72454	44.52849	42.83033	47.30753	4.848	52.72514	2.443392
15	21447	5.4257	15.68422	45.28071	42.65148	47.01868	4.848	52.56453	2.282789
16	21611	5.4443	15.64964	44.39879	42.82369	47.27155	4.848	51.28901	1.007263
17	21776	5.4381	15.61506	45.13337	42.58215	46.89539	4.848	57.60865	7.326903
Sol684 Enrich Full:									
A	B	C	D	E	F	G	H	I	J
1	12136	5.6923	15.87711	44.41414	42.80709	47.07954	4.1805	93.17943	25.16943
2	12301	5.6861	16.0008	45.46861	42.7441	46.92395	3.9914	79.12805	11.11805
3	12460	5.7264	16.09567	44.56437	42.97012	47.17276	4.2208	110.9244	42.91444
4	12770	5.7109	16.24507	45.0642	43.02856	47.25178	4.1681	56.79218	-11.2178

5	12935	5.7295	16.27378	44.0685	42.75238	46.61945	4.0782	79.3022	11.2922
6	13099	5.7295	16.29531	45.34152	43.06369	47.22123	4.0999	82.76889	14.75889
7	13263	5.7698	16.30967	44.37321	42.90514	46.7991	4.1619	110.9472	42.93719
8	13427	5.7233	16.34268	45.61873	42.90181	46.97934	3.9976	76.78682	8.776818
9	13592	5.7481	16.33694	44.53532	43.04027	46.99006	4.1991	113.1123	45.10232
10	13751	5.7357	16.35416	45.10569	42.76564	46.53072	3.9635	102.4012	34.39118
11	13915	5.7481	16.37281	44.76298	43.14412	47.12254	4.165	74.95907	6.949067
12	14080	5.7481	16.39146	44.34083	42.71099	46.33422	4.0069	72.15404	4.144039
13	14244	5.7636	16.40151	44.96413	43.20457	47.23561	4.2611	77.65707	9.64707
14	14409	5.7636	16.42159	44.01748	42.83199	46.44921	4.0348	108.4102	40.40023
15	14573	5.7543	16.42446	45.18705	43.23821	47.29313	4.2239	108.7435	40.73352
16	14737	5.7698	16.43163	44.2063	42.92345	46.63188	4.0937	77.65813	9.648126
17	14901	5.7729	16.44023	45.44247	43.23148	47.26256	4.1495	77.97625	9.96625
18	15066	5.7791	16.4388	44.41584	43.04528	46.82939	4.1681	72.4543	4.444296
19	15230	5.7636	16.4388	45.65895	43.11896	47.05089	4.0348	80.60734	12.59734
20	15395	5.7729	16.44023	44.58318	43.12735	46.9704	4.1991	91.5853	23.5753
21	15559	5.7791	16.43737	44.47385	42.66965	46.20003	3.9139	102.8001	34.79007
22	15723	5.7915	16.42733	44.8815	43.1609	47.11179	4.2456	87.84815	19.83815
23	15883	5.7729	16.41872	43.98008	42.77061	46.35897	4.0162	84.13345	16.12345
24	16047	5.776	16.41155	45.13683	43.22139	47.23022	4.2239	112.2893	44.27932
25	16207	5.7853	16.40294	44.19779	42.91346	46.58572	4.0968	73.1899	5.179897
26	16371	5.7729	16.39577	45.58378	42.97012	46.82761	3.9821	99.57195	31.56195
Sol684 Enrich Empty:									
A	B	C	D	E	F	G	H	I	J
1	17586	5.7853	16.35129	0.931593	44.37833	42.96011	4.111	71.97914	3.967781
2	17750	5.7543	16.30967	0.912448	45.20611	43.03692	4.111	55.48204	-12.5293
3	17909	5.7636	16.27091	0.894619	44.208	42.86189	4.111	62.605	-5.40636
4	18068	5.7667	16.23645	0.878767	45.03657	43.03191	4.111	59.43607	-8.57529
5	18232	5.7605	16.19911	0.861591	44.16546	42.74741	4.111	81.5075	13.49614
6	18397	5.7543	16.16895	0.847716	44.73554	43.07038	4.111	42.88791	-25.1234
7	18561	5.7605	16.1359	0.832516	44.76298	42.7143	4.111	79.8076	11.79624
8	18726	5.7512	16.11004	0.820618	44.46702	42.95344	4.111	72.20165	4.190285
9	18890	5.7357	16.08705	0.810042	45.23385	43.04528	4.111	62.39773	-5.61363
10	19049	5.7481	16.06693	0.800786	44.19949	42.8486	4.111	72.40265	4.391285
11	19208	5.7357	16.0468	0.791529	45.43898	43.11393	4.111	75.48778	7.476422
12	19373	5.7388	16.04249	0.789546	44.34083	42.95344	4.111	73.30206	5.290696
13	19537	5.7264	16.04105	0.788884	45.47384	43.17098	4.111	67.72685	-0.28451
14	19701	5.7357	16.03674	0.786901	44.37321	42.99849	4.111	63.18049	-4.83087
15	19866	5.7233	16.06261	0.798802	45.49127	43.18945	4.111	58.25675	-9.75461
16	20030	5.7419	16.08705	0.810042	44.38685	43.01686	4.111	61.65215	-6.35921
17	20195	5.714	16.12728	0.82855	45.53314	43.19449	4.111	66.33318	-1.67818
18	20359	5.7264	16.19624	0.860269	44.41925	43.03525	4.111	79.87382	11.86246
19	20523	5.714	16.27522	0.8966	45.54187	43.20962	4.111	43.22082	-24.7905

20	20682	5.7233	16.36277	0.936873	44.45849	43.07038	4.111	76.8138	8.802443
21	20846	5.714	16.45744	0.980424	45.62747	43.19617	4.111	61.11781	-6.89356
22	21006	5.7388	16.53916	1.018014	44.52508	43.11393	4.111	70.89978	2.888423
23	21170	5.7233	16.60794	1.049653	45.72021	43.18777	4.111	75.65976	7.648398
24	21335	5.7295	16.65664	1.072055	44.54558	43.14076	4.111	70.46315	2.451786
25	21499	5.714	16.69244	1.088522	45.69745	43.20962	4.111	84.91746	16.9061
26	21658	5.7357	16.71248	1.097742	44.57976	43.16762	4.111	78.68243	10.67107

References and Notes

1. S. K. Atreya, P. R. Mahaffy, A. S. Wong, Methane and related trace species on Mars: Origin, loss, implications for life, and habitability. *Planet. Space Sci.* **55**, 358–369 (2007). doi:10.1016/j.pss.2006.02.005

2. V. A. Krasnopolsky, J. P. Maillard, T. C. Owen, Detection of methane in the martian atmosphere: Evidence for life? *Icarus* **172**, 537–547 (2004). doi:10.1016/j.icarus.2004.07.004

3. C. Oze, M. Sharma, Have olivine, will gas: Serpentinization and the abiogenetic production of methane on Mars. *Geophys. Res. Lett.* **32**, L10203 (2005). doi:10.1029/2005GL022691

4. F. Keppler, I. Vigano, A. McLeod, U. Ott, M. Früchtl, T. Röckmann, Ultraviolet-radiation-induced methane emissions from meteorites and the martian atmosphere. *Nature* **486**, 93–96 (2012). Medline

5. A. Schuerger, J. E. Moores, C. A. Clausen, N. G. Barlow, D. T. Britt, Methane from UV-irradiated carbonaceous chondrites under simulated martian conditions. *J. Geophys. Res.* **117**, E08007 (2012). doi:10.1029/2011JE004023

6. O. Poch, S. Kaci, F. Stalport, C. Szopa, P. Coll, Laboratory insights into the chemical and kinetic evolution of several organic molecules under simulated Mars surface UV radiation conditions. *Icarus* **242**, 50–63 (2014). doi:10.1016/j.icarus.2014.07.014

7. V. A. Krasnopolsky, Some problems related to the origin of methane on Mars. *Icarus* **180**, 359–367 (2006). doi:10.1016/j.icarus.2005.10.015

8. E. Chassefière, Metastable methane clathrate particles as a source of methane to the martian atmosphere. *Icarus* **204**, 137–144 (2009). doi:10.1016/j.icarus.2009.06.016

9. P.-Y. Meslin, R. Gough, L. Lefevre, F. Forget, Little variability of methane on Mars induced by adsorption in the regolith. *Planet. Space Sci.* **59**, 247–258 (2011). doi:10.1016/j.pss.2010.09.022

10. R. V. Gough, M. A. Tolbert, C. P. McKay, O. B. Toon, Methane adsorption on a martian soil analog: An abiogenic explanation for methane variability in the martian atmosphere. *Icarus* **207**, 165–174 (2010). doi:10.1016/j.icarus.2009.11.030

11. S. McMahon, J. Parnell, N. J. F. Blamey, Sampling methane in basalt on Earth and Mars. *Int. J. Astrobiol.* **12**, 113–122 (2013). doi:10.1017/S1473550412000481

12. G. Etiope, D. Z. Oehler, C. C. Allen, Methane emissions from Earth's degassing: Implications for Mars. *Planet. Space Sci.* **59**, 182–195 (2011). doi:10.1016/j.pss.2010.06.003

13. M. J. Mumma, G. L. Villanueva, R. E. Novak, T. Hewagama, B. P. Bonev, M. A. Disanti, A. M. Mandell, M. D. Smith, Strong release of methane on Mars in northern summer 2003. *Science* **323**, 1041–1045 (2009). Medline doi:10.1126/science.1165243

14. V. Formisano, S. Atreya, T. Encrenaz, N. Ignatiev, M. Giuranna, Detection of methane in the atmosphere of Mars. *Science* **306**, 1758–1761 (2004). Medline doi:10.1126/science.1101732

15. A. Geminale, V. Formisano, G. Sindoni, Mapping methane in martian atmosphere with PFS-MEX data. *Planet. Space Sci.* **59**, 137–148 (2011). doi:10.1016/j.pss.2010.07.011

16. S. Fonti, G. A. Marzo, Mapping the methane on Mars. *Astron. Astrophys.* **512**, A51 (2010). doi:10.1051/0004-6361/200913178

17. V. A. Krasnopolsky, A sensitive search for methane and ethane on Mars, *EPSC abstracts* **6**, 49 (2011).

18. V. A. Krasnopolsky, Search for methane and upper limits to ethane and SO_2 on Mars. *Icarus* **217**, 144–152 (2012). doi:10.1016/j.icarus.2011.10.019

19. G. L. Villanueva, M. J. Mumma, R. E. Novak, Y. L. Radeva, H. U. Käufl, A. Smette, A. Tokunaga, A. Khayat, T. Encrenaz, P. Hartogh, A sensitive search for organics (CH_4, CH_3OH, H_2CO, C_2H_6, C_2H_2, C_2H_4), hydroperoxyl (HO2), nitrogen compounds (N_2O, NH_3, HCN) and chlorine species (HCl, CH_3Cl) on Mars using ground-based high-resolution infrared spectroscopy. *Icarus* **223**, 11–27 (2013). doi:10.1016/j.icarus.2012.11.013

20. F. Lefèvre, F. Forget, Observed variations of methane on Mars unexplained by known atmospheric chemistry and physics. *Nature* **460**, 720–723 (2009). Medline doi:10.1038/nature08228

21. S. K. Atreya, O. Witasse, V. F. Chevrier, F. Forget, P. R. Mahaffy, P. Buford Price, C. R. Webster, R. W. Zurek, Methane on Mars: Current observations, interpretations, and future plans. *Planet. Space Sci.* **59**, 133–136 (2011). doi:10.1016/j.pss.2010.10.008

22. K. J. Zahnle, R. S. Freedman, D. C. Catling, Is there methane on Mars? *Icarus* **212**, 493–503 (2011). doi:10.1016/j.icarus.2010.11.027

23. P. R. Christensen, Mars as seen from the 2001 Mars Odyssey Thermal Emission Imaging System experiment, *EOS Trans. AGU Fall Meet. Suppl.* **84** (46), Abstract P21A-02, 2003.

24. F. Gaillard, J. Michalski, G. Berger, S. M. McLennan, B. Scaillet, Geochemical reservoirs and timing of sulfur cycling on Mars. *Space Sci. Rev.* **174**, 251–300 (2013). doi:10.1007/s11214-012-9947-4

25. M. A. Mischna, M. Allen, M. I. Richardson, C. E. Newman, A. D. Toigo, Atmospheric modeling of Mars methane surface releases. *Planet. Space Sci.* **59**, 227–237 (2011). doi:10.1016/j.pss.2010.07.005

26. S. K. Atreya, A. S. Wong, N. O. Renno, W. M. Farrell, G. T. Delory, D. D. Sentman, S. A. Cummer, J. R. Marshall, S. C. Rafkin, D. C. Catling, Oxidant enhancement in martian dust devils and storms: Implications for life and habitability. *Astrobiology* **6**, 439–450 (2006). Medline doi:10.1089/ast.2006.6.439

27. G. T. Delory, W. M. Farrell, S. K. Atreya, N. O. Renno, A. S. Wong, S. A. Cummer, D. D. Sentman, J. R. Marshall, S. C. Rafkin, D. C. Catling, Oxidant enhancement in martian dust devils and storms: Storm electric fields and electron dissociative attachment. *Astrobiology* **6**, 451–462 (2006). Medline doi:10.1089/ast.2006.6.451

28. W. M. Farrell, G. T. Delory, S. K. Atreya, Martian dust storms as a possible sink of atmospheric methane. *J. Geophys. Res.* **33**, L21203 (2006).

29. P. R. Mahaffy, C. R. Webster, M. Cabane, P. G. Conrad, P. Coll, S. K. Atreya, R. Arvey, M. Barciniak, M. Benna, L. Bleacher, W. B. Brinckerhoff, J. L. Eigenbrode, D. Carignan, M. Cascia, R. A. Chalmers, J. P. Dworkin, T. Errigo, P. Everson, H. Franz, R. Farley, S. Feng, G. Frazier, C. Freissinet, D. P. Glavin, D. N. Harpold, D. Hawk, V. Holmes, C. S. Johnson, A. Jones, P. Jordan, J. Kellogg, J. Lewis, E. Lyness, C. A. Malespin, D. K. Martin, J. Maurer, A. C. McAdam, D. McLennan, T. J. Nolan, M. Noriega, A. A. Pavlov, B. Prats, E. Raaen, O. Sheinman, D. Sheppard, J. Smith, J. C. Stern, F. Tan, M. Trainer, D. W. Ming, R. V. Morris, J. Jones, C. Gundersen, A. Steele, J. Wray, O. Botta, L. A. Leshin, T. Owen, S. Battel, B. M. Jakosky, H. Manning, S. Squyres, R. Navarro-González, C. P. McKay, F. Raulin, R. Sternberg, A. Buch, P. Sorensen, R. Kline-Schoder, D. Coscia, C. Szopa, S. Teinturier, C. Baffes, J. Feldman, G. Flesch, S. Forouhar, R. Garcia, D. Keymeulen, S. Woodward, B. P. Block, K. Arnett, R. Miller, C. Edmonson, S. Gorevan, E. Mumm, The Sample Analysis at Mars investigation and instrument suite. *Space Sci. Rev.* **170**, 401–478 (2012). doi:10.1007/s11214-012-9879-z

30. C. R. Webster, P. R. Mahaffy, Determining the local abundance of martian methane and its' $^{13}C/^{12}C$ and D/H isotopic ratios for comparison with related gas and soil analysis on the 2011 Mars Science Laboratory (MSL) mission. *Planet. Space Sci.* **59**, 271–283 (2011). doi:10.1016/j.pss.2010.08.021

31. C. R. Webster, P. R. Mahaffy, G. J. Flesch, P. B. Niles, J. H. Jones, L. A. Leshin, S. K. Atreya, J. C. Stern, L. E. Christensen, T. Owen, H. Franz, R. O. Pepin, A. Steele; the MSL Science Team, Isotope ratios of H, C, and O in CO_2 and H_2O of the martian atmosphere. *Science* **341**, 260–263 (2013). Medline doi:10.1126/science.1237961

32. See supplementary materials on *Science* Online.

33. C. R. Webster, P. R. Mahaffy, S. K. Atreya, G. J. Flesch, K. A. Farley; MSL Science Team, Low upper limit to methane abundance on Mars. *Science* **342**, 355–357 (2013). Medline doi:10.1126/science.1242902

34. C. Freissinet *et al*., Organic Molecules in the Sheepbed Mudstone of Gale Crater, Mars, *8th International Conf. on Mars*, Abstract No. 1349 (2014).

35. J. R. C. Garry, I. L. ten Kate, Z. Martins, P. Nørnberg, P. Ehrenfreund, Analysis and survival of amino acids in martian regolith analogs. *Meteorit. Planet. Sci.* **41**, 391–405 (2006). doi:10.1111/j.1945-5100.2006.tb00470.x

36. J. Gómez-Elvira, C. Armiens, I. Carrasco, M. Genzer, F. Gómez, R. Haberle, V. E. Hamilton, A.-M. Harri, H. Kahanpää, O. Kemppinen, A. Lepinette, J. Martín Soler, J. Martín-Torres, J. Martínez-Frías, M. Mischna, L. Mora, S. Navarro, C. Newman, M. A. de Pablo, V. Peinado, J. Polkko, S. C. R. Rafkin, M. Ramos, N. O. Rennó, M. Richardson, J. A. Rodríguez-Manfredi, J. J. Romeral Planelló, E. Sebastián, M. de la Torre Juárez, J. Torres, R. Urquí, A. R. Vasavada, J. Verdasca, M.-P. Zorzano, Curiosity's rover environmental monitoring station: Overview of the first 100 sols. *J. Geophys. Res.* **119**, 1680–1688 (2014). doi:10.1002/2013JE004576

37. T. H. McConnochie *et al*., ChemCam Passive Spectroscopy of Atmospheric O2 and H2O, *8th International Conf. on Mars*, Abstract #1328 (2014).

38. D. M. Hassler, C. Zeitlin, R. F. Wimmer-Schweingruber, S. Böttcher, C. Martin, J. Andrews, E. Böhm, D. E. Brinza, M. A. Bullock, S. Burmeister, B. Ehresmann, M. Epperly, D.

Grinspoon, J. Köhler, O. Kortmann, K. Neal, J. Peterson, A. Posner, S. Rafkin, L. Seimetz, K. D. Smith, Y. Tyler, G. Weigle, G. Reitz, F. A. Cucinotta, The Radiation Assessment Detector (RAD) investigation. *Space Sci. Rev.* **170**, 503–558 (2012). doi:10.1007/s11214-012-9913-1

39. M. T. Lemmon, The Mars Science Laboratory Optical Depth Record, *8th International Conf. on Mars,* Abstract #1338 (2014).

40. A. Geminal *et al*., Methane in martian atmosphere: Average spatial, diurnal and seasonal behavior. *Planet. Space Sci.* **56**, 1194–1203 (2008). doi:10.1016/j.pss.2008.03.004

41. M. E. Schmidt *et al*., Geochemical Classification of Rocks in Gale Crater with APXS to sol 360: Sediment provenance, mixing, and diagenetic processes, 45th Lunar and Planet. Sci. Conf. Abstr. #1504 (2014).

42. H. K. Newsom *et al*., "Gale Crater and Impact Processes from Curiosity," 45th Lunar and Planetary Science Conference (LPSC), Abstract #2103 (2014).

43. L. S. Rothman, I. E. Gordon, A. Barbe, D. C. Benner, P. F. Bernath, M. Birk, V. Boudon, L. R. Brown, A. Campargue, J.-P. Champion, K. Chance, L. H. Coudert, V. Dana, V. M. Devi, S. Fally, J.-M. Flaud, R. R. Gamache, A. Goldman, D. Jacquemart, I. Kleiner, N. Lacome, W. J. Lafferty, J.-Y. Mandin, S. T. Massie, S. N. Mikhailenko, C. E. Miller, N. Moazzen-Ahmadi, O. V. Naumenko, A. V. Nikitin, J. Orphal, V. I. Perevalov, A. Perrin, A. Predoi-Cross, C. P. Rinsland, M. Rotger, M. Šimečková, M. A. H. Smith, K. Sung, S. A. Tashkun, J. Tennyson, R. A. Toth, A. C. Vandaele, J. Vander Auwera, The *HITRAN* 2008 molecular spectroscopic database. *J. Quant. Spectrosc. Radiat. Transfer* **110**, 533–572 (2009). doi:10.1016/j.jqsrt.2009.02.013

44. C. R. Webster, R. T. Menzies, E. D. Hinkley, "Infrared laser absorption: theory and applications," in *Laser Remote Chemical Analysis*, R. M. Measures, Ed. (Wiley, New York, 1988), chap. 3.

45. A. Buch *et al*., Detection of Organics at Mars: How Wet Chemistry Onboard SAM Helps," 44th Lunar and Planetary Science Conference (LPSC) abstract #1512 (2013).

Mars Science Laboratory (MSL) Science Team List October 2014

First name Last name	Institution Affiliation
William Abbey	Jet Propulsion Laboratory, California Institute of Technology
Cherie Achilles	Indiana University Bloomington
Christophe Agard	Centre National d'Etudes Spatiales (CNES)
José Alexandre Alves Verdasca	Centro de Astrobiología (CSIC/INTA)
Dana Anderson	California Institute of Technology
Robert C. Anderson	Jet Propulsion Laboratory, California Institute of Technology
Ryan B. Anderson	United States Geological Survey Flagstaff
Jan Kristoffer Appel	University of Kiel
Paul Douglas Archer	Jacobs, NASA Johnson Space Center
Ricardo Arevalo	NASA Goddard Space Flight Center
Carlos Armiens-Aparicio	Centro de Astrobiología (CSIC/INTA)
Raymond Arvidson	Washington University in St. Louis
Evgeny Atlaskin	Finnish Meteorological Institute and University of Helsinki
Sushil Atreya	University of Michigan Ann Arbor
Andrew Aubrey	Jet Propulsion Laboratory, California Institute of Technology
Sherif Azeez	Delaware State University
Burt Baker	Malin Space Science Systems
Michael Baker	California Institute of Technology
Tonci Balic-Zunic	University of Copenhagen
David Baratoux	Institut de Recherche en Astrophysique et Planétologie, CNRS/University Paul Sabatier
Julien Baroukh	Centre National d'Etudes Spatiales (CNES)
Bruce Barraclough	Planetary Science Institute
Michael Battalio	Texas A&M
Michael Beach	Malin Space Science Systems
Keri Bean	Texas A&M
Pierre Beck	Institut des Sciences de la Terre
Richard Becker	University of Minnesota
Luther Beegle	Jet Propulsion Laboratory, California Institute of Technology
Alberto Behar	Jet Propulsion Laboratory, California Institute of Technology
Inès Belgacem	IRAP (Institut de Recherche en Astrophysique et Planetologie) and CNES (Centre National d'Etudes Spatiales)
James F. Bell III	Arizona State University
Steven Bender	Planetary Science Institute
Mehdi Benna	University of Maryland Baltimore County
Jennifer Bentz	University of Saskatchewan
Gilles Berger	Institut de Recherche en Astrophysique et Planétologie, CNRS/University Paul Sabatier

Jeffrey Berger	Western University
Thomas Berger	Deutsches Zentrum für Luft- und Raumfahrt
Genesis Berlanga	Mount Holyoke College
Daniel Berman	Planetary Science Institute
David Bish	Indiana University Bloomington
Jordana Blacksberg	Jet Propulsion Laboratory, California Institute of Technology
David F. Blake	NASA Ames Research Center
Juan José Blanco Ávalos	Universidad de Alcalá
Diana Blaney	Jet Propulsion Laboratory, California Institute of Technology
Jennifer Blank	Blue Marble Space Inst. of Science and NASA Ames Research Center
Hannah Blau	University of Massachusetts
Lora Bleacher	NASA Goddard Space Flight Center
Eckart Boehm	University of Kiel
Jean-Yves Bonnet	Laboratoire Atmosphères, Milieux, Observations Spatiales (LATMOS)
Oliver Botta	Swiss Space Office
Stephan Böttcher	University of Kiel
Thomas Boucher	University of Massachusetts
Hannah Bower	University of Maryland College Park
Nick Boyd	University of Guelph
William Boynton	University of Arizona
Shaneen Braswell	University of Michigan
Elly Breves	Mount Holyoke College
John C. Bridges	University of Leicester
Nathan Bridges	Johns Hopkins University Applied Physics Laboratory
William Brinckerhoff	NASA Goddard Space Flight Center
David Brinza	Jet Propulsion Laboratory, California Institute of Technology
Thomas Bristow	NASA Ames Research Center
Claude Brunet	Canadian Space Agency
Anna Brunner	University of Maryland College Park
Will Brunner	inXitu
Arnaud Buch	Laboratoire Génie des Procédés et Matériaux
Mark Bullock	Southwest Research Institute
Sönke Burmeister	University of Kiel
John Burton	York University
Jennifer Buz	California Institute of Technology
Michel Cabane	Laboratoire Atmosphères, Milieux, Observations Spatiales (LATMOS)
Fred Calef	Jet Propulsion Laboratory, California Institute of Technology
James Cameron	Lightstorm Entertainment Inc.

John L. Campbell	University of Guelph
Bruce Cantor	Malin Space Science Systems
Michael Caplinger	Malin Space Science Systems
Carey Clifton Jr.	University of Massachusetts
Javier Caride Rodríguez	Centro de Astrobiología (CSIC/INTA)
Marco Carmosino	University of Massachusetts
Isaías Carrasco Blázquez	Centro de Astrobiología (CSIC/INTA)
Patrick Cavanagh	Indiana University Bloomington
Antoine Charpentier	Atos
Steve Chipera	Chesapeake Energy
David Choi	University of Michigan
Lance Christensen	Jet Propulsion Laboratory, California Institute of Technology
Benton Clark	Space Science Institute
Sam Clegg	Los Alamos National Laboratory
Timothy Cleghorn	retired
Ed Cloutis	University of Winnipeg
George Cody	Carnegie Institution of Washington
Patrice Coll	Laboratoire Interuniversitaire des Systèmes Atmosphériques (LISA)
Ecaterina I. Coman	Washington University in St. Louis
Pamela Conrad	NASA Goddard Space Flight Center
David Coscia	Laboratoire Atmosphères, Milieux, Observations Spatiales (LATMOS)
Agnès Cousin	Los Alamos National Laboratory
David Cremers	Applied Research Associates, Inc.
Joy A. Crisp	Jet Propulsion Laboratory, California Institute of Technology
Kevin Cropper	Planetary Science Institute
Alain Cros	Institut de Recherche en Astrophysique et Planétologie, CNRS/University Paul Sabatier
Francis Cucinotta	University of Nevada Las Vegas
Claude d'Uston	Institut de Recherche en Astrophysique et Planétologie, CNRS/University Paul Sabatier
Scott Davis	Malin Space Science Systems
Mackenzie Day	University of Texas at Austin
Yves Daydou	Institut de Recherche en Astrophysique et Planétologie, CNRS/University Paul Sabatier
Lauren DeFlores	Jet Propulsion Laboratory, California Institute of Technology
Erwin Dehouck	State University of New York Stony Brook
Dorothea Delapp	Los Alamos National Laboratory
Julia DeMarines	Denver Museum of Nature & Science
Tristan Dequaire	Laboratoire Interuniversitaire des Systèmes Atmosphériques (LISA)
David Des Marais	NASA Ames Research Center

Roch Desrousseaux	University of Michigan Ann Arbor
William Dietrich	University of California Berkeley
Robert Dingler	Los Alamos National Laboratory
Shawn Domagal-Goldman	NASA Goddard Space Flight Center
Christophe Donny	Centre National d'Etudes Spatiales (CNES)
Robert Downs	University of Arizona
Darrell Drake	Retired
Gilles Dromart	Laboratoire de Géologie de Lyon : Terre, Planète, Environnement
Audrey Dupont	CS Systemes d'Inforation
Brian Duston	Malin Space Science Systems
Jason P. Dworkin	NASA Goddard Space Flight Center
M. Darby Dyar	Mount Holyoke College
Lauren Edgar	Arizona State University
Kenneth Edgett	Malin Space Science Systems
Christopher S. Edwards	California Institute of Technology
Laurence Edwards	NASA Ames Research Center
Peter Edwards	University of Leicester
Bethany Ehlmann	Jet Propulsion Laboratory/Caltech and California Institute of Technology
Bent Ehresmann	Southwest Research Institute
Jennifer Eigenbrode	NASA Goddard Space Flight Center
Beverley Elliott	University of New Brunswick
Harvey Elliott	University of Michigan Ann Arbor
Ryan Ewing	Texas A&M
Cécile Fabre	GéoRessources
Alberto Fairén	Centro de Astrobiología (CSIC/INTA)
Alberto Fairén	Cornell University
Kenneth Farley	California Institute of Technology
Jack Farmer	Arizona State University
Caleb Fassett	Mount Holyoke College
Laurent Favot	Capgemini France
Donald Fay	Malin Space Science Systems
Fedor Fedosov	Space Research Institute
Jason Feldman	Jet Propulsion Laboratory, California Institute of Technology
Kim Fendrich	University of Arizona
Erik Fischer	University of Michigan Ann Arbor
Martin Fisk	Oregon State University
Mike Fitzgibbon	University of Arizona
Gregory Flesch	Jet Propulsion Laboratory, California Institute of Technology
Melissa Floyd	NASA Goddard Space Flight Center
Lorenzo Flückiger	Carnegie Mellon University

Olivier Forni	Institut de Recherche en Astrophysique et Planétologie, CNRS/University Paul Sabatier
Valerie Fox	Washington University in St. Louis
Abigail Fraeman	Caltech
Raymond Francis	Western University
Pascaline François	Laboratoire Interuniversitaire des Systèmes Atmosphériques (LISA)
Heather Franz	University of Maryland Baltimore County
Caroline Freissinet	NASA Goddard Space Flight Center
Katherine Louise French	Massachusetts Institute of Technology
Jens Frydenvang	University of Copenhagen
James Garvin	NASA Goddard Space Flight Center
Olivier Gasnault	Institut de Recherche en Astrophysique et Planétologie, CNRS/University Paul Sabatier
Claude Geffroy	Institut de Chimie des Milieux et Matériaux de Poitiers
Ralf Gellert	University of Guelph
Maria Genzer	Finnish Meteorological Institute
Stephanie Getty	NASA Goddard Space Flight Center
Daniel Glavin	NASA Goddard Space Flight Center
Austin Godber	Arizona State University
Fred Goesmann	Max Planck Institute for Solar System Research
Walter Goetz	Max Planck Institute for Solar System Research
Dmitry Golovin	Space Research Institute
Felipe Gómez Gómez	Centro de Astrobiología (CSIC/INTA)
Javier Gómez-Elvira	Centro de Astrobiología (CSIC/INTA)
Brigitte Gondet	Institut d'Astrophysique Spatiale
Suzanne Gordon	University of New Mexico
Stephen Gorevan	Honeybee Robotics
Heather Graham	NASA Goddard Space Flight Center
John Grant	Smithsonian Institution
David Grinspoon	Planetary Science Institute
John Grotzinger	California Institute of Technology
Philippe Guillemot	Centre National d'Etudes Spatiales (CNES)
Jingnan Guo	University of Kiel
Sanjeev Gupta	Imperial College
Scott Guzewich	NASA Goddard Space Flight Center
Robert Haberle	NASA Ames Research Center
Douglas Halleaux	University of Michigan Ann Arbor
Bernard Hallet	University of Washington Seattle
Victoria Hamilton	Southwest Research Institute
Kevin Hand	Jet Propulsion Laboratory, California Institute of Technology
Craig Hardgrove	Arizona State University
Keian Hardy	Los Alamos National Laboratory

David Harker	Malin Space Science Systems
Daniel Harpold	NASA Goddard Space Flight Center
Ari-Matti Harri	Finnish Meteorological Institute
Karl Harshman	University of Arizona
Donald Hassler	Southwest Research Institute
Harri Haukka	Finnish Meteorological Institute
Alexander Hayes	Cornell University
Kenneth Herkenhoff	United States Geological Survey Flagstaff
Paul Herrera	Malin Space Science Systems
Sebastian Hettrich	Centro de Astrobiología (CSIC/INTA)
Ezat Heydari	Jackson State University
Victoria Hipkin	Canadian Space Agency
Tori Hoehler	NASA Ames Research Center
Jeff Hollingsworth	NASA Ames Research Center
Judy Hudgins	Salish Kootenai College
Wesley Huntress	Retired
Joel Hurowitz	State University of New York Stony Brook
Stubbe Hviid	Max Planck Institute for Solar System Research
Karl Iagnemma	Massachusetts Institute of Technology
Stephen Indyk	Honeybee Robotics
Guy Israël	Laboratoire Atmosphères, Milieux, Observations Spatiales (LATMOS)
Ryan Steele Jackson	University of New Mexico
Samantha Jacob	University of Hawai'i at Manoa
Bruce Jakosky	University of Colorado Boulder
Laurent Jean-Rigaud	Atos
Elsa Jensen	Malin Space Science Systems
Jaqueline Kløvgaard Jensen	University of Copenhagen
Jeffrey R. Johnson	Johns Hopkins University Applied Physics Laboratory
Micah Johnson	Microtel
Stephen Johnstone	Los Alamos National Laboratory
Andrea Jones	Lunar and Planetary Institute and NASA Goddard Space Flight Center
John H. Jones	NASA Johnson Space Center
Jonathan Joseph	Cornell University
Mélissa Joulin	Laboratoire de Planétologie et Géodynamique de Nantes
Insoo Jun	Jet Propulsion Laboratory, California Institute of Technology
Linda C. Kah	University of Tennessee Knoxville
Henrik Kahanpää	Finnish Meteorological Institute
Melinda Kahre	NASA Ames Research Center
Hannah Kaplan	Brown University

Natalya Karpushkina	Space Research Institute
Srishti Kashyap	University of Maryland Baltimore County
Janne Kauhanen	Finnish Meteorological Institute
Leslie Keely	NASA Ames Research Center
Simon Kelley	The Open University
Fabian Kempe	Max Planck Institute for Solar System Research
Osku Kemppinen	Finnish Meteorological Institute and Aalto University
Megan R. Kennedy	Malin Space Science Systems
Didier Keymeulen	Jet Propulsion Laboratory, California Institute of Technology
Alexander Kharytonov	University of Kiel
Myung-Hee Kim	Universities Space Research Association
Kjartan Kinch	University of Copenhagen
Penelope King	Australian National University
Randolph Kirk	United States Geological Survey Flagstaff
Laurel Kirkland	Lunar and Planetary Institute
Jacob Kloos	York University
Gary Kocurek	University of Texas at Austin
Asmus Koefoed	University of Copenhagen
Jan Köhler	University of Kiel
Onno Kortmann	University of California Berkeley
Benjamin Kotrc	Massachusetts Institute of Technology
Alexander Kozyrev	Space Research Institute
Johannes Krauß	University of Kiel
Gillian Krezoski	Malin Space Science Systems
Rachel Kronyak	University of Tennessee Knoxville
Daniel Krysak	Malin Space Science Systems
Ruslan Kuzmin	Space Research Institute and Vernadsky Institute
Jean-Luc Lacour	Commissariat à l'Énergie Atomique et aux Énergies Alternatives
Vivian Lafaille	Centre National d'Etudes Spatiales (CNES)
Yves Langevin	Institut d'Astrophysique Spatiale
Nina Lanza	Los Alamos National Laboratory
Mathieu Lapôtre	California Institute of Technology
Marie-France Larif	Centre National d'Etudes Spatiales (CNES)
Jérémie Lasue	Institut de Recherche en Astrophysique et Planétologie, CNRS/University Paul Sabatier
Laetitia Le Deit	Laboratoire de Planétologie et Géodynamique de Nantes
Stéphane Le Mouélic	Laboratoire de Planétologie et Géodynamique de Nantes
Ella Mae Lee	United States Geological Survey Flagstaff
Qiu-Mei Lee	Institut de Recherche en Astrophysique et Planétologie, CNRS/University Paul Sabatier
Rebekka Lee	Brock University
David Lees	Carnegie Mellon University

Matthew Lefavor	Microtel
Mark Lemmon	Texas A&M
Alain Lepinette Malvitte	Centro de Astrobiología (CSIC/INTA)
Kate Lepore	Mount Holyoke College
Laurie Leshin	Worcester Polytechnic Institute
Richard Léveillé	McGill University
Éric Lewin	Institut des Sciences de la Terre
Kevin Lewis	Johns Hopkins University
Shuai Li	Brown University
Kimberly Lichtenberg	Jet Propulsion Laboratory, California Institute of Technology
Leslie Lipkaman	Malin Space Science Systems
Denis Lisov	Space Research Institute
Cynthia Little	Los Alamos National Laboratory
Maxim Litvak	Space Research Institute
Lu Liu	University of Washington Seattle
Henning Lohf	University of Kiel
Eric Lorigny	Centre National d'Etudes Spatiales (CNES)
Günter Lugmair	University of California San Diego
Angela Lundberg	Delaware State University
Eric Lyness	Microtel
Morten Bo Madsen	University of Copenhagen
Angela Magee	Malin Space Science Systems
Paul Mahaffy	NASA Goddard Space Flight Center
Justin Maki	Jet Propulsion Laboratory, California Institute of Technology
Teemu Mäkinen	Finnish Meteorological Institute
Alexey Malakhov	Space Research Institute
Charles Malespin	Universities Space Research Association
Michael Malin	Malin Space Science Systems
Nicolas Mangold	Laboratoire de Planétologie et Géodynamique de Nantes
Gerard Manhes	Institut de Physique du Globe de Paris
Heidi Manning	Concordia College
Geneviève Marchand	Canadian Space Agency
Mercedes Marín Jiménez	Centro de Astrobiología (CSIC/INTA)
César Martín García	University of Kiel
David K. Martin	NASA Goddard Space Flight Center
Mildred Martin	Catholic University of America
Peter Martin	California Institute of Technology
Germán Martínez Martínez	University of Michigan Ann Arbor
Jesús Martínez-Frías	Instituto de Geociencias (CSIC-UCM)
Jaime Martín-Sauceda	Centro de Astrobiología (CSIC/INTA)

Martín	
Javier Martín-Soler	Centro de Astrobiología (CSIC/INTA)
F. Javier Martín-Torres	Instituto Andaluz de Ciencias de la Tierra (CSIC-UGR)
Emily Mason	Texas A&M
Tristan Matthews	York University
Daniel Matthiä	Deutsches Zentrum für Luft- und Raumfahrt
Patrick Mauchien	Commissariat à l'Énergie Atomique et aux Énergies Alternatives
Sylvestre Maurice	Institut de Recherche en Astrophysique et Planétologie, CNRS/University Paul Sabatier
Amy McAdam	NASA Goddard Space Flight Center
Marie McBride	Malin Space Science Systems
Elaina McCartney	Malin Space Science Systems
Timothy McConnochie	University of Maryland
Emily McCullough	Western University
Ian McEwan	Ashima Research
Christopher McKay	NASA Ames Research Center
Hannah McLain	Catholic University of America
Scott McLennan	State University of New York Stony Brook
Sean McNair	Malin Space Science Systems
Noureddine Melikechi	Delaware State University
Teresa Mendaza de Cal	Centro de Astrobiología (CSIC/INTA)
Sini Merikallio	Finnish Meteorological Institute
Sean Merritt	Malin Space Science Systems
Pierre-Yves Meslin	Institut de Recherche en Astrophysique et Planétologie, CNRS/University Paul Sabatier
Michael Meyer	NASA Headquarters
Alissa Mezzacappa	Delaware State University
Sarah Milkovich	Jet Propulsion Laboratory, California Institute of Technology
Maëva Millan	Laboratoire Atmosphères, Milieux, Observations Spatiales (LATMOS)
Hayden Miller	California Institute of Technology
Kristen Miller	Massachusetts Institute of Technology
Ralph Milliken	Brown University
Douglas Ming	NASA Johnson Space Center
Michelle Minitti	Planetary Science Institute
Michael Mischna	Jet Propulsion Laboratory, California Institute of Technology
Julie Mitchell	Arizona State University
Igor Mitrofanov	Space Research Institute
Jeffrey Moersch	University of Tennessee Knoxville
Maxim Mokrousov	Space Research Institute
Antonio Molina Jurado	Centro de Astrobiología (CSIC/INTA)
Casey Moore	York University

John E. Moores	York University
Luis Mora-Sotomayor	Centro de Astrobiología (CSIC/INTA)
Gines Moreno	Centro de Astrobiología (CSIC/INTA)
John Michael Morookian	Jet Propulsion Laboratory, California Institute of Technology
Richard V. Morris	NASA Johnson Space Center
Shaunna Morrison	University of Arizona
Valérie Mousset	Centre National d'Etudes Spatiales (CNES)
Alankrita Mrigakshi	Deutsches Zentrum für Luft- und Raumfahrt
Reinhold Mueller-Mellin	University of Kiel
Jan-Peter Muller	University College London
Guillermo Muñoz Caro	Centro de Astrobiología (CSIC/INTA)
Marion Nachon	Laboratoire de Planétologie et Géodynamique de Nantes
Abbey Nastan	California Institute of Technology
Sara Navarro López	Centro de Astrobiología (CSIC/INTA)
Rafael Navarro-González	University Nacional Autónoma de México
Kenneth Nealson	University of Southern California
Ara Nefian	Carnegie Mellon University
Tony Nelson	Los Alamos National Laboratory
Megan Newcombe	California Institute of Technology
Claire Newman	Ashima Research
Horton Newsom	University of New Mexico
Sergey Nikiforov	Space Research Institute
Matthew Nikitczuk	Brock University
Paul Niles	NASA Johnson Space Center
Brian Nixon	Malin Space Science Systems
Audrey Noblet	Laboratoire Interuniversitaire des Systèmes Atmosphériques (LISA)
Eldar Noe Dobrea	Planetary Science Institute
Thomas Nolan	Nolan Engineering
Dorothy Oehler	Jacobs Technology
Ann Ollila	University of New Mexico
Timothy Olson	Salish Kootenai College
Tobias Orthen	University of Kiel
Tobias Owen	University of Hawai'i at Manoa
Marie Ozanne	Mount Holyoke College
Miguel Ángel de Pablo Hernández	Universidad de Alcalá
Hannah Pagel	Los Alamos National Laboratory
Alexis Paillet	Centre National d'Etudes Spatiales (CNES)
Etienne Pallier	Institut de Recherche en Astrophysique et Planétologie,

	CNRS/University Paul Sabatier
Marisa Palucis	University of California Berkeley
Timothy Parker	Jet Propulsion Laboratory, California Institute of Technology
Yann Parot	Institut de Recherche en Astrophysique et Planétologie, CNRS/University Paul Sabatier
Alex Parra	Los Alamos National Laboratory
Kiran Patel	Global Science & Technology, Inc.
Mark Paton	Finnish Meteorological Institute
Gale Paulsen	Honeybee Robotics
Alexander Pavlov	NASA Goddard Space Flight Center
Betina Pavri	Jet Propulsion Laboratory, California Institute of Technology
Verónica Peinado-González	Centro de Astrobiología (CSIC/INTA)
Robert Pepin	University of Minnesota
Laurent Peret	Atos
René Pérez	Centre National d'Etudes Spatiales (CNES)
Glynis Perrett	University of Guelph
Joseph Peterson	Southwest Research Institute
Cedric Pilorget	California Institute of Technology
Patrick Pinet	Institut de Recherche en Astrophysique et Planétologie, CNRS/University Paul Sabatier
Veronica Pinnick	University of Maryland Baltimore County
Jorge Pla-García	Centro de Astrobiología (CSIC/INTA)
Ianik Plante	Universities Space Research Association
Franck Poitrasson	Géosciences Environnement Toulouse
Jouni Polkko	Finnish Meteorological Institute
Radu Popa	University of Southern California
Liliya Posiolova	Malin Space Science Systems
Arik Posner	NASA Headquarters
Irina Pradler	University of Guelph
Benito Prats	eINFORMe Inc.
Vasily Prokhorov	Space Research Institute
Eric Raaen	NASA Goddard Space Flight Center
Leon Radziemski	Piezo Energy Technologies, Tucson
Scot Rafkin	Southwest Research Institute
Miguel Ramos	Universidad de Alcalá
Elizabeth Rampe	Aerodyne, NASA Johnson Space Center
William Rapin	Institut de Recherche en Astrophysique et Planétologie, CNRS/University Paul Sabatier
François Raulin	Laboratoire Interuniversitaire des Systèmes Atmosphériques (LISA)
Michael Ravine	Malin Space Science Systems
Günther Reitz	Deutsches Zentrum für Luft- und Raumfahrt

Jun Ren	Delaware State University
Nilton Rennó	University of Michigan Ann Arbor
Melissa Rice	Western Washington University
Mark Richardson	Ashima Research
Birgit Ritter	Deutsches Zentrum für Luft- und Raumfahrt
Frances Rivera-Hernández	University of California Davis
François Robert	IMPMC, Muséum d'Histoire Naturelle
Kevin Robertson	Brown University
José Antonio Rodriguez Manfredi	Centro de Astrobiología (CSIC/INTA)
Julio José Romeral-Planelló	Centro de Astrobiología (CSIC/INTA)
Scott Rowland	University of Hawai'i at Manoa
David Rubin	University of California Santa Cruz
Muriel Saccoccio	Centre National d'Etudes Spatiales (CNES)
David Said	Centre National d'Etudes Spatiales (CNES)
Andrew Salamon	Malin Space Science Systems
Anton Sanin	Space Research Institute
Sara Alejandra Sans Fuentes	Centro de Astrobiología (CSIC/INTA)
Lee Saper	Malin Space Science Systems
Philippe Sarrazin	SETI Institute
Violaine Sautter	IMPMC, Muséum d'Histoire Naturelle
Hannu Savijärvi	University of Helsinki
Juergen Schieber	Indiana University Bloomington
Mariek Schmidt	Brock University
Walter Schmidt	Finnish Meteorological Institute
Daniel Scholes	Washington University in St. Louis
Marcel Schoppers	Jet Propulsion Laboratory, California Institute of Technology
Susanne Schröder	Institut de Recherche en Astrophysique et Planétologie, CNRS/University Paul Sabatier
Susanne P. Schwenzer	The Open University
Cauê Sciascia Borlina	University of Michigan Ann Arbor
Anthony Scodary	Jet Propulsion Laboratory, California Institute of Technology
Eduardo Sebastián Martínez	Centro de Astrobiología (CSIC/INTA)
Aaron Sengstacken	Jet Propulsion Laboratory, California Institute of Technology
Jennifer Griffes Shechet	California Institute of Technology
Ruslan Shterts	Canadian Space Agency
Kirsten Siebach	California Institute of Technology
Tero Siili	Finnish Meteorological Institute
John J. Simmonds	Jet Propulsion Laboratory, California Institute of Technology

Jean-Baptiste Sirven	Commissariat à l'Énergie Atomique et aux Énergies Alternatives
Susan Slavney	Washington University in St. Louis
Ronald Sletten	University of Washington Seattle
Michael D. Smith	NASA Goddard Space Flight Center
Pablo Sobron Sanchez	Space Research Institute
Nicole Spanovich	Jet Propulsion Laboratory, California Institute of Technology
John Spray	University of New Brunswick
Justin Spring	Honeybee Robotics
Steven Squyres	Cornell University
Katie Stack	Jet Propulsion Laboratory, California Institute of Technology
Fabien Stalport	Laboratoire Interuniversitaire des Systèmes Atmosphériques (LISA)
Richard Starr	The Catholic University of America & NASA Goddard Space Flight Center
Andrew Steele	Carnegie Institution of Washington
Thomas Stein	Washington University in St. Louis
Jennifer Stern	NASA Goddard Space Flight Center
Noel Stewart	Salish Kootenai College
Wayne Stewart	University of Washington
Susan Louise Svane Stipp	University of Copenhagen
Kevin Stoiber	Malin Space Science Systems
Edward Stolper	California Institute of Technology
Robert Sucharski	United States Geological Survey Flagstaff
Robert Sullivan	Cornell University
Roger Summons	Massachusetts Institute of Technology
Dawn Y. Sumner	University of California Davis
Vivian Sun	Brown University
Kimberley Supulver	Malin Space Science Systems
Brad Sutter	Jacobs, NASA Johnson Space Center
Cyril Szopa	Laboratoire Atmosphères, Milieux, Observations Spatiales (LATMOS)
Florence Tan	NASA Goddard Space Flight Center
Christopher Tate	University of Tennessee Knoxville
Samuel Teinturier	Laboratoire Interuniversitaire des Systèmes Atmosphériques (LISA)
Inge Loes ten Kate	Utrecht University
Alicia Thomas	Brock University
Peter Thomas	Cornell University
Lucy Thompson	University of New Brunswick
Franck Thuillier	Laboratoire de Planétologie et Géodynamique de Nantes
Emmanual Thulliez	Centre National d'Etudes Spatiales (CNES)
Robert Tokar	Planetary Science Institute
Michael Toplis	Institut de Recherche en Astrophysique et Planétologie,

	CNRS/University Paul Sabatier
Manuel de la Torre Juárez	Jet Propulsion Laboratory, California Institute of Technology
Josefina Torres Redondo	Centro de Astrobiología (CSIC/INTA)
Melissa Trainer	NASA Goddard Space Flight Center
Allan Treiman	Lunar and Planetary Institute
Vladislav Tretyakov	Space Research Institute
Aurora Ullán-Nieto	Centro de Astrobiología (CSIC/INTA)
Roser Urqui-O'Callaghan	Centro de Astrobiología (CSIC/INTA)
Patricia Valentín-Serrano	Centro de Astrobiología (CSIC/INTA)
Jason Van Beek	Malin Space Science Systems
Tessa Van Beek	Malin Space Science Systems
Scott VanBommel	University of Guelph
David Vaniman	Planetary Science Institute
Alexey Varenikov	Space Research Institute
Ashwin R. Vasavada	Jet Propulsion Laboratory, California Institute of Technology
Paulo Vasconcelos	University of Queensland
Álvaro de Vicente-Retortillo Rubalcaba	Universidad Complutense Madrid and University of Michigan
Edward Vicenzi	Smithsonian Institution
Andrey Vostrukhin	Space Research Institute
Mary Voytek	NASA Headquarters
Meenakshi Wadhwa	Arizona State University
Jennifer Ward	Washington University in St. Louis
Jessica Watkins	University of California Los Angeles
Christopher R. Webster	Jet Propulsion Laboratory, California Institute of Technology
Gerald Weigle	Big Head Endian LLC
Danika Wellington	Arizona State University
Frances Westall	Centre National de la Recherche Scientifique (CNRS)
Roger Wiens	Los Alamos National Laboratory
Mary Beth Wilhelm	Georgia Institute of Technology and NASA Ames Research Center
Amy Williams	University of California Davis
Joshua Williams	University of New Mexico
Rebecca Williams	Planetary Science Institute
Richard B. Williams	Los Alamos National Laboratory
Kenneth Williford	Jet Propulsion Laboratory, California Institute of Technology
Michael A. Wilson	University of California San Francisco
Sharon A. Wilson	Smithsonian Institution
Robert Wimmer-Schweingruber	University of Kiel

Michael Wolff	Space Science Institute
Michael Wong	University of Michigan Ann Arbor
James Wray	Georgia Institute of Technology
Charles Yana	Centre National d'Etudes Spatiales (CNES)
Albert Yen	Jet Propulsion Laboratory, California Institute of Technology
Aileen Yingst	Planetary Science Institute
Cary Zeitlin	Southwest Research Institute
Robert Zimdar	Malin Space Science Systems
María-Paz Zorzano Mier	Centro de Astrobiología (CSIC/INTA)